Universidade de Aveiro
2012

Departamento de Engenharia de Materiais e Cerâmica

Carla Florbela Ferreira Pinto da Silva

Multifunctional films from porous matrices

Filmes multifuncionais a partir de matrizes porosas

Universidade de Aveiro
2012

Departamento de Engenharia de Materiais e Cerâmica

Carla Florbela Ferreira Pinto da Silva

Multifunctional films from porous matrices

Filmes multifuncionais a partir de matrizes porosas

Dissertation presented to University of Aveiro to obtain the Master degree in Materials Engineering, under the scientific guidance of Dr. Paula Celeste da Silva Ferreira, Auxiliary researcher of Centre for Research in Ceramics and Composite Materials of the University of Aveiro and Prof. Dr. Paula Maria Lousada Silveirinha Vilarinho, Associated Professor of the Department of Materials and Ceramics Engineering of University of Aveiro of the Department of Materials and Ceramics Engineering of University of Aveiro, Portugal.

Dissertação apresentada à Universidade de Aveiro para cumprimento dos requisitos necessários à obtenção do grau de Mestre em Engenharia de Materiais, realizada sob a orientação científica da Doutora Paula Celeste da Silva Ferreira, Investigadora Auxiliar do Centro de Investigação em Materiais Cerâmicos e Compósitos da Universidade de Aveiro, e da Professora Doutora Paula Maria Lousada Silveirinha Vilarinho, Professora Associada do Departamento de Engenharia de Materiais e Cerâmica da Universidade de Aveiro.

Financial support from FCT and FEDER (QREN – COMPETE) of the project PTDC/CTM/098130/2008.

I dedicate this work to my family and to beloved Cristiano, who always supported me...

The Board of Examiners

president

Prof. Dr. Fernando Manuel Bico Marques
Full Professor at University of Aveiro

Dr. Filipe Miguel Henriques Lebre Ramos Figueiredo
Post-Doctoral Research Assistant at CICECO – Centre for Research in Ceramics & Composite Materials, University of Aveiro

Prof. Dr. Ana Cristina Moreira Freire
Associate professor at University of Porto

Dr. Paula Celeste da Silva Ferreira
Post-Doctoral Research Assistant at CICECO – Centre for Research in Ceramics & Composite Materials, University of Aveiro (Supervisor)

Prof. Dr. Paula Maria Lousada Silveirinha Vilarinho
Associate Professor at University of Aveiro (Co-supervisor)

Acknowledgements

Firstly I would like to thank my supervisors, Dr. Paula Ferreira and Prof. Paula Vilarinho, for the guidance, personal support and constant motivation in this work. Furthermore, I'm thankful for the opportunity to integrate this research grant (PTDC/CTM/098130/2008).

Thank you to Dr. Rosário from *Laboratório Central de Análises* of University of Aveiro for her support in XRD analyses and to technical services from Department of Materials and Ceramics Engineering, namely Célia Miranda, Ana Ribeiro and Maria João Bastos for their support in DTA/TGA, UV spectrometry and BET analyses. I would like also to thank Marta Ferro and Bruno for continuous technical support on the electron microscopy analyses. Thank you all for the availability, support and sympathy.

I would like to thank Dr Rui Borges and Dr Liliana Ferreira from the Physics Department of the *Faculty of Science of the* University of Lisbon for the magnetic measurements.

In particular, I would like to thank Alichandra Castro for all the support, patience, sympathy and always willing to help. I will never forget that. Our discussions were very important in this project.

Θα ήθελα να ευχαριστήσω τη Στελλα Σκιαδοπουλου από το γειτονικό δωμάτιο, για όλες τις συζητήσεις που έχουμε κάνει. "Καληνύχτα" ήταν η πρώτη λέξη που έμαθα, και δεν θα την ξεχάσω ποτέ. Είμαι πολύ ευτυχής που σε γνώρισα, ακόμα κι αν στάθηκε σημαντικό εμπόδιο ο αγώνας μου για το ακαδημαϊκό τέλος. Ελπίζω να μπορούμε να κρατήσουμε για πάντα επαφή. Furthermore, I would like to thank you for all the PFM characterization and discussions about this work that we did.

I'm thankful to my laboratory colleagues for the good moments that we have passed together, namely Mirtha, Cláudia, Eliana, Maria João, Nuno, Adelaide and Eddy.

Thank you João Vieira, Paulo Cyhlar, Eduardo Silva and Styliani Skiadopoulou for your very important friendship. Nothing happens just by chance.

And just to close, I'm would like to thank the most important persons in my life, my mom, my father, my grandmother and obviously, my sweetie! I must also thank my 4-legged friends who kept with me through many hours of reading, reflection and writing…

"*Perfer et obdura, dolor hic tibi proderit olim…Omnia cause fiunt*"

keywords

Ferroelectric porous films, ferromagnetic nanoparticles, multiferroics, hydrothermal synthesis, electrophoretic deposition.

abstract

Multiferroic materials, that exhibit both ferroelectric and ferromagnetic properties, have attracted considerable interest in the scientific community due to its potential for novel applications in electronic devices as well as for physics and materials science underlying its multifunctionality. In multiferroic composites, the coupling magnetoelectric is due to elastic interaction between ferromagnetic and ferroelectric phases caused by the piezoelectric and magnetostrictive effect.

The strategy of this work encompass: i) the preparation of porous thin films of ferroelectric barium titanate; ii) the synthesis of magnetic nanoparticles to be incorporated in the previous porous films and iii) the functionalization of the ferroelectric porous matrix aiming to fabricate multiferroic nano composite. The composite system $BaTiO_3$-$CoFe_2O_4$ was chosen due to the piezoelectricity of $BaTiO_3$, thus allowing strong elastic interaction between the two phases, and good magnetostriction of $CoFe_2O_4$. For materials synthesis, easy, environmental friendly and cost effective methodologies were adopted: i) evaporation induced self-assembly (EISA) assisted by dip-coating to prepare porous ferroelectric matrix; ii) hydrothermal synthesis to prepare magnetic nanoparticles and iii) electrophoretic deposition for functionalization.

The $BaTiO_3$ thin films were obtained using polystyrene-poly(ethylene oxide) block co-polymer (PS-b-PEO) as template to create porosity. The effect of a polymer with different molecular weights (Mw) in the creation of porosity, concentration of block co-polymer, type of annealing and withdrawal rate of the dip-coating were studied in this work. The porous microstructure of $BaTiO_3$ thin films were studied by SEM. Decomposition of the solvents and $BaTiO_3$ crystallization was studied by DTA/TGA. The topography and piezoelectric behaviour of porous films was analysed by AFM/ PFM.

$CoFe_2O_4$ nanoparticles were obtained by hydrothermal synthesis. The effect of temperature and time of the hydrothermal synthesis, the addition of polyvinylpyrrolidone (PVP) as additive with different concentrations, and effect of precipitating (NaOH) and Co^{2+}/Fe^{3+} concentration were studied in order to prepare nanoparticles with desired size and magnetic properties. The shape, size, dispersion and crystallinity of the nanoparticles were studied by various techniques such as TEM, BET and XRD. The crystallite size was calculated by Scherrer equation. The magnetic properties were evaluated by SQUID magnetometer. The results show that with the increase of temperature and time synthesis the particle and crystallite size increases too. The saturation magnetization depends of particles size, increasing with particle size increase. The increasing particle size from 12.9 to 16.1 nm provokes an increase in saturation magnetization from 53.7 to 73.2 emu/g. In time of hydrothermal synthesis studies, it was observed that a antiferromagnetic phase appear, hematite (α-Fe_2O_3). The presence of this phase damaged drastically the magnetic properties to 8.2 emu/g in the case of a sample prepared over 24 h. The PVP addition does not affect the shape of nanoparticles however favours their growth from 20.1 to 23.6. In term of magnetic properties, no influence was observed. The increase of Co^{2+}/Fe^{3+} and NaOH concentration induces growth of nanoparticles.

The functionalization of $BaTiO_3$ films was made by electrophoretic deposition (EPD). Initially, the process optimization was necessary by studying the different parameters related with deposition such as: applied voltage, deposition time and suspension type. This studies permits to conclude that with time increasing, the amount of nanoparticles deposited increases too. It was observed that, despite the optimization of EPD, it is important the use a good quality substrate that can afford voltage application.

palavras-chave

Filmes ferroelétricos porosos, nanopartículas ferromagnéticas, multiferroicos, síntese hidrotermal, deposição eletroforética.

resumo

Materiais multiferróicos são por definição materiais que exibem simultaneamente propriedades ferroelétricas e ferromagnéticas. Dado o seu potencial de aplicação tanto nos em dispositivos electrónicos existentes como em novos dispositivos devido ao seu carácter multifuncional, os materiais multiferróicos têm atraído consideravelmente o interesse da comunidade científica. Infelizmente os materiais multiferróicos existentes são raros e exibem propriedades bastante inferiores às necessárias para a sua aplicação. Assim é absolutamente fundamental desenvolver materiais multiferróicos compósitos. Em compósitos multiferróicos, o acoplamento magnetoelétrico deve-se à interação elástica entre as fases ferroelétrica e ferromagnética causada pelo efeito piezoeléctrico e magnetostritivo.

A estratégia deste trabalho engloba: i) a preparação de filmes finos porosos de titanato de bário ferroelétrico; ii) a síntese de nanopartículas magnéticas para serem incorporadas nos filmes porosos e iii) a funcionalização da matriz ferroelétrica porosa visando fabricar um nano compósito multiferróico. O sistema composto $BaTiO_3$-$CoFe_2O_4$ foi escolhido devido à piezoeletricidade do $BaTiO_3$, permitindo uma interação elástica forte entre as duas fases, e boa magnetostrição do $CoFe_2O_4$. Para a síntese dos materiais, foram adotadas metodologias simples, de baixo custo e amigas do ambiente: i) a *evaporation induced self-assembly* (EISA) assistida por *dip-coating* para preparar a matriz ferroelétrica porosa; ii) síntese hidrotermal para preparar nanopartículas magnéticas e iii) deposição eletroforética para a funcionalização dos filmes porosos.

Os filmes finos porosos de $BaTiO_3$ foram obtidos utilizando o co-polímero em bloco poliestireno-poli(óxido de etileno) - PS-b-PEO para criar a porosidade. Foram estudados os efeito da variação: i) do peso molecular do co-polímero; ii) da concentração do co-polímero em bloco; iii) do tipo de tratamento térmico e iv) da taxa de retirada da deposição por *dip-coating*. A microestrutura porosa dos filmes finos de $BaTiO_3$ foi estudada por SEM. A decomposição dos solventes e a cristalização do $BaTiO_3$ foram seguidas por análises térmicas. A topografia e o comportamento piezoeléctrico dos filmes porosas foram analisados por AFM/ PFM.

As nanopartículas de $CoFe_2O_4$ foram obtidas por síntese hidrotermal. Foram estudados o efeito da temperatura, do tempo da síntese hidrotermal, da adição de polivinilpirrolidona (PVP) como aditivo em diferentes concentrações, e os efeitos da concentração do agente precipitante (NaOH) e dos iões Co^{2+}/Fe^{3+} com o objectivo de preparar nanopartículas com tamanho e propriedades magnéticas adequadas. A forma, o tamanho, dispersão e cristalinidade das nanopartículas foram estudados através das técnicas TEM, BET e XRD. O tamanho da cristalite foi calculado pela equação de Scherrer. As propriedades magnéticas foram avaliadas por medidas de magnetização de SQUID. Os resultados mostram que aumento da temperatura e do tempo da síntese hidrotermal contribui para o aumento do tamanho da partícula e da cristalite. A magnetização de saturação aumenta com o aumento do tamanho das partículas. O aumento do tamanho das partículas de 12.9 para 16.1 nm provocou um aumento na magnetização de saturação de 53.7 para 73.2 emu/ g. Nos estudos do tempo de síntese hidrotermal observou-se o aparecimento de uma fase antiferromagnética, hematite (α-Fe_2O_3). A presença desta fase prejudicou drasticamente as propriedades magnéticas – 8.2 emu/ g, no caso da amostra preparada durante 24 h. A adição de PVP não afecta a forma das nanopartículas no entanto favorece o seu crescimento de 20.1 para 23.6 nm. Relativamente às propriedades magnéticas, nenhuma influência foi observada. O aumento da concentração de Co^{2+}/Fe^{3+} e de NaOH induz o crescimento de nanopartículas e, consequentemente, aumenta a magnetização de saturação.

A funcionalização dos filmes de $BaTiO_3$ foi feita por deposição eletroforética (EPD). Inicialmente, foi necessária a otimização do processo, estudando os diferentes parâmetros relacionados com a deposição, tais como: tensão aplicada, tempo de deposição e tipo de suspensão. Este estudo permitiu concluir que, com o aumento do tempo, a quantidade de nanopartículas depositadas também aumenta. Observou-se que, para fazer EPD, é importante o uso de um substrato de boa qualidade que seja estável à aplicação de tensão.

TABLE OF CONTENTS

INDEX OF FIGURES

INDEX OF TABLES

LIST OF SYMBOLS

A_{BET}	Specific surface area (measured by BET)
D_{TEM}	Average nanoparticles size (measured by TEM)
E	Electric field
H	Magnetic field
Hc	Coercive magnetic field
Mr	Remanent magnetization
Ms	Saturation magnetization
Mw	Block co-polymer molecular weight
Pc	Coercive electric field
Pr	Remanent polarization
Ps	Spontaneous polarization
Tc	Curie temperature

ABBREVIATIONS

ABC	Amphiphilic Block Co-Polymer
AFM	Atomic Force Microscopy
BET	Brunauer-Emmet-Teller
BTO	$BaTiO_3$ (Barium Titanate)
CAc	Citric Acid
CFO	$CoFe_2O_4$ (Cobalt Ferrite)
CMC	Critical Micelle Concentration
CTAB	Cetyltrimethylammonium Bromide
DTA	Differential Thermal Analysis
EDS	Energy Dispersive X-ray Spectrometer
EISA	Evaporation Induced Self-Assembly
EPD	Electrophoretic Deposition
EtOH	Ethanol
FWHM	Full Wight at Half Maximum
HS	Hydrothermal Synthesis
IUPAC	International Union of Pure and Applied Chemistry
JCPDS	Joint Committee on Powder Diffraction Standards
ME	Magnetoelectric
O/W	Oil in Water micro-emulsion
PEG	Polyethylene Glycol
PFM	Piezoresponse Force Microscopy
PLD	Pulsed Laser Deposition
PS-b-PEO	Polystyrene-Poly-(Ethylene oxide)
PTO	$PbTiO_3$ (Lead Titanate)
PVP	Polyvinylpyrrolidone
PZT	Lead Zirconate Titanate
SEM	Scanning Electron Microscopy
SQUID	Superconductor Quantum Interference Device

STO	$SrTiO_3$ (Strontium titanate)
TEA	Triethanolamine
TEM	Transmission Electron Microscopy
TGA	Thermal Gravimetric Analysis
THF	Tetrahydrofuran
W/O	Water in oil micro-emulsion

Introduction

1. Introduction

In 60's the computers were room-sized while nowadays the personal computers have 9 mm of thickness, Figure 1.1.

Figure 1.1 50 years old computer [1] (left) and 2000's notebook [2] (right).

Moore's law, in 1965, predicted the exponential increase of the power density associated with a decrease of size and power consumption of integrated circuits [3]. In the last decades "More and More Moore" has been the trend. However Moore's law is now reaching the limit and making power management and development of multifunctional materials for new devices an essential requirement of the microelectronic industry. Within this context, multiferroics can have an important role because of the simultaneous conjugation of electric and magnetic properties in the same physical volume, allowing the electric control of the magnetic response for storage and for processing (Figure 1.2).

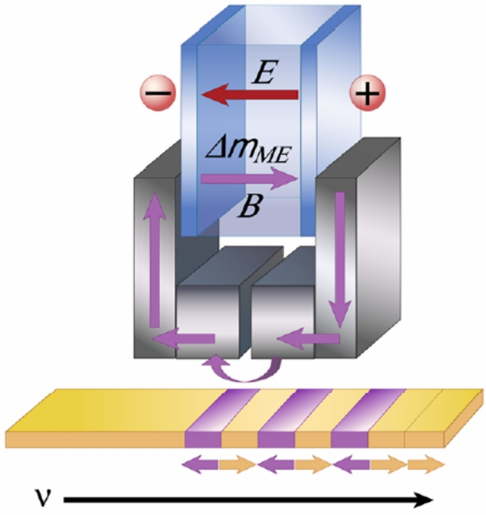

Figure 1.2 Scheme of a voltage-controlled write head at a magnetic hard disk track. The magnetic "write" field is generated by an electric field at the magnetoelectric (ME) material [4].

It should be emphasised that the use of, electric field controlled devices produces much less Joule heating than magnetic devices switched with a current, allowing an interesting thermal management [4].

The single-phase multiferroics are rare and exhibit weak magnetoelectric (ME) coupling or it occurs at very low temperature for practical applications [5, 6]. As an alternative, the composite multiferroic combining piezoelectric and magnetic phases together in a heterostructures, show strong direct responses to electric or magnetic fields [7]. However, the magnetoelectric coupling induced by strain due to piezoelectric and magnetostriction effect is still relatively weak due to the limitation by the mechanical adhesion of the component phases.

1.1. Objective

The aim of this work is to develop multiferroic nano composite thin films, exploiting low cost and environmental friendly chemical based processes for the preparation of ferroelectric thin films and magnetic nanoparticles. The strategy developed within this work encompass: i) the preparation of porous thin films, as ferroelectric matrix to be functionalized, ii) the synthesis of magnetic nanoparticles to be incorporated in the previous porous films and iii) the functionalization of the porous matrix aiming to fabricate multiferroic nano composite thin films for novel applications in electronics.

1.2. Structure of this thesis

The content of this thesis is divided into 6 chapters. The following chapter, chapter 2, is dedicated to the basic concepts related with ferroelectric, ferromagnetic and multiferroic materials, as well as the State of the Art in the latter materials.

In chapter 3, the strategy of this work is presented, proposing a alternative design for multiferroics materials in attempt to improve the magnetoelectric coupling. The experimental procedure and materials are described in chapter 4, which is divided into four subchapters: preparation of ferroelectric thin films, synthesis of ferromagnetic nanoparticles, functionalization of thin films with nanoparticles and characterization techniques. Chapter 5 describes and discuss the results. Conclusions and future work are presented in the final chapter.

Review: Multiferroic Materials

2. Review: multiferroic materials

2.1. Basic concepts

➢ *Multiferroic materials*

The term multiferroic, like the word itself (multi + ferroic), is used to describe materials that exhibit simultaneously at least two of the three ferroic properties: ferroelectricity, ferromagnetism or ferroelasticity [8, 9]. From the viewpoint of materials constituents, multiferroic materials can be divided in two types: single-phase [5] and composite [10] , which are described in sections 2.2 and 2.3, respectively.

Magnetoelectric coupling describes the influence of a magnetic field on the polarization and the influence of an electric field on the magnetization of a material. It may arise directly from the two order parameters in a single-phase material or indirectly via strain/stress as in multiferroic composite.

The coupling between the magnetic and ferroelectric order parameters leads to magnetoelectric effects, in which the magnetization can be tuned by an applied electric field and polarization can be tuned by an applied magnetic field. Figure 2.1 shows the relationship between multiferroic and magnetoelectric coupling [9]. Ferromagnets (ferroelectrics) form a subset of magnetically (electrically) polarizable materials such as paramagnets and antiferromagnets (paraelectrics and antiferroelectric). The intersection (red hatching) represents materials that are multiferroic. Magnetoelectric coupling (blue) is an independent phenomenon that can arise in any of the materials that are both magnetically and electrically polarizable [9].

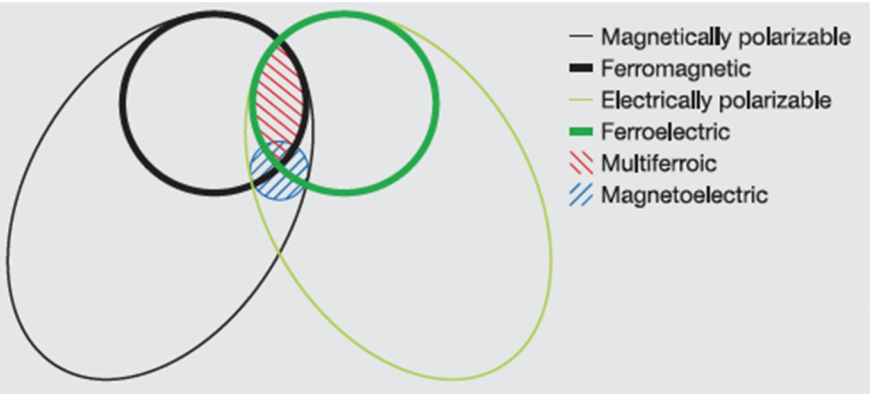

Figure 2.1 Relationship between multiferroic and magnetoelectric materials [9].

➢ *Ferroelectricity*

Ferroelectricity is a property of materials which exhibit spontaneous electric polarization that can be reversed by an external electric field [11]. This polarization could be associated to the movements of cations in relation to anions. When an electric field is applied, orientation of dipoles creating domains of polarization occurs and this polarization remains even when the electric field is removed [12]. As the temperature is increased, a ferroelectric undergoes a phase transition, which is accompanied by the disappearance of spontaneous polarization due to a change in the symmetry of the crystal lattice. The temperature at which a phase transition occurs is called Curie temperature, T_C.

Most of the known ferroelectric materials have (above Tc) a cubic perovskite ABO_3 structure with smaller "B" cations at the centre of the oxygen octahedron and larger "A" cations at the corner of the unit cell, Figure 2.2. Atoms of Pb, Ba, Ca, Sr typically occupy A-sites while Ti, Nb, Mg or Ta can be located at the B-site of the perovskite structure. Compounds like $BaTiO_3$ and $PbTiO_3$ are examples of ferroelectric materials [11-15]. Below the Curie temperature there is a structural distortion to a lower symmetry phase accompanied by the off-centre shift of "A" or "B" cations relative to the "O" anions. The spontaneous polarization of the lower symmetry ferroelectric phase is due to the dipole moment created by the shift of cations with respect to the anions [16].

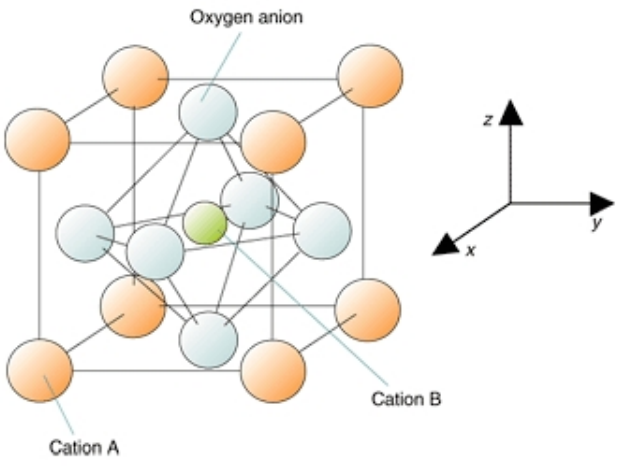

Figure 2.2 Crystallographic structure of ABO_3 perovskite, adapted from Ref. [17].

The response of ferroelectric domains to an external electric field applied on ferroelectric material can be described by the so-called ferroelectric hysteresis loop, illustrated in Figure 2.3.

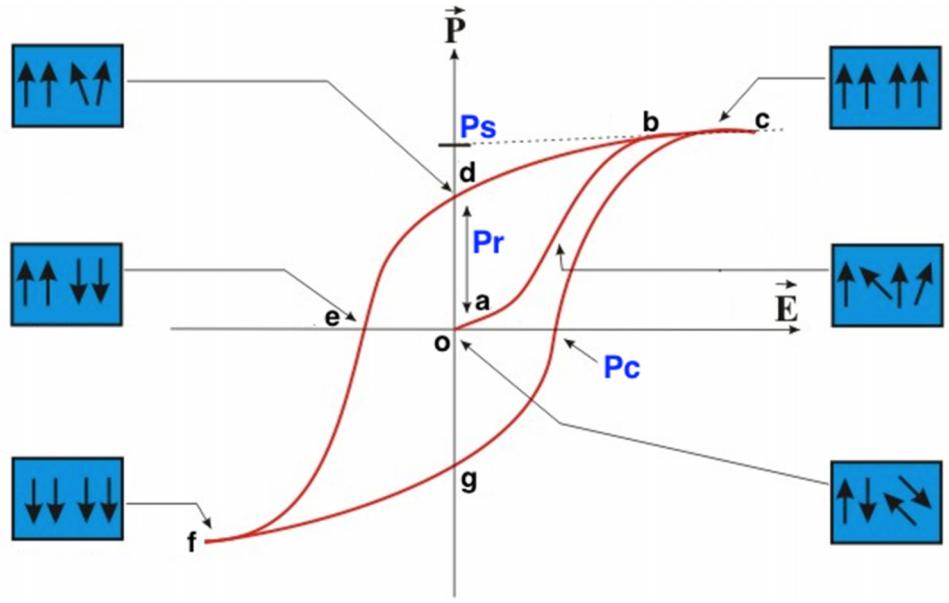

Figure 2.3 Ferroelectric hysteresis loop (polarization vs. applied electric field), adapted from Ref.[16].

Several points of the ferroelectric hysteresis loop are of interest: the spontaneous (*Ps*) and remanent (*Pr*) polarization, the coercive field (*Pc*) and the general shape of the loop. In a ferroelectric material, when all of the dipole moments are aligned, the material is considered saturated since an increase in the applied electric field will not increase more the polarization (segment *b*-*c*). The linear extrapolation of the curve back to the polarization axis ($\vec{P}$) represents the spontaneous polarization (*Ps*). As the applied electric field is reduced from its maximum positive value to zero, some dipole moments will remain aligned, and a remanent (P_r) polarization is observed. As the applied electric field spans the range from its maximum positive to negative values, *-Ps* and *-Pr* will be observed (*f* and *g* points in Figure 2.3, respectively). In this state, all of the dipole moments will be switched from the positive to the negative (up to down arrows) as shown in the blue boxes of the Figure 2.3.

All ferroelectric crystals are necessarily piezoelectric. The piezoelectricity effect is a phenomenon resulting from a coupling between the electrical and mechanical properties of a material. There are two types of piezoelectric effect: direct and inverse. In a direct piezoelectric effect, when a mechanical stress (designated by *F* in Figure 2.4) is applied to a piezoelectric material, an electric potential will be generated.

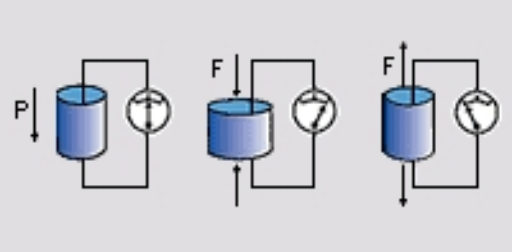

Figure 2.4 Direct piezoelectric effect: mechanical stress applied results in a voltage [18].

In case of inverse piezoelectric effect, when a voltage is applied to the piezoelectric, a mechanical strain will occur (Figure 2.5).

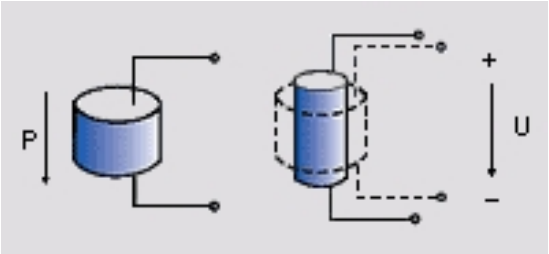

Figure 2.5 Inverse piezoelectric effect: voltage applied results in a deformation [18].

The basic equations 1.1 and 1.2 describe these two effects, respectively, in regard to electric and elastic properties:

$$D_i = \varepsilon_{ij}^{T} E_j + d_{ijk} T_{jk} \qquad \text{Eq. 1.1}$$

$$S_{ij} = d_{ijk} E_k + s_{ijkl}^{E} T_{kl} \qquad \text{Eq. 1.2}$$

where, D is the dielectric displacement vector, ε is the tensor of dielectric constants (superscript T indicates a constant stress), E is the electric field vector, d is the tensor of piezoelectric constants, T is the mechanical stress, S is the mechanical strain tensor and s is the tensor of mechanical compliance (superscript E indicates a constant electric field) [19]. Piezoelectric materials are utilized in transducers, devices that convert electrical energy into mechanical strains, or vice versa. Applications that employ piezoelectrics include, among others, microphones, ultrasonic generators, sonar detectors.

➢ *Ferromagnetism*

The elements iron, cobalt and nickel, together with some of the rare-earth elements, possess at sufficiently low temperature a magnetic moment even in the absence of an applied field. This property characterised by a spontaneous magnetization is known as ferromagnetism [20]. Permanent magnetic moments result from atomic magnetic moments due to electron spin-uncancelled as a consequence of the electron structure. Only atoms with partially filled shells with unpaired spins can exhibit a net magnetic moment in the absence of an external magnetic field. Furthermore, in a ferromagnetic material, coupling interactions cause net spin magnetic moments of adjacent atoms to align with another, even in the absence of an external field. This mutual spin alignment exists over relatively large volume regions of the crystal called magnetic domains, Figure 2.6.

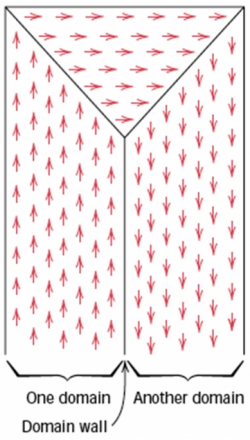

Figure 2.6 Schematic representation of domains in a ferro- or ferrimagnetic material. Arrows represent atomic magnetic dipoles. Within each domain, all dipoles are aligned, whereas the direction of alignment varies from one domain to another [21].

According to the response to the external magnetic field, the material can be classified into: ferromagnetic, paramagnetic, antiferromagnetic or ferrimagnetic [22]. In ferromagnetic materials, the electron spins are aligned parallel to each other at absolute zero, Figure 2.7. However, this behaviour depends on the temperature. When a certain temperature is reached the ferromagnetism completely disappears and the material becomes paramagnetic. This temperature is called Curie temperature. If the material is cooled above its Tc the ferromagnetic domains reform and the materials becomes ferromagnetic again. In contrast to ferromagnetic, an antiferromagnetic behaviour corresponds to an antiparallel alignment of

equal moments. Finally, ferrimagnetic behaviour is characterized by antiparallel moments having different magnitudes.

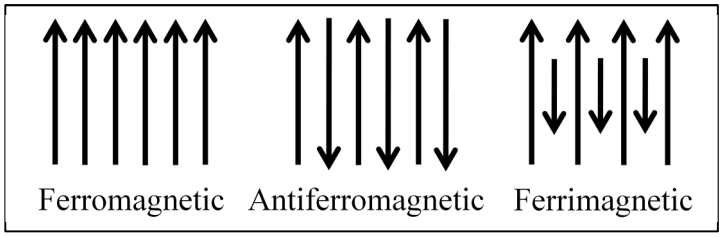

Figure 2.7 Different alignments of magnetic dipoles. Adapted from Ref.[22].

The application of a relatively small external magnetic field changes the domain arrangement, and hence induces an appreciable change in magnetization. Both ferro- and ferrimagnetic materials exhibit a hysteric response to an external magnetic field, as shown in right side of Figure 2.8.

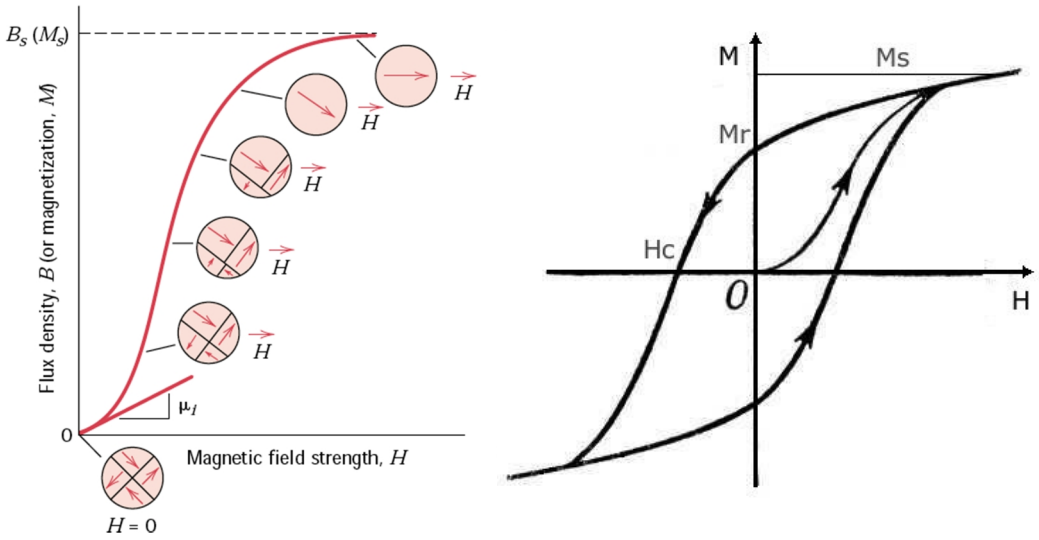

Figure 2.8 Domain configurations during several stages of magnetization (left side) and ferro/ferrimagnetic hysteresis loop (right side), adapted from Ref. [21].

During the magnetization of a ferro/ferrimagnetic material, as the applied magnetic field increases from zero, magnetization value increases from zero and achieves saturation magnetization, *Ms*. At this point, all magnetic domains are aligned. While decreasing the

applied field to zero, the original magnetization curve is not retraced, and it remains the magnetization called remanent or residual magnetization. To decrease the magnetization to zero, it is required to apply a negative magnetic field with H_C value, called coercive field. When the negative applied field is increased even more, the material achieves saturation magnetization in reverse field, i.e. all magnetic moments are aligned but in opposite direction to *Ms*. Upon removing the reverse field, the magnetization returns to the remanent value. If the magnetic field is continuously increased the magnetization will saturate again closing the hysteresis loop.

The size and shape of the hysteresis loop is of considerable practical importance. Based on the value of a coercive field, magnetic materials are classified into hard for high H_C and soft magnets for small values of H_C [20]. Soft magnetic materials are used in devices that are subjected to alternating magnetic field. It can achieve high magnetization with low values of magnetic field (*i.e.* it is easily magnetized and demagnetized). On the other hand, the hard magnetic materials have high values of coercive field, thus utilized in permanent magnets (for example memory storage) due to a high resistance to demagnetization.

Similar to piezoelectric effect on ferroelectric materials, if ferromagnetics will have a mechanical response when a magnetic field is applied, the phenomenon is called magnetostriction [20]. When an applied field changes a state of magnetization of a ferromagnetic material, it occurs a small change in its dimensions, provided by two reasons: i) domain wall migration in response to an external magnetic field and ii) domain rotation. The linear magnetostriction λ can be defined as

$$\lambda = \frac{\Delta l}{l} \qquad \text{Eq. 1.3}$$

where l is the original length of the specimen and Δl the magnetostrictive change.

2.2. Single-phase multiferroics

By definition, a single-phase multiferroic shows simultaneously ferroelectricity and ferromagnetism in a unique compound. There are very few single-phase multiferroic materials such as $BiFeO_3$ [23-25], $BiMnO_3$ [26-28], $YMnO_3$ [24, 29-31].

The most widely single-phase studied multiferroic is bismuth ferrite, $BiFeO_3$ (Figure 2.9) [24, 32].

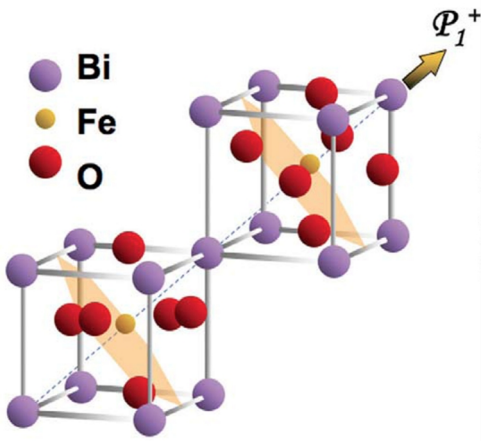

Figure 2.9 Schematics of the crystal structure of $BiFeO_3$ with polarization arrow in [111] direction and antiferromagnetic plan (shaded plans) [33].

The structure of $BiFeO_3$ can be characterized by distorted perovskite with rhombohedral symmetry and space group R3c. The primitive unit cell, shown in Figure 2.9, contains two formula units (10 atoms in total), arising from counter-rotations of neighbouring O octahedral about the [111] axis. The R3c symmetry permits the development of a spontaneous polarization along [111], and Bi, Fe and O are displaced relative to one another along this threefold axis. Therefore, the ferroelectric state is realized by a large displacement of the Bi ions relative to the FeO_6 octahedra. The Fe magnetic moments are coupled ferromagnetically within the pseudocubic (111) planes Figure 2.9. If the magnetic moments are oriented perpendicularly to the [111] direction, the symmetry also permits a canting of the antiferromagnetic sublattices resulting in a macroscopic magnetization, so-called weak ferromagnetism [5, 24, 34].

Some studies were carried out about polarization of single-phase multiferroic materials thin films and bulk. Teague et al. [35] published the first studies of polarization of bulk $BiFeO_3$ in 1970. These measurements were made at 77 K revealing a spontaneous polarization of ~6.1 $\mu C/cm^2$ along the 111-direction. Nowadays the measured values are converging to ~90 $\mu C/cm^2$ along the [111] direction of the pseudo-cubic perovskite unit cell, consistent with first-principles calculations made by Neaton et al. [36].

2.3. Composite multiferroics

Composite multiferroics consist of two different phases, a ferroelectric and a ferro-ferrimagnetic. To date, depending on the architecture of the composite, namely the design of the interface-connectivity between the two components, three different heterostructures have been studied: particulate, horizontal and vertical, as represented in Figure 2.10. An internationally accepted notation, first established for a series of composites by Newnham *et al.* [37] helps to describe and distinguish the connectivity character, using the dimensionality of each phase. Thus, in the particulate case with 0D particles dispersed into a 3D matrix corresponds to 0-3 connectivity (Figure 2.10a), in the horizontal heterostructure, with 2D alternating layers correspond to a 2-2 connectivity (Figure 2.10b), while the vertical heterostructure, with 1D nanopillars dispersed to a 3D matrix, corresponds to a 1-3 structure (Figure 2.10c).

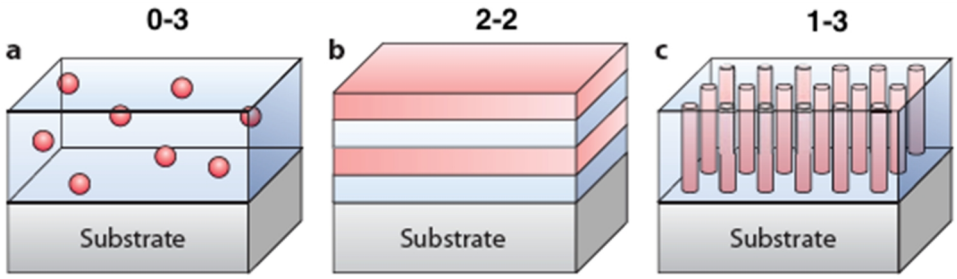

Figure 2.10 Schematic illustration of three kinds of multiferroic composites nanostructures: a) 0-3 Particulate, b) 2-2 Horizontal heterostructure and c) 1-3 Vertical heterostructure [10].

In 1972, van Suchtelen [38], in an attempt to describe the rising magnetoelectric (ME) effect in this kind of composites, proposed for the first time the concept of the product property, using the case of $BaTiO_3$ and $CoFe_2O_4$ (equations 1.4 and 1.5). This concept can be described as a "chain" reaction taking place between the two phases and yields the direct and the converse ME effect. When a magnetic field is applied, occurs a mechanical strain in the ferromagnetic phase, subsequently transferred to the ferroelectric one generating polarization (Eq. 1.4, Figure 2.11a). The second case claims the application of an electric field, which provokes mechanical strain to the ferroelectric phase and, analogously to the prior case, evoking magnetization to the ferromagnetic counterpart (Eq. 1.5, Figure 2.11b). The direct and the converse ME effect can be described, respectively, by the equations [39]:

$$ME_H = \frac{magnetic}{mechanical} \times \frac{mechanical}{electric} \quad \text{Eq. 1.4}$$

$$ME_E = \frac{electric}{mechanical} \times \frac{mechanical}{magnetic} \quad \text{Eq. 1.5}$$

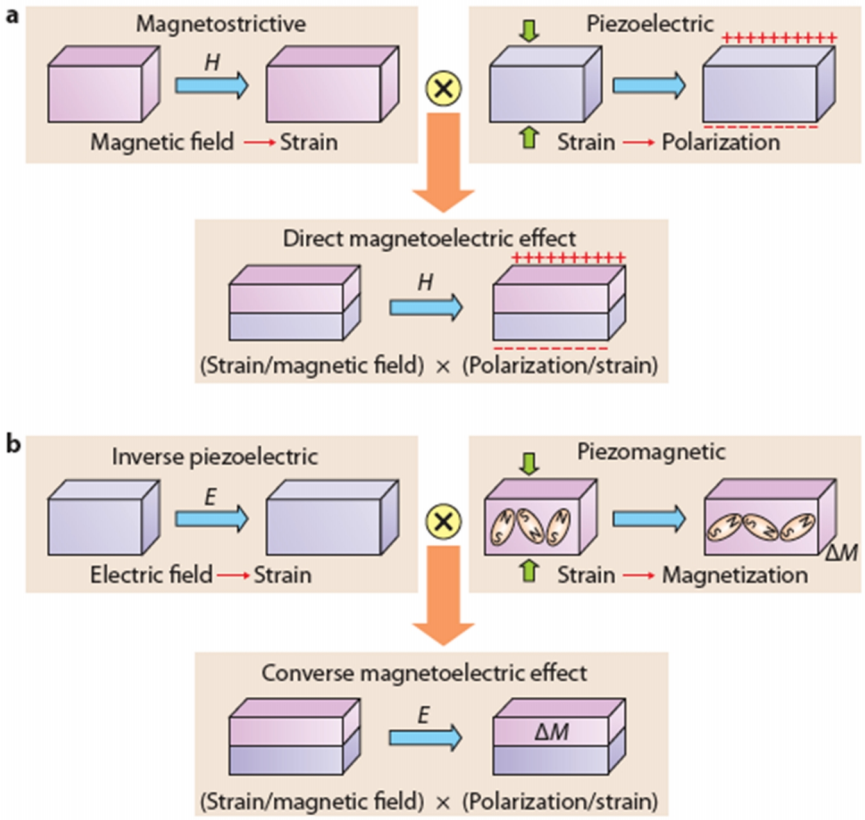

Figure 2.11 Schematic illustration of strain-mediated ME effect in a composite system consisting of a magnetic layer (purple) and ferroelectric layer (pink). (a) Represents a direct magnetoelectric effect and (b) represents a converse magnetoelectric effect [10].

2.3.1. Horizontal heterostructures

The horizontal heterostructures, or else 2-2 composites, are the most widely studied, because they can be easily fabricated layer-by-layer and integrated in the devices. The thickness of the layers could be modulated at the nanometer level.

The highest ME voltage coefficient ever measured was achieved with laminate mm-thick Terfenol-D/PZT composites, prepared by conventional methods and reached 4680 mV cm^{-1} Oe^{-1} [40]. However, the ever-increasing demand for miniaturization has led to focus the investigation on thick and thin films.

Concerning the materials of the current investigation, $CoFe_2O_4$ (CFO) and $BaTiO_3$ (BTO), in 2008 Wang *et al.* [41] grew BTO thin films (260 nm thick) by Pulsed Laser

Deposition technique (PLD) on CFO substrates, achieving ME voltage coefficient of 38 mV cm^{-1} Oe^{-1}. A little bit earlier the same year, Zhang et al. [42], also using PLD, deposited BTO and CFO thin films, 70 nm and 20 nm thick respectively, on $SrTiO_3$ (STO) substrates, achieving ME voltage coefficient of 104 mV cm^{-1} Oe^{-1}. The viable mechanism of ME coupling comes from strain-coupling among the piezoelectric and magnetostrictive components of heterostructure. In case of horizontal heterostructures, the clamping effect of the substrate effectively suppresses any in-plane strain in the film. Theoretically, this limitation is minimized in vertical heterostructures if the contact area of the film with the substrate is lower than the interface area within the composite.

2.3.2. Vertical heterostructures

The most common composition of vertical or 1-3 heterostructures are magnetic spinel nanopillars embedded into a ferroelectric perovskite matrix, usually epitaxially grown [24]. The high interfacial surface area together with intrinsic three-dimensional heteroepitaxial character (ferroelectric, ferromagnetic and substrate lattice match) result in strong coupling between the two ferroic components. The most important advantage of 1-3 heterostructures is the substantially low mechanical clamping effect related to the lattice constraint from the substrate.

In 2004, Zheng *et al.* [7] grew CFO nanopillars of 20-30 nm diameter in BTO thin film on STO substrate, by PLD technique and proved the magnetoelectric behaviour by detecting a sharp change in magnetization at the Curie temperature. By the same procedure, Zavalinche *et al.* [43] composed CFO nanopillars in 200 nm thick $BiFeO_3$ (BFO) films on STO substrate, which corresponded to a magnetic susceptibility of 10^{-2} G cm/V, similar to single crystalline bilayered composites. More recently, Yan *et al.* [44] measured ME voltage coefficient of 20 mV cm^{-1} Oe^{-1}, for CFO/BFO/STO (nanopillar/matrix/substrate) thin films of about 150-240 nm thick.

The vertical heterostructures present in general better ME coupling than the horizontal structures, however the coupling is still too low for practical uses. It is essential to develop alternative architectures to prepare multiferroic composite thin films that can ensure a good control of the interfaces between ferroelectric and ferromagnetic phases.

Strategy of this thesis

3. Strategy of this thesis

3.1. Introduction

As discussed before, the actual multiferroic composite architectures show low magnetoelectric coupling. The aim of this work is the development of an alternative architecture of multiferroic composites using simple and low cost methodologies. This alternative architecture consists of a porous thin film as ferroelectric matrix functionalized with ferromagnetic nanoparticles (Figure 3.1).

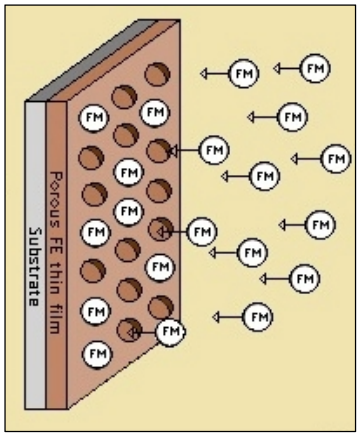

Figure 3.1 Porous ferroelectric matrix functionalization with ferromagnetic nanoparticles.

The inspiration to this proposal comes from the use of lyotropic liquid-crystal phases as templates to develop porous structures [45]. These materials have ordered and porous structure with high specific surface areas and can be interesting matrices for the preparation of multiferroic composite with large interface areas. The idea is to prepare porous ferroelectric thin films, which would be later functionalized with ferromagnetic nanoparticles to form a multiferroic composite material.

3.2. Porous ferroelectric thin films

Traditionally porosity is undesired in electroceramics because it usually degrades the electrical and mechanical properties of the material. However, for certain applications, porosity may be an advantage, such as for pyroelectric applications where is required a material with piezoelectric properties but at the same time with low dielectric constant.

Sensors and actuators are some examples of potential applications [13, 46-50]. Furthermore, these porous structures can be seen as an avenue to achieve lighter materials giving the opportunity to further use the voids to incorporate other functionalities in the same volume. This is the case of the present work. Porous thin films can be interesting to develop multiferroic materials, by incorporating ferromagnetic nanoparticles in the pores of a ferroelectric matrix.

Thin films can be prepared through a great number of different techniques (Figure 3.2). However, only some of them are able to produce porous thin films. The physical deposition techniques are preferred in order to prepare dense thin films and chemical deposition approaches are much more appropriate to the preparation of porous layers.

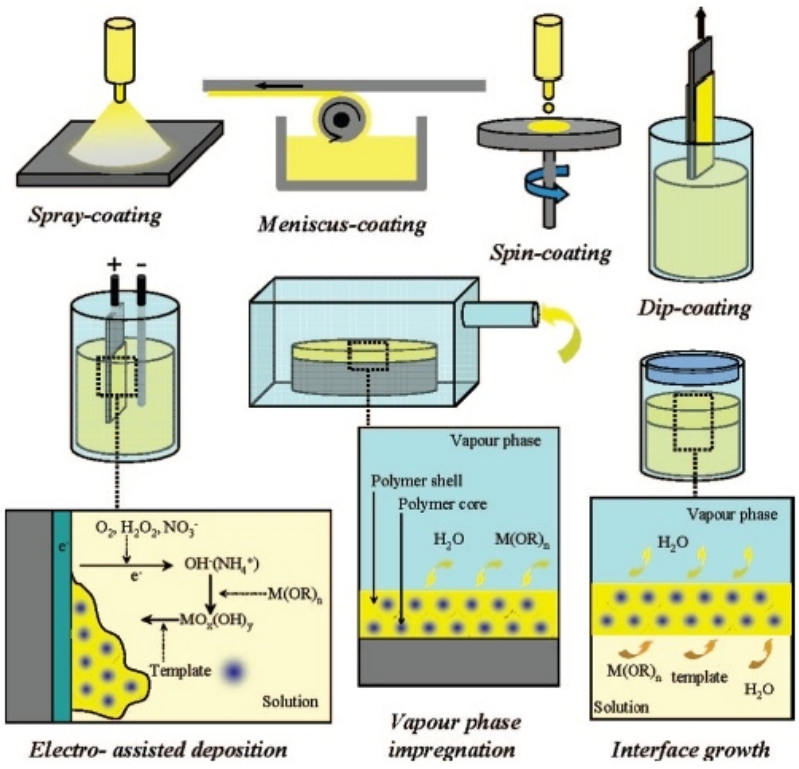

Figure 3.2 Various processing methods used to prepare porous thin films [51].

From chemical deposition techniques, spin-coating and dip-coating are commonly used in electronics and optics industries for instance, to prepare inorganic layers from sol-gel solutions. Each technique has advantages and drawbacks. For example, dip-coating, in which the substrate is successively dipped into the solution and withdrawn at a constant speed, offers a good control of the thickness and produces no waste. However, the spin-coating is preferred if one wants only one face to be deposited.

Some reported works describe the preparation of porous films by dip-coating and spin-coating [13, 48, 49, 52-54].

To obtain an optimised pyroelectric response of a material (figure of merit), porosity as been considered since it will decrease the dielectric constant [49]. Porous lead zirconate titanate (PZT) thin films were prepared by spin-coating of sol-gel solutions [48, 49, 52]. The porosity was generated by using a polymer and could be controlled by using polymers with different molecular weights. Stancu *et al* [52] studied two different ways to produce porous films by spin coating: (1) hydrolysis of precursor solution and (2) the addition of organic macromolecular polyvinylpyrrolidone (PVP). In case of hydrolysis, the authors suggested that the porosity should develop when either the water or the solvent has been removed during the pyrolysis step. For PVP case, the pores were produced after pyrolysis of PVP, which was realised at high temperature. The ferroelectric properties of the porous PZT films were compared to the equivalent dense PZT films and the properties were by far lower. The dielectric permittivity decreases from 348 for dense film to 48 for porous films. Later, Stancu *et al.* [48] published another study describing the effect of porosity on ferroelectric properties of PZT films. In this work, the authors prepared porous films with addition of different amounts of PVP. The pore size increased by increasing the amount of polymer added to precursor solution and this fact has an effect on the final film thickness. The addition of PVP makes the starting solution more viscous leading to an increase of thickness after crystallization. The pores size increased with increasing PVP, and lead to a high shrinkage of the film during crystallization annealing. The electrical measurements showed that the presence of porosity in the films leads to a lower capacitance and lower dielectric constant. The authors suggested that these films are good candidates for pyroelectric applications due to its lower permittivity (characteristic property). The porosity in these films is completely random.

The group of C. Sanchez have reported several papers on the fabrication of metallic and multimetallic oxides porous thin films [13, 46, 47, 53, 54]. The methods used to obtain porous thin films are evaporation induced self-assembly (EISA) combined with dip-coating of sol-gel solutions. EISA can be described like the conjugation of two cooperative effects. During the evaporation of the sol-gel solution containing the inorganic precursors and surfactant, the self-assembly of inorganic species occurs around the surfactant micelles leading to mesophase formation, Figure 3.3.

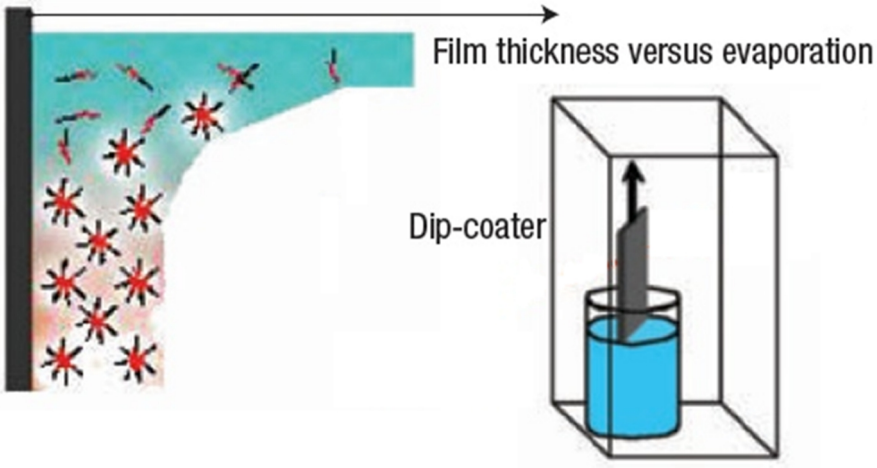

Figure 3.3 Scheme of Evaporation-induced self-assembly associated to dip-coating, adapted from Ref. [47].

The as-prepared thin films are xerogels where the organic template are embedded into the inorganic matrix. The thermal treatment step is necessary after the deposition due to three important facts: i) it conducts to the stabilization of the mesophase, ii) decomposition and elimination of the organic phase creating the porosity and iii) crystallization of the network (Figure 3.4). The crystallization occurs through nucleation and growth of crystallized seeds and is followed by diffusive sintering if sufficiently high temperature is maintained long enough. A fast nucleation leads usually to a large number of seeds created homogeneously into the inorganic network. Their subsequent growth into nanocrystallites is made by diffusion of the adjacent atoms towards the nucleus surface to occupy atomic sites of lower energy.

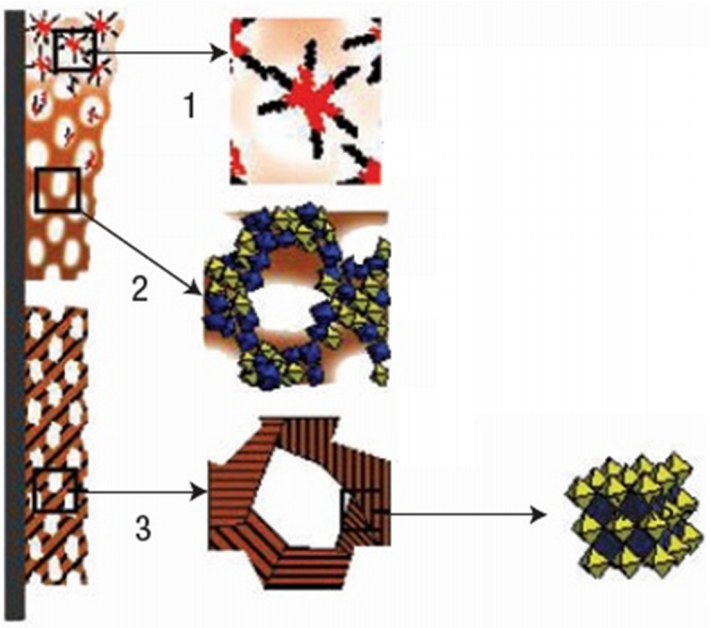

Figure 3.4 Thermal treatment step involving: (1) pre-consolidation, (2) template removal and (3) inorganic network crystallization, adapted from Ref. [47].

A. Fisher *et al.* [53] prepared well-ordered nanoperforated TiO_2 layers by EISA combined with dip-coating and studied the effect of molecular weight of surfactant on the pores size. The higher molecular weight surfactants originated the biggest pores. The authors suggest that the formation of such systems is possible through the precise balance of the interactions between the surfactant micelles, inorganic precursors, solvent phase and interfaces (film/air and film/substrate) during the different steps of evaporation drying and thermal treatment.

Investigation of dip-coating of various sol-gel solutions using different withdrawal speed conditions were reported by Faustini *et al.* [54]. At low withdrawal speeds, the film thickness is governed by the interdependence of continuous evaporation of the solvent at the meniscus and the capillary rise at the drying line. At high speeds, the final thickness is mainly dependent on the viscous drag. At intermediate speeds, both phenomena, overlap and a critical speed, were found. Furthermore, a thickness lower limit exists that cannot be overcome, except by dilution of the initial solution *i.e.*, thinner films can be obtained with high diluted solutions and/or by using at ultralow withdrawal speeds.

More recently, P. Ferreira *et al.* [13] reported the first study on synthesis and measurements of ferroelectric properties of porous $PbTiO_3$ (lead titanate - PTO) and $BaTiO_3$ films. The thermal processing used to convert the amorphous porous mesostructured multimetallic oxide thin films into a crystalline perovskite film is a key

point to achieve both size and shape monodispersity in particles and pore sizes and in keeping nanoporosity. The obtained films showed piezoelectric and ferroelectric response, measured at the nanoscale. The authors suggested that these films are highly promising as platforms to construct multifunctional ordered distributed composite materials in which the original architecture of the pores are filled just before crystallization.

PZT and PTO are both good ferroelectric and piezoelectric materials, but they have lead in their constitution, which is a non-environmental friendly element. Nowadays, the scientific community has been paying special attention to develop substituents for lead based materials – the so-called *lead-free materials*. BTO is a good example of lead-free ferroelectric material. It is a well-know ceramic capacitor dielectric material for electronic industry due to its high dielectric constant [11].

Like referred in section 2.1-*Ferroelectricity*, BTO is a ferroelectric material with perovskite structure, Figure 3.5. Eight atoms of Ba^{2+}, one atom of Ti^{4+} and six atoms of O^{2-} compose the $BaTiO_3$ unit cell.

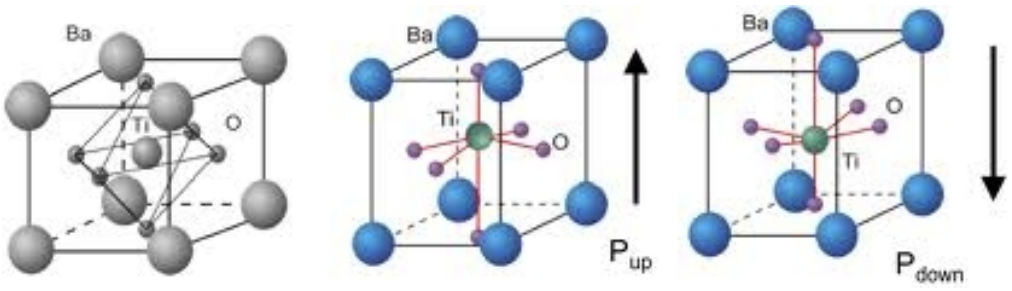

Figure 3.5 $BaTiO_3$ unit cell with a schematic representation of the possible developed polarization upon the application of an electric field.

Figure 3.6 shows 3 different phase transitions of barium titanate. The arrows indicate the direction of polarization. Above the Curie temperature, BTO crystal possesses cubic structure (space group Pm3m). Below the Curie temperature (120°C), the crystal turns into tetragonal (P4mm). Between 5°C and -90°C the structure is orthorhombic (Amm2), and rhombohedral (R3m) below of -90°C.

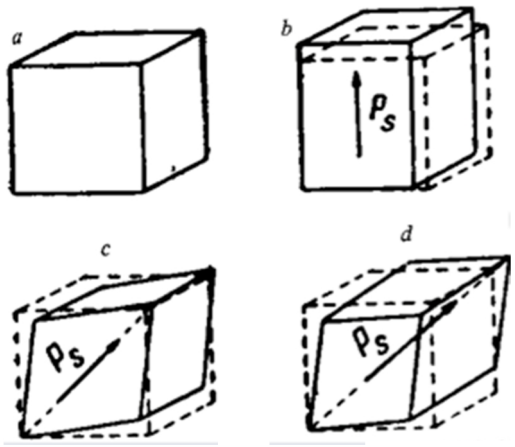

Figure 3.6 $BaTiO_3$ unit cell in different crystallographic phases: a) cubic, b) tetragonal, c) rhombic and d) rhombohedral cell [15]. The arrows indicate the direction of spontaneous polarization (*Ps*).

The cubic structure is the only one does not show ferroelectric properties and it is paraelectric because the vibrations in the cubic structure promotes the random displacement of Ti^{4+} ion around its central position, there does not show any asymmetry or polarization. In the case of the tetragonal system, Ti^{4+} ion and the octahedral arrangement of O^{2-} ions move asymmetrically causing a permanent electric dipole moment in the unit cell. Knowing that the oxygen octahedra are coupled, the neighbouring unit cells will also be polarized yielding domain structures. These domains are characterized by small volumes of material in which the electric dipole moments are aligned in the same direction.

3.3. Ferromagnetic nanoparticles

Magnetic nanoparticles have attracted tremendous attention due to their novel properties and their potential applications in magnetic recording, magnetic storage, biotechnology and biomedicine [55, 56]. For example, in the case of magnetic recording applications a large remanent magnetization and moderate coercivity is required [57]. For some of these mentioned applications of magnetic nanoparticles, the soft ferrites, such as magnetite and maghemite, are thought to be the most suitable [20]. Cobalt ferrite, $CoFe_2O_4$, is a hard ferrite and displays some interesting characteristics in order to compose a multiferroic material: good chemical stability, high magnetocrystalline

anisotropy and large magnetostriction [20, 58]. The saturation magnetostriction (λs) of various materials at room temperature is given in Table 3.1.

Table 3.1 Saturation magnetostriction of various materials at room temperature, adapted from Ref. [20].

Material	**Saturation magnetostriction λs (10^{-6})**
Iron	-7
Nickel	-33
Magnetite, (Fe_3O_4)	+40
Cobalt ferrite	-110
$SmFe_2$	-1560
Terfenol D ($Tb_{0.3}Dy_{0.7}Fe_{1.93}$)	+2000

The high values of saturation magnetostriction of $SmFe_2$ and Terfenol D are due to the highly anisotropic shapes of Sm and Tb ions and to the large lanthanide-iron exchange energy. Comparing the cases of magnetite and cobalt ferrite, the high magnetostriction in materials containing cobalt is due to the presence of the Co^{2+}, from which there is a large orbital contribution to the magnetic moment and hence a strong spin-orbit coupling, which increases the magnetostriction. The properties of cobalt ferrite depend on the morphology and preparation method.

Some methods have been studied to obtain magnetic nanoparticles such as: co-precipitation [59, 60], thermal decomposition [61-63], micro-emulsion [64-66], solvothermal and hydrothermal synthesis.

- **Co-precipitation**

Co-precipitation, or wet chemical route is a facile way to synthesize iron oxides composed from aqueous ionic salt solutions by the addition of a base under inert atmosphere at room or elevated temperature. However, after the precipitation an annealing step is necessary to crystalize the material. The particles prepared by co-precipitation tend to be rather polydisperse and with low magnetic properties when compared with other processes. Zhang et al [59] prepared $CoFe_2O_4$ nanoparticles by co-precipitation method. The authors studied the effect of base concentration (NaOH) and annealing temperature. They observed that for high concentrations of NaOH and higher

annealing temperatures the crystallite size was higher. The results obtained are summarised in Table 3.2.

Table 3.2 NaOH concentration and annealing temperature effect on crystallite size and saturation magnetization of $CoFe_2O_4$ nanoparticles.

NaOH conc. (M)	Annealing temperature (°C)	Crystallite size (nm)	Ms (emu/g)
0.4	*	27	39.94
1.0	*	38	30.18
1.6	*	50	29.79
4.8	*	69	33.45
4.8	200	*	30.41
4.8	300	*	24.41
4.8	600	*	53.69
4.8	1000	*	86.34

* Not done/measured

The lower magnetization of samples obtained with 4.8 M of NaOH and annealing at 200 and 300 °C can be related with the presence of Fe_2O_3 and γ - Fe_2O_3 and an outer layer with thickness around 10 nm appearing on the surfaces of each nano-particle. The products annealed above 600 °C showed that most particles have sizes larger than 100 nm, but they were polydisperse.

- **Thermal decomposition**

Thermal decomposition is the decomposition of organometallic compounds in high-boiling organic solvents containing stabilizing surfactants. The typical surfactants are fatty acids [61, 62] or PVP [63]. The size and morphology of magnetic nanoparticles could be controlled by the ratio of the starting reagents including organometallic compounds, surfactant, and solvent. An annealing step is needed in order to obtain crystalline material. Cabrera *et al.* [61] synthesized cubic nanoparticles of MFe_2O_4 (M= Fe, Co and Mn) by thermal decomposition of Fe(III), Co(II) and Mn(II) oleates. The authors observed that the size of ferrite nanoparticles could be controlled by varying the amount of metal-oleate complex in the reaction mixture. The particle size was proportional to the concentration of metal-oleate. For the case of CFO, the morphology of

the particles changed from cubic to spherical with modification of Co-oleate concentration. This fact is related with the growth rates. Faster growth rates lead to spherical Co ferrite nanoparticles. Therefore, high concentration of metal cations is responsible for faster growth rates. Cobalt ferrite with mean size 12 nm shows 54 emu/g of saturation magnetization at 5 K and 50 emu/g at 290 K.

- **Micro-emulsion**

A micro-emulsion is an isotropic and thermodynamically stable single phase formed by at least three components; two of them are non-miscible, and the third one, called surfactant, is characterized by amphiphilic properties [65]. Depending on the proportion of suitable components and on the hydrophilic-lipophilic balance value of the surfactant used, it occurs the formation of microdroplets can be in the form of oil in water (O/W) or micro-emulsion of water in oil (W/O). In W/O microemulsions, the aqueous phase is dispersed as microdroplets surrounded by a monolayer of surfactant molecules [67]. The size of the micelle is determined by the molar ratio of water to surfactant [66]. By mixing two identical water-in-oil microemulsions containing the desired reactants, the microdroplets will continuously collide, coalesce and break again, and finally a precipitate is formed in the micelles. By the addition of solvent, such as acetone or ethanol, to the microemulsions, the precipitate can be extracted by filtering or centrifuging the mixture. The micro-emulsion can be named as a nanoreactor for the formation of nanoparticles.

Liu *et al.* [68] prepared $CoFe_2O_4$ nanoparticles by micro-emulsion method. The size of nanoparticles (from 4nm to 10nm) was controlled by concentration of the reagents. The saturation magnetization increased from 15 to 50 emu/g with particle size increase.

- **Hydrothermal synthesis**

Hydrothermal processing can be defined as a heterogeneous reaction on the presence of aqueous solvents under high pressure and temperature conditions that allow the dissolution and recrystallization of materials that are relatively insoluble under ordinary conditions [69]. When a non-aqueous solvent is used, the process is so-called solvothermal synthesis [70, 71]. During the hydrothermal treatment metallic cations initially precipitate in the form of hydroxides. Over time, these hydroxides undergo dehydration to form the metal oxide crystal structures [72].

This method is a good alternative to organic decomposition processes from the environment viewpoint. Moreover, hydrothermal synthesis does not need special water- and oxygen-free procedures and annealing step to crystalize the products.

Goh *et al.* [73] prepared $CoFe_2O_4$ by hydrothermal synthesis with sizes between 15.6 and 33.1 nm. The size of nanoparticles was controlled by the temperature of hydrothermal reaction. The saturation magnetization increase with particle size and the highest value achieved was 73.4 emu/g.

The advantages and drawbacks of each method discussed above are summarised in Table 3.3. The choice of the appropriate method to synthesize nanoparticles should be done as a function of the final application. In terms of simplicity and environmental friendly methodologies, co-precipitation and hydrothermal synthesis are the preferred routes because only need water-based solutions to prepare magnetic nanoparticles. The differences between these two methods are mainly the need of an annealing step in the case of co-precipitation. Thermal decomposition and micro-emulsion methods involve the use of organic compounds and the processes are more complex to settle than the co-precipitation and hydrothermal synthesis. When the shape control is a required aim, the best methods are thermal decomposition and hydrothermal synthesis. Additives or different precursor nature could easily control the shape of nanoparticles by favouring the growth in some crystallographic direction [63, 74, 75]. The shape could also be controlled on microemulsion synthesis however this method requires a large amount of solvent [76].

Table 3.3 Summary comparison of possible methods to synthesize $CoFe_2O_4$ nanoparticles.

Method	Synthesis	Annealing	Solvent	Size distribution/ Shape control	Yield	References
Co-Precipitation	Simple, ambient conditions	Needed	Water	Relatively narrow/ Not good	High	[59, 77]
Thermal decomposition	Complicated, inert atmosphere	Needed	Organic compound	Very narrow/ Very good	High	[61]
Micro-emulsion	Complicated, ambient conditions	Needed	Organic compound	Relatively narrow/ Good	Low	[68]
Hydrothermal synthesis	Simple, autogeneous pressure	Not needed	Water	Very narrow/ Very good	Medium	[73]

Co-precipitation and thermal decomposition are the best studied to prepare magnetic nanoparticles. Although, due to a high interest in use of simple and environmental friendly methods, hydrothermal synthesis has been extensively applied the last years. The following paragraphs are devoted to the review of the hydrothermal synthesis of $CoFe_2O_4$ nanoparticles.

Only a few papers could be found in *Web of Knowledge*® about hydrothermal synthesis of $CoFe_2O_4$ nanoparticles. The first work reported was in 2003 by Cote *et al.* [72] which prepared $CoFe_2O_4$ nanoparticles by continuous hydrothermal synthesis. Important conclusions were achieved. It was found that it is necessary to control pH and temperature in order to prevent premature precipitation of iron in the reactor. The presence of a second metal cation was beneficial in controlling the particle formation process probably by preventing the formation of complex hydroxides when the base was added to the cold metal salt solution. In this work two variations of the continuous hydrothermal synthesis were examined – cold mixing and hot mixing [72]. The cold mixing experiment produced a material with less impurities than the hot mixing one. Furthermore, a mechanism of particle formation was postulated involving the precipitation of metal hydroxides at ambient conditions, dissolution of the hydroxides as temperature was increased followed by rapid precipitation of metal oxides at elevated temperatures. When the reactants were mixed at elevated temperatures, the mechanism was simply precipitation of metal oxides due to the addition of the hot hydroxide solution. In both mechanisms, very fine particles of $CoFe_2O_4$ were produced.

In 2004, the effect of cetyltrimethylammonium bromide (CTAB) as surfactant in hydrothermal synthesis was studied by Ji *et al.* [78]. The products prepared without CTAB showed an irregular shape and wide size distribution. However, the morphology changed drastically when the surfactant was applied. Nanorods were formed with the average size of 120 nm in length and 25 nm in diameter (Figure 3.7A). CTAB is an ionic compound, which is ionized completely in water. The resultant CTA^+ has a positively charged tetrahedron with a long hydrophobic tail, while the growth unit for $CoFe_2O_4$ crystal is considered to be $Co–Fe–OH^-$. Therefore, ion pairs between CTA^+ and $Co–Fe–OH^-$ could be formed due to electrostatic interaction. In the crystallization process, surfactant molecules may serve as a growth controller, as well as an agglomeration inhibitor, by forming a covering film on the newly formed $CoFe_2O_4$ crystal. The adsorption of species at the crystal surfaces strongly affects the growth rate and orientation of the crystals. The surfactant molecules in the film tend to be perpendicular

to the absorbed surface, and the growth units would tend to face-land onto the growing interface. Since this kind of landing and dehydration will result in Co–O–Fe bonds, make this landing mode is predominant in competition with other ones such as vertex- and edge-landing. $CoFe_2O_4$ crystal should grow preferentially and the dehydration steps are repeated in the following procedures. In terms of magnetic properties, nanorods showed a very low saturation magnetization (0.083 emu/g). The reason for this low magnetization was not discussed. More works in hydrothermal synthesis assisted by different surfactants, in order to change the morphology, were reported [74, 75, 79, 80].

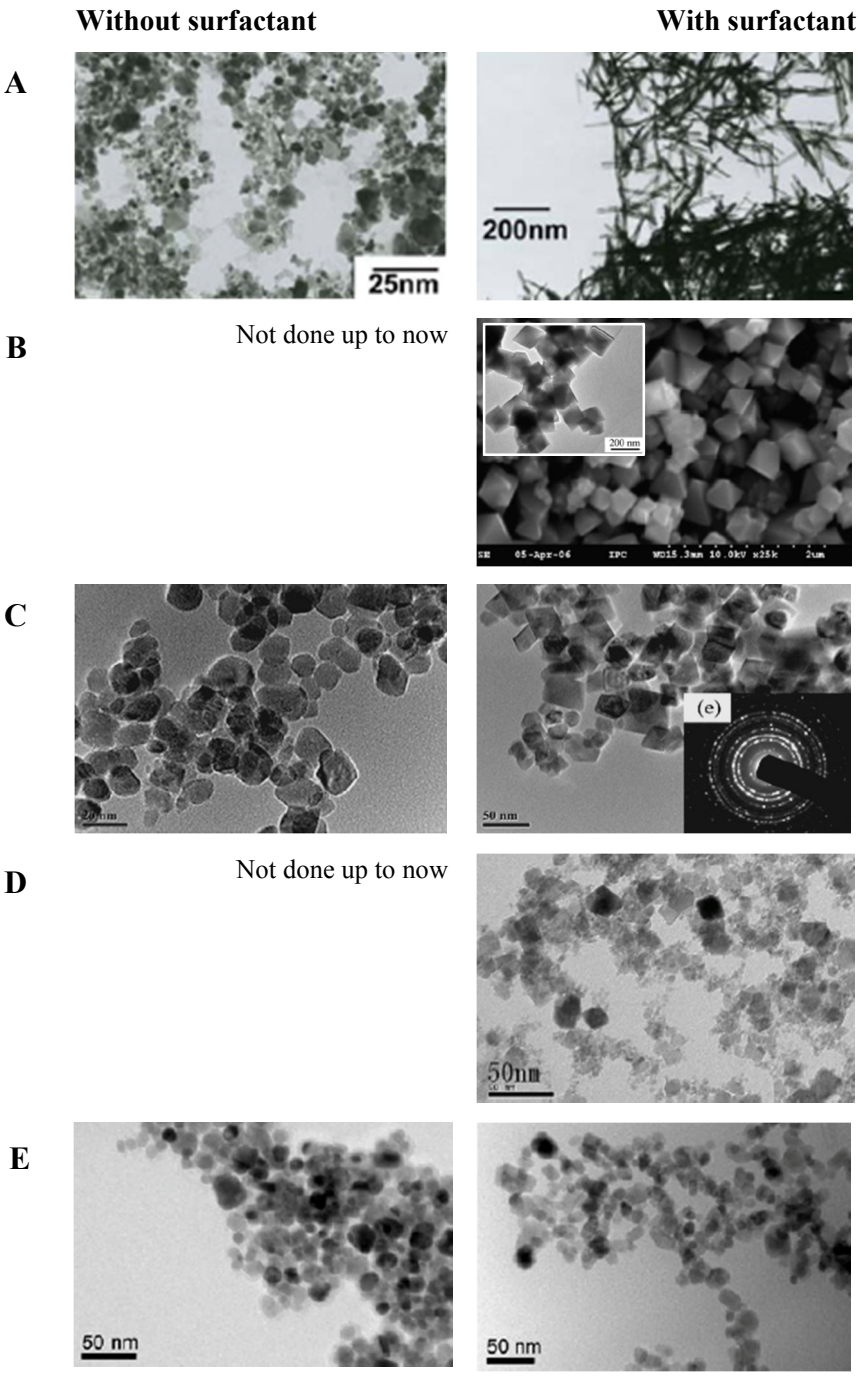

Figure 3.7 Different morphologies of $CoFe_2O_4$ nanoparticles prepared by surfactant-assisted hydrothermal synthesis. **A**= Ref. [78], **B**= Ref. [74], **C**= Ref. [79], **D**= Ref. [75] and **E**= Ref. [80].

Chen *et al.* [79] synthesized $CoFe_2O_4$ nanoparticles by using polyethylene glycol (PEG) as surfactant. The shape of particles changed from quasi-spherical to parallelogram, Figure 3.7C. The addition of PEG improved the crystallite size from 24 to 35 nm. In terms of magnetic properties, the saturation magnetization increased from 29.3 to 36.5 emu/g with PEG addition. Similarly to the work reported by Chen *et al.*, Zhang *et al.* [80] studied the effect of different amounts of trisodium citrate (CA) dihydrate

($Na_3CA{\cdot}2H_2O$), Figure 3.7E. The authors observed that the lattice constant, crystallite size, shape and magnetic properties could be tuned by changing the masses of $Na_3CA{\cdot}2H_2O$. The lattice constant increased with $Na_3CA{\cdot}2H_2O$ mass increase. However, the average size of particles increased for masses of surfactant below 1g and decreased for larger amounts of surfactant. When a large amount of additive was used, the Co^{2+} and Fe^{3+} had finite masses and reacted totally; the extra molecules of additive had no contribution to the increase of lattice constant. The magnetic properties of the products are related with lattice constant, size and shape of particles due to the addition of $Na_3CA{\cdot}2H_2O$.

In addition to the surfactant effect on hydrothermal synthesis, other studies were carried out in order to understand the mechanism of the method. Goh *et al.* [73] studied the hydrothermal synthesis temperature effect on particle size and shape. It was observed that the shape of $CoFe_2O_4$ nanocrystals was transformed from spherical into rod and the crystallite size increased by increasing the hydrothermal temperature, Table 3.4. The larger sizes result from coalescence and Ostwald ripening at high temperatures.

Table 3.4 Effect of hydrothermal temperature on average crystallite size and magnetic properties, of $CoFe_2O_4$ adapted from Ref. [73].

Hydrothermal temperature (°C)	**Average crystallite size (nm)**	**Saturation magnetization (emu/g)**
150	18.45	61.1
200	22.62	74.8
250	25.29	73.6
300	26.79	73.2

Zhao *et al.* [58] studied the effect of pH of solution and the coexisting cations. It was found that pure $CoFe_2O_4$ could be synthesized at pH 12 and above. To evaluate the effect of coexisting cations, the authors used LiOH, NaOH and KOH solutions. It was observed that the final products did not contain Na or K, which indicates that these cations did not take part in the reaction. In the presence of NaOH and KOH aqueous solutions the only product was $CoFe_2O_4$. However, the product synthesized in LiOH solution did not match with $CoFe_2O_4$. The researchers suggested that Li could form a spinel compound with formula $Li_{2x}Co_{1-x}Fe_2O_4$.

Li *et al.* [81] carried out the magnetic measurements at different temperatures: 10 and 300 K. CFO nanoparticles exhibited high coercive field at 10K and performed superparamagnetism at room temperature (characterized by very low coercive field), Figure 3.8.

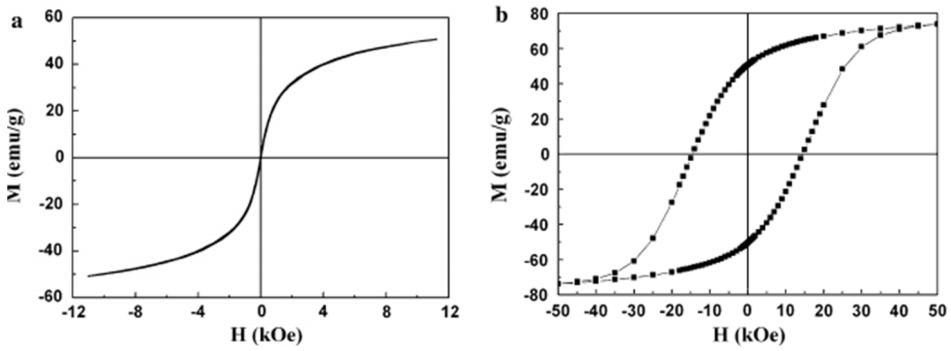

Figure 3.8 Magnetic measurements carried out at room temperature (**a**) and 10 K (**b**), adapted from Ref. [81].

From this hydrothermal synthesis review, it was conclude that the final product properties (size, shape and magnetic properties) could be easily controlled by this method.

3.4. Functionalization - Electrophoretic deposition

Electrophoretic deposition (EPD) has attracted special attention of the scientific community over the last decade due to its high versatility for application for the preparation of thick or thin films of different materials, substrates and combinations of materials, its cost-effectiveness and the use of simple equipment [82-85]. It offers easy control of thickness and morphology of the deposited product by controlling the processing parameters like voltage and time [85-89]. For all the stated reasons, it is a good candidate for the functionalization of the porous thin films matrices with cobalt ferrite nanoparticles.

3.4.1. Introduction

The electrophoresis phenomenon was discovered in 1808 by a Russian physicist F. F. Ruess, who observed movement of clay particles, suspended in water, due to an induced electric field [90]. The basic phenomenon involved in EPD for the fabrication of

ceramics was first researched by Hamaker in 1940 [91]. On the following years and up to the early 90's, EPD was mainly researched for the processing of traditional ceramics or coatings of metal components and very limited work was carried out on the EPD of materials engineering [84]. More recently, it the last two decades the interest in electrophoretic deposition increased incredibly, and new applications of advanced materials have been discovered, denoted by the existence of more than a thousand articles, patents and four conferences about EPD.

Nowadays, EPD has been studied for several of novel applications like anti-oxidant ceramic coatings, micro moulds, fabrication of functional films for advanced microelectronic devices, monolayers of nanoparticles or bioactive coatings for medical implants [82, 83, 86-89, 92-95].

3.4.2. Basic concepts

Electrophoretic deposition is a colloidal process, which is used for coatings and fabrication of films. During the EPD process, charged powder particles, dispersed or suspended in a liquid medium are attracted and deposited onto a conductive substrate of opposite charge on application of a DC electric field, Figure 3.9. Therefore, are three basic steps in EPD: (1) formation of a stable suspension of the particles, (2) electrophoretic migration of the particles to the deposition electrode, and (3) deposition of the particles in the desired arrangement on the electrode surface [82].

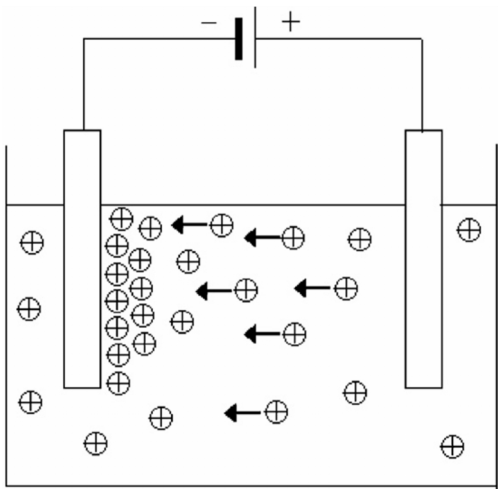

Figure 3.9 Two electrodes cell for electrophoretic deposition showing positively charged particles in suspension migrating towards the negative electrode [84].

There are two types of electrophoretic deposition depending on which electrode the deposition occurs. When the particles are positively charged, the deposition happens on the cathode - cathodic electrophoretic deposition [96]. If the particles are negatively charged, the deposition occurs on the anode and the process is called anodic electrophoretic deposition, Figure 3.10.

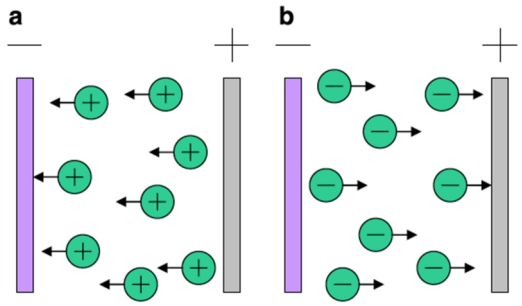

Figure 3.10 Schematic illustration of EPD process a) cathodic EPD and b) anodic EPD [90].

During the EPD process, particles get charged and move towards the electrode, depositing on the electrode. But, how do particles get charge? Four mechanisms of charging the particles were suggested [97]:

1. A selective adsorption of ions from the liquid onto the solid particle;
2. Dissociation of ions from the solid phase into the liquid;
3. Adsorption or orientation of dipolar molecules at the particles surface;
4. Electron transfer between the solid and liquid phase due to different work function.

In case of ceramic particles the last mechanism is not applicable but the first two invariably occur. The sign of the net charge on the particle will depend not only on whether mechanism 1 or 2 is dominant. Also, a positively charged particle may even behave like a negative one, which is attracted to a positive electrode, if an excess of negative ions is attracted to the vicinity of the particles. So it's difficult to predict whether a deposition will occur, if on positive or negative electrodes in an unknown system.

The electrical double layer is a very important concept for the surface chemistry of materials in colloidal science field, like as in EPD. It describes the variation of the electric potential near a surface, and has a large effect on the behavior of colloids. Development of a net charge at the particle surface affects the distribution of ions in the surrounding

interfacial region, resulting in an increased concentration of the counter ions close to the surface. Apart from the surface charge of the particles, the electrical surrounding double layer consists of two parts: an inner region called *Stern layer*, where the ions are strongly attracted to the particle surface and closely attached to it due to their electrostatic force and an outer region called *Diffuse layer*, where the ions are less firmly associated to the surface and which contains free ions with a higher concentration of the counter ions, Figure 3.11. In the *Diffuse layer* is a boundary known as the slipping plane, in which the particle acts as a single entity [90, 98].

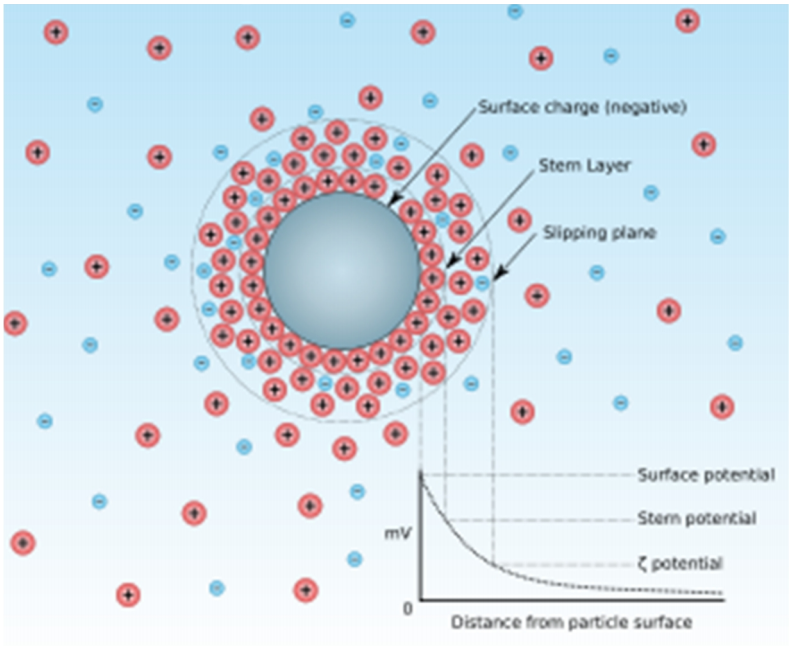

Figure 3.11 Schematic representation of the double layer surrounding a charged particle and evolution of the zeta potential from the surface potential [98].

The zeta potential is the potential difference between the stationary layer of each dispersed particle and liquid medium. It can be used to control the stability of the colloidal suspensions by determining the intensity of repulsive interactions between the particles. Higher values of zeta potential lead to more stable suspensions. Increasing the ionic strength can significantly reduce the repulsive forces. The behaviour of particle separations depends critically on the ionic strength. If the potential energy is high, it originates strong repulsive forces producing a totally dispersed system [90].

Furthermore, the zeta potential determines the direction and migration velocity of particles during EPD, according to the negative or positive signal of the charge.

3.4.3. Mechanism of EPD process

Although EPD has been studied over the last decades, the mechanism of the deposition is not entirely clear. Different theories have been discussed for a possible mechanism.

The first attempt to explain the phenomenon of EPD was made in 1940 by Hamaker *et al.* [99], who suggested that the EPD is mainly a mechanical problem, *i.e.*, the formation of deposits by EPD is similar to the formation of sediment due to gravitation. The authors noted that the role of the electric field is only to provide a force, which presses the particles and moves them towards the electrode.

Grillon *et al.* [100] suggested that the charged particles would be neutralized upon contact with the deposition electrode, becoming static to form a deposit and that the role of the electric field is only to push the charged particles to move towards the electrode. Due to a "tip effect", the first deposited particles, i.e. those in contact with the substrate, play the role of poles attracting the other particles, Figure 3.12.

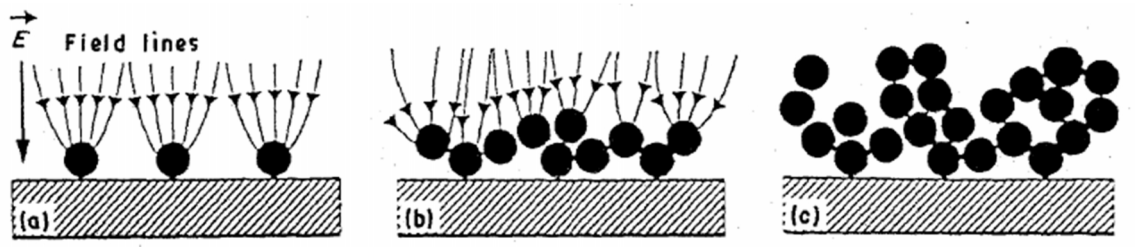

Figure 3.12 Phenomenological model of the electrophoresis of coarse particles [100].

Another mechanism found in literature was the electrical double layer distortion and thinning mechanism proposed by Sarkar and Nicholson [101]. The authors proposed a model mainly based on distortion of double layer. When a positive charge particle and its shell are moving towards the cathode, the double layer is distorted becoming thinner ahead and wide behind due to the electric field applied, Figure 3.13(a). The cations in the liquid also move to the cathode along with positively charged particles and the counter ions behind of the double layer will tend to react with the cations in high concentration around them, Figure 3.13(b). This chemical reaction reduces the thickness of the double layer and therefore decreases the zeta potential. When another particle with a thin double layer is approaching, the two particles come close enough to interact through London Van der Walls attractive forces and coagulate, Figure 3.13(c).

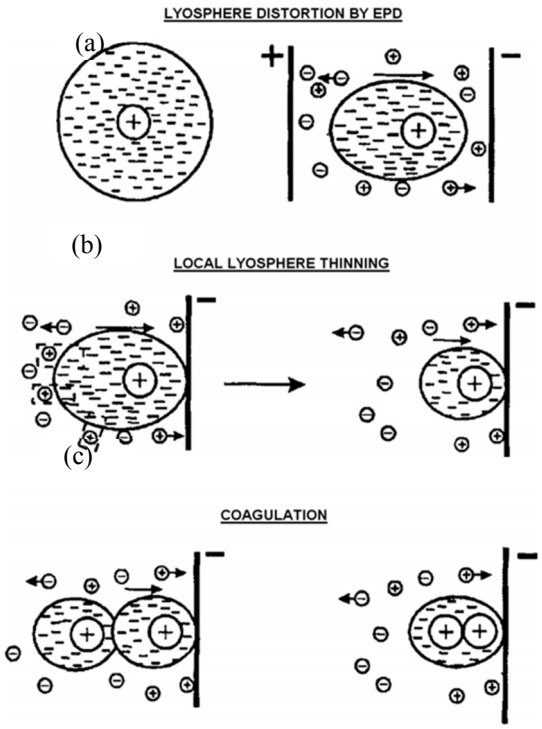

Figure 3.13 Schematic representation of the deposition mechanism due to electrical double layer distortion and thinning [101].

3.4.4. Kinetics of electrophoretic deposition

In order to control and manipulate electrophoretic deposition process according to desired final product, the understanding of the kinetics of electrophoretic deposition is highly important.

Hamaker [91] observed a linear dependence of the deposited weight or yield of the EPD with the amount of charge passed, and proposed that the amount deposited is proportional to the concentration of the suspension, time of deposition, surface area of electrode and electric field showed in the following equation:

$$M = \int_0^t \alpha A C \mu E \, dt \qquad \text{Eq. 3.1}$$

where M stands for the deposited mass in time t(s), α designates a coefficient which represents the fraction of particles deposited near the electrode, A represents the electrode area (m^2), C is the particle concentration in the suspension (kg/m^3), μ is the electrophoretic mobility ($m^2/V.s$) and E is the electric field (V/m).

3.4.5. Parameters related with suspension

Concerning the suspension properties to obtain a good deposit by electrophoretic deposition, many key parameters must be considered, such as the physicochemical nature of both suspended particle and the liquid medium: particle size, dielectric constant of liquid, zeta potential and stability of suspension [102]. The effect of each parameter will be discussed in the following subtopics.

- **Particle size**

Nowadays, electrophoretic deposition is used from micron to nanoscale. For larger particles, the main problem is that they tend to settle due to gravity forces. In this case, the mobility of particles needs to be higher than the gravity force. It is difficult to get a uniform deposition with a sedimenting suspension of large particles because, will lead to gradient in deposition, *i.e.*, thinner above and thicker deposit at the bottom in case of deposition electrode is placed vertically. However, nanoparticles also show some drawbacks due to their high tendency to agglomerate. The use of solvents and in some cases additives is necessary to prevent the agglomeration of nanoparticles.

- **Dielectric constant of liquid**

The behaviour of the dielectric constant of the suspension media was studied by Powers et al. [103]. The authors used different suspension media of β-Al_2O_3 and found that the deposition did not take place for solvents with dielectric constant below 12 and above 25. For low dielectric constant, the deposition fails due to insufficient dissociative power of solvent. In case of high dielectric constant the high ionic concentration in the suspension reduces the thickness of the double layer and consequently the electrophoretic mobility.

- **Zeta potential and stability of suspension**

As mentioned before, the zeta potential is a key factor in the electrophoretic process. It determines the intensity of repulsive interaction between particles, the direction (positive or negative) and migration velocity of particle during EPD. A high zeta potential will confer stability to the suspension and the dispersion will resist to agglomeration.

3.4.6. Parameters related to electrophoretic deposition process

Not only the suspension properties lead to a good electrophoretic deposition but also the parameters such as deposition time and applied voltage are very important.

- **Deposition time**

The effect of deposition time was studied by A. Wu and P. Vilarinho [89]. The authors observed that the deposition rate decreases for long times of deposition due to an overall electrical resistance of the film already deposited. So, short times of deposition favour thick films, while long time deposition leads to decrease the rate due to the formation of an insulating layer on the electrode composed by the film itself.

- **Applied voltage**

Besides the studies on the effect of time deposition, A. Wu and P. Vilarinho also studied the effect of applied voltage [89]. For a fixed time of 2.5 minutes, the thickness of deposit increases linearly with the applied field. Both results at the time are in agreement with the Eq. 3.1 discussed in Kinetics of EPD – Section 3.4.4.

Experimental Procedure

4. Experimental procedure

The experimental procedure of this thesis is divided in 3 parts: i) preparation of porous ferroelectric thin films: ii) preparation of ferromagnetic nanoparticles and iii) functionalization of pores of the ferroelectric matrix with ferromagnetic nanoparticles by electrophoretic deposition, Figure 4.1.

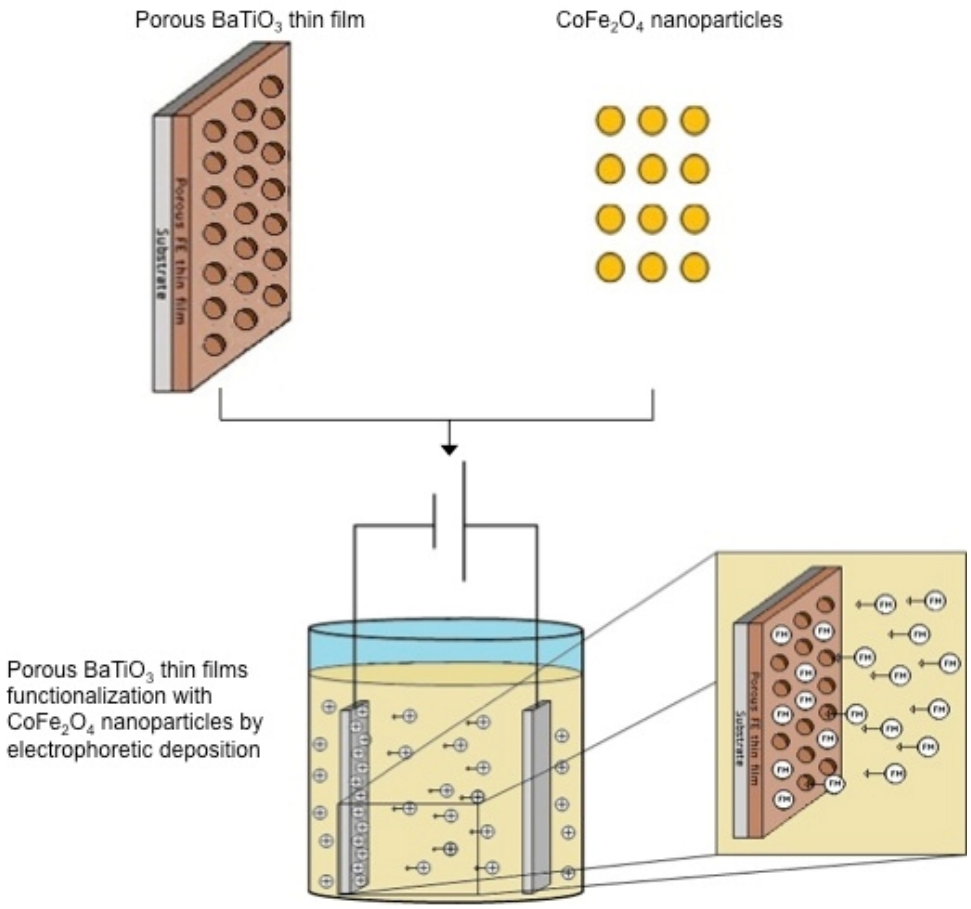

Figure 4.1 Schematic of this work illustrating the functionalization of porous $BaTiO_3$ matrix with $CoFe_2O_4$ nanoparticles by electrophoretic deposition.

4.1. Porous ferroelectric films

To produce porous ferroelectric thin films the experimental procedure proposed by Ferreira *et al.* [13] was adopted. It consists in the preparation of $BaTiO_3$ sol-gel solution and then its deposition in conductive substrates by dip-coating combined with EISA (Evaporation Induced Self Assembly).

In order to form the pores in the films, template molecules are needed. Typical templates are surfactant molecules or amphiphilic block copolymers (ABCs), which consist of a copolymer formed by blocks of polymers chemically different that are covalently attached to each other. These polymers should be have different hydrophobic character namely one should be very hydrophobic while the other should be hydrophilic. They are mostly referred by the abbreviation of their segments and usually a *b* is put between them to indicate the block structure. For example, in this work, it is used PS-b-PEO for polystyrene-poly-(ethylene oxide), Figure 4.2.

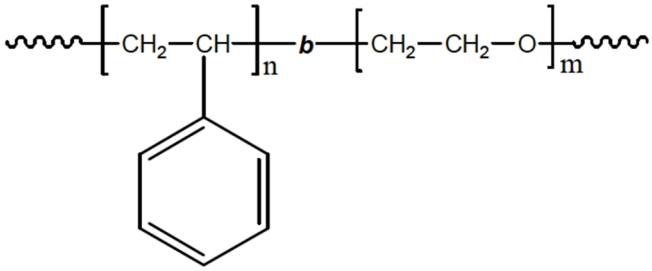

Figure 4.2 Structure of monomer of PS-b-PEO block copolymer, adapted from Ref. [104].

By dissolving the ABC in a liquid that is thermodynamically a good solvent for one of the blocks and a precipitant for the other (called a "selective solvent"), micelles are formed above the critical micelle concentration (CMC). The inorganic precursors typical condense around those micelles arrays to form the porous films. In this work the PS is soluble in tetrahydrofuran (THF), while the PEO is solubilized by the ethanol.

In this work, it was used as block co-polymer polystyrene-poly-(ethylene oxide) with two different average molecular weight (Mw): a) PS-b-PEO 40000-53000 g mol^{-1} and b) 58600-71000 g mol^{-1}.

4.1.1. Sol-gel method

For preparation of sol-gel solution, three initial solutions were prepared: A, B and C. Table 4.1 shows the chemical composition of these starting solutions used to synthesize $BaTiO_3$ porous films.

Table 4.1 Chemical composition of initial solutions used for preparation of $BaTiO_3$ films.

	Reagents	Weight (g)	Producer	Purity
Solution A	Ps-b-PEO	*	Polymer source	-
	$(CH_2)_4O$	0.930	Sigma-Aldrich	≥99.5%
	CH_3CH_2OH	2.280	Panreac	Absolute
Solution B	$Ba(OH)_2 \cdot 8H_2O$	0.268	Merk	-
	CH_3COOH	1.717	Sigma-Aldrich	≥99.7%
Solution C	$C_5H_8O_2$	0.100	Fluka	99.3%
	$Ti(OBu)_4$	0.480	Merk	-
	CH_3CH_2OH	0.500	Panreac	Absolute

* The used polymer weight depends of concentration. Low and high concentrations correspond to 0.083 g and 0.166 g, respectively.

In order to study the effect of molecular weight (Mw) of PS-b-PEO, two different Mw were used: Mw = 40000-53000 g mol^{-1} and Mw=58600-71000 g mol^{-1}. The molecular weight is related with the number of monomers of polystyrene and polyethylene oxide (*n* and *m* index, respectively, displayed in Figure 4.2) present in a unique chain of polymer.

The solution containing the block polymer was heated to 70ºC for 10 minutes to allow the complete dissolution of polymer in tetrahydrofuran (THF). Then, 2.28g of ethanol were added drop-by-drop under magnetic stirring at 25 ºC. The solution B, the barium precursor was dissolved in acetic acid and heated to 70 ºC for 60 minutes to allow the total dissolution of $Ba(OH)_2 \cdot 8H_2O$. In third solution, acetylacetone was added to titanium precursor and stirred for 45 minutes at room temperature and then ethanol was added drop-by-drop. To achieve the final sol-gel solution, solutions A, B and C were mixed, at room temperature, in the following sequence: first solution C was added into solution B drop-by-drop under stirring. After 15 minutes, the new solution (B+C) was dropped into solution A. The sol-gel solution was kept under stirring several minutes before dip-coating process.

4.1.2. Dip-coating and EISA

The films were deposited by dip-coating (Figure 4.3) with different values of withdrawal rate (15.58, 29.58 and 96 mm/min) onto 10 × 25 mm sized slides of multilayer ($Pt/TiO_2/SiO_2/Si$) wafers from *Ramtron*. Before deposition the substrates were cleaned by ultrasonics agitation in ethanol and acetone, 5 minutes each one.

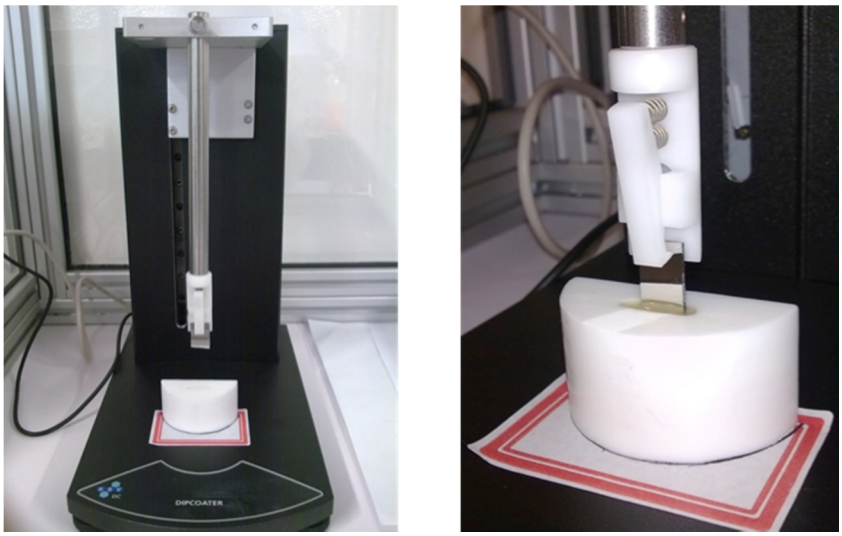

Figure 4.3 Deposition of porous $BaTiO_3$ film by dip-coating.

The solutions preparation and deposition was done at approximately 30% of relative humidity and 25 °C. The dip-coater used is from *KSV* model *DC/D/LM*. After deposition, $BaTiO_3$ films were treated in air up to 400 °C for 5 minutes in order to complete de inorganic condensation of the matrix and to decompose the organic parts of the precursors and copolymer template. Then, the films were annealed for 6 minutes at the desired temperatures of crystallization. Above 700 °C the calcination time was 2 minutes in order to avoid the elimination of the porous by the high growth of $BaTiO_3$ grains. The annealing temperatures were chosen according to the results from Differential Thermal (DTA) and Thermogravimetry (TGA) analyses.

Due to the porosity and in order to avoid humidity and gases adsorption, the films were involved in filter paper, placed in Schlenk and maintained under nitrogen atmosphere until further characterization or functionalization, Figure 4.4.

Figure 4.4 Schlenk with porous $BaTiO_3$ thin films inside.

4.2. Cobalt ferrite nanoparticles – Hydrothermal synthesis

The $CoFe_2O_4$ nanoparticles were synthesized by hydrothermal synthesis, a water-based environmental-friendly process. In typical synthesis, 0.1 mol of Co^{2+} : 0.2 mol of Fe^{3+} : 0.01 mol of NaOH : 0.55 mol of H_2O. The starting precursors, $Co(NO_3)_2{\cdot}6H_2O$ (Sigma-Aldrich, purity 98%) and $Fe(NO_3)_3{\cdot}9H_2O$ (Sigma-Aldrich, purity ≥ 98%) with Co:Fe ratio=1:2 were dissolved, under magnetic stirring, into distilled water to achieve mixed aqueous solutions. The pH in this step was between 1 and 2 (the equipment used for pH measurements was *WTW* model *pH330i*). In some cases, to study the effect of the additive in final properties of $CoFe_2O_4$, different concentrations of PVP (Aldrich, Mw = 1300000 $gmol^{-1}$) were added to the reaction mixture. Two aqueous solutions of PVP were prepared with the concentration of 5% (%w/v) and 10% (%w/v). In this case, 2 mL of these mother solutions were added by substitution of the same volume of H_2O – corresponding to PVP5 (solution of 5% of PVP) and PVP10 (solution of 10% of PVP). After 15 minutes the precipitating agent, NaOH (eka), was added drop-by-drop under stirring and a dark brown solution was achieved with at pH=13. Different concentrations of NaOH were used in order to study the effect on the morphology of the nanoparticles. The solution was kept under stirring for one hour. Then, it was transferred to a Teflon-lined stainless steel autoclave, Figure 4.5A.

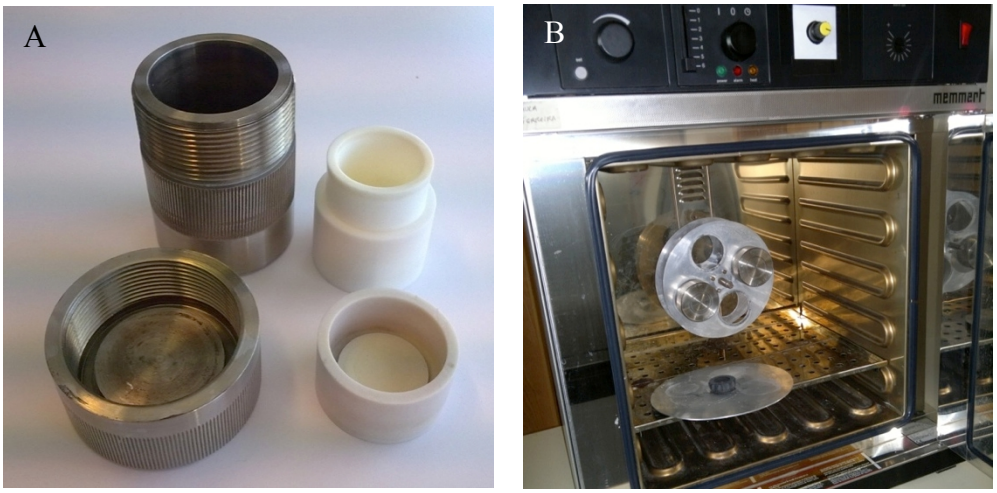

Figure 4.5 (A) 30mL autoclave used for hydrothermal synthesis and (B) oven equipped with mechanical stirrer.

The autoclave was placed into an oven equipped with rotation system Figure 4.5B. The rotation speed was the same for all syntheses, 35 RPM. Different temperatures and times of hydrothermal synthesis were used to study and optimize the process. According to the aim of this thesis, deposition of nanoparticles in the pores of $BaTiO_3$ films, the control of size and shape of $CoFe_2O_4$ nanoparticles is required. Initially the effect of the synthesis temperature were studied. Then, the best temperature was used to study the time effect. In the end the additive effect, NaOH and metal ions concentrations were studied. After hydrothermal synthesis, the dark powders were collected from the bottom of Teflon vessel and were washed by ultracentrifugation with distilled water and ethanol. The ultracentrifugation equipment used was *Beckman* model *L8-70M.* Initially the powder was washed under 10.000 RPM but at this velocity the nanoparticles tend to agglomerate due to high centrifugal forces. In order to avoid this problem, a study was developed to achieve the best velocity to minimize the nanoparticles agglomeration. The ideal velocity was 7.500 RPM. The drying step was made at room temperature. The final powders were stored in glass vials.

4.3. Films functionalization – Electrophoretic deposition

The functionalization step involved firstly optimization of electrophoretic deposition, namely in terms of solvent to ensure monodispersion of nanoparticles.

Five suspensions were prepared in a glass beaker with 0.2 mg mL^{-1} of $CoFe_2O_4$ nanoparticles. Distilled water, ethanol (Panreac, purity P.A.), acetone (Carlo Erba, purity P.A.), n-hexane (Sigma-Aldrich, purity ≥ 99%) and n-butanol (Sigma, purity > 99%) were tested. A further dispersion of the suspension was conducted by using ultrasonics agitation in equipment *Bransonic* (70 W and 42 kHz) for 1 hour and then 15 seconds in ultrasonic sonar from *Bandelin* model *Sonoplus HD 3100*. The stability of the suspensions was studied by two simple methods: by observation of the suspension colour over the time and by UV spectroscopy.

For the EPD optimization, bare substrates of 10 × 25 mm were used (the same as used for dip-coating of porous $BaTiO_3$ thin films. In this step, studies on effect of applied voltage and deposition time were carried out.

Finished the EPD optimization, the best parameters were chosen to functionalize porous $BaTiO_3$ thin films, Figure 4.6.

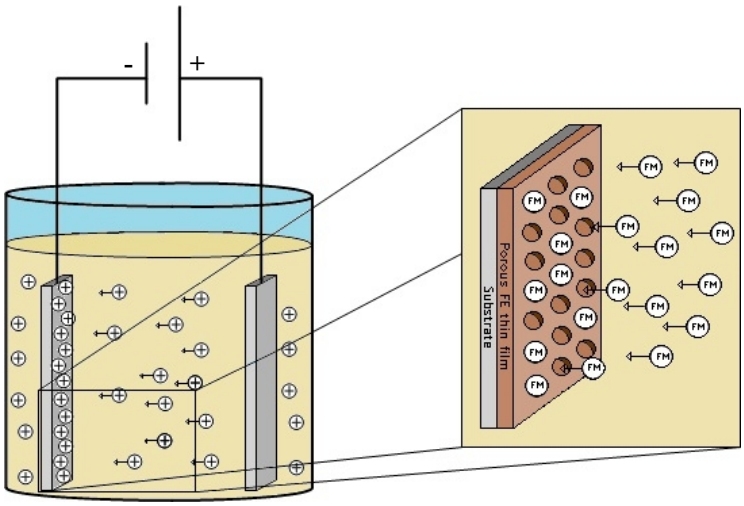

Figure 4.6 Schema of functionalization of porous thin films with ferromagnetic nanoparticles by EPD.

4.4. Characterization

4.4.1 X-rays diffraction (XRD)

X-ray diffraction was a very useful technique in this work, enabling a qualitative analysis of the crystalline phases in the porous $BaTiO_3$ thin films, $CoFe_2O_4$ nanoparticles and composite films. This technique is a versatile and non-destructive.

By exposing a crystalline sample to a X-ray beam, some of those X-rays are diffracted according to a certain angle (2θ) matching characteristic crystallographic directions of the material as given by the "Bragg's law" [105]:

$$\lambda = 2d \sin\theta \qquad \text{Eq. 4.1}$$

where λ is the wavelength of X-rays, θ is the angle between the incident rays and crystal surface, d is the spacing between layer of atoms.

In the present project, the X-rays diffractions were performed using *Philips X-Pert MPD* equipment with Cu-Kα X-radiation and λ = 1.5406 Å. The sweeping angles used for identification of the crystalline phases present in $BaTiO_3$ thin films were from 20 to 60°2θ and for $CoFe_2O_4$ nanoparticles were 20 to 80°2θ, both with a step of 0.02°2θ at room temperature. For phase identification through the X-ray diffraction peaks, an integrated database of *Powder Diffraction Files* (PDF4+) from the *International Centre of Data Diffraction* (ICDD) was used.

Through the broadening of the X-ray diffraction peaks, crystallite sizes of less than ~0,1 μm could be conveniently measured [106]. The crystallite size of $CoFe_2O_4$ was calculated by Scherrer equation:

$$\beta = \frac{K\lambda}{L\cos\theta} \qquad \text{Eq. 4.2}$$

where β is the breadth usually expressed as the full width at half maximum peak (FWHM), K is a constant to account for particle shapes (close to unity, usually 0.9 for spherical shapes), λ is the wavelength of the X-rays, L is the crystallite size and θ is the diffraction angle. The broadening is also affected by instrumental factors. Such factors

have to be subtracted to correctly calculate the crystallite size. To measure the instrumental broadening a crystalline material in which the broadening is negligible can be used. In this case, the instrumental broadening was determined with a crystalline lanthanum hexaboride (LaB_6). The peaks used for crystallite size measurements were at 2θ=30.07 and 35.42°. In these cases, new X-rays diffractions were measured between 28 and 38° 2θ in order to obtain more defined peaks allowing a good crystallite size measurements.

4.4.2 Scanning Electron Microscopy (SEM)

Scanning Electron Microscopy was used in this project to reveal the microstructure of porous $BaTiO_3$ thin films and composite thin films. An electron gun generates a beam of electrons inside a vacuum column, which is then focused and driven to collide with a target, the sample. [107] An image is possible due to the electronic signal generated by the low angle backscattered electrons, which are created by electron interactions with the material surface [108].

The SEM equipment used was *Hitachi*® model *SU-70.* This microscopy has magnifications from ×30 to ×800.000 and acceleration voltage in range of 0.1 to 30 kV. The sample holder has 5-axis motorized: displacement in X and Z-axis, shift in Y, rotation (360°) and tilt (-5 to 70°). The tilt is an important characteristic because it allows the tilt movement in cross-section of *Ramtron* substrate and of porous $BaTiO_3$ thin films allowing a good view and measurement of thickness of the films. The potential acceleration used was 7kV. This equipment is also equipped with microanalysis system for energy dispersive spectrometry of X-rays/EDS from *Bruker* model *Quantax 400*.

For samples preparation, the porous $BaTiO_3$ thin films and composite thin films were glued in typical SEM sample-holder with carbon tape. This preparation method allows the reutilization of the films for other characterization techniques or future functionalization.

4.4.3 Transmission Electron Microscopy (TEM)

Transmission Electron Microscopy (TEM) has the same operation principle of SEM, but in this case the electrons are accelerated at a much higher potential to pass through the sample towards the detector below it. The electrons, passing through the

sample, which has to be very thin to allow it, are either absorbed or dispersed changing their directions. This dispersion is influenced by the atomic arrangement of the material. Afterwards, they are focused again, amplified and projected in a fluorescent screen or in a monitor. This technique allows observing the $CoFe_2O_4$ shape and size. The average size of nanoparticles was determined by measuring 150 particles of each sample assisted by software *ImageJ* version 1.46r. The size distributions were determined by Gaussian curve.

TEM was done in *Hitachi*® model *H9000* with an acceleration potential of 300 kV. The $CoFe_2O_4$ nanopowders were suspended in n-hexane (Sigma-Aldrich, purity ≥ 99%). The powder was added slowly into n-hexane under ultrasonics agitation and kept for 1 hour. Then, a droplet of the suspension was deposited in a holey carbon micrometric copper grid from *Agar Scientific*®.

4.4.4 Differential Thermal and Thermogravimetric Analysis (DTA/TGA)

Differential Thermal Analysis (DTA) is a technique that permits to know the thermal behaviour of a material and the transformations it goes through as temperature increases. It is done by heating up the material, registering its temperature difference between material and an inert one (standard sample, normally pure alumina), which is being heated simultaneously. The temperature difference (in μV) is then plotted against the temperature of the furnace. Positive differences between them indicate exothermal transformations, while negative ones denote endothermic phenomena.

It is usual to record the weight variation with temperature during DTA, with a technique called thermogravimetric analysis (TGA). This provides additional information about the transformation that is occurring, by overlapping the weight loss curve (TGA) as a function of temperature together with the thermal energy curve (DTA).

These techniques were used to evaluate the $BaTiO_3$. The sol-gel solution was dried at 60°C for 48h and then milled in a mortar . The equipment used was *Setaram* model *Labsys™ TG-DSC16*. The analyses were done by heating the powder from room temperature to 800°C at rate of 10°C/min under flowing air.

4.4.5 Specific Surface Area (A_{BET}) and Porosity Measurements obtained from the 77 K N_2 Isotherms

Adsorption measurement based on the Brunauer-Emmet-Teller (BET) isotherm is the most widely used for the determination of the specific surface area of a powder or porous materials [109].

This measurement is done using N_2 adsorption at 77 K, by putting a solid material of a known mass in contact with a known volume of gas, it adsorbs creating a decrease in the pressure, from which the amount of adsorbed gas can be calculated. From these measurements a plot of the amount of gas adsorbed versus the relative pressure (P/P_0, P_0 being the saturation vapour pressure of the adsorption gas used) is represented, which is called the adsorption isotherm. According to IUPAC 1985, the shapes of adsorption isotherms are classified into six groups. Type I isotherm is given by a microporous solid having a relatively small external surface. In contrast, type II isotherm represents unrestricted mono/multilayer adsorption on a non-porous or macroporous adsorbent. Type IV isotherm shows a characteristic hysteresis loop and the limiting uptake at high P/P_0: these features are associated with capillary condensation taking place in mesopores. Type VI represents stepwise multilayer adsorption on a uniform non-porous surface. Type III and V are associated with weak adsorbent - adsorbate interactions. The BET equation that can be applied to the isotherm curve, which is only valid for lower values of *p/p0* and is used in this form [110]:

$$\frac{p}{V(p_0-p)} = \frac{1}{V_n C} + \frac{C-1}{V_n C}\frac{p}{p_0} \qquad \text{Eq. 4.3}$$

where V is the volume of gas adsorbed, V_m is the monolayer volume and C is a constant. By this procedure, the V_m can be calculated (from the slope and the intercept) and applied in Eq. 4.4 to calculate the surface area [110]:

$$A_{BET} = \frac{N_A \sigma V_m}{V_0} \qquad \text{Eq. 4.4}$$

where A_{BET} is the surface area, N_A is the Avogadro number, σ is the area of an adsorbed gas molecule and V_0 is the volume of 1 mol of gas at STP (Standard Temperature and Pressure).

The equipment used was *Micromeritics®* - *Gemini 2370 V5*. N_2 gas was used as the adsorption gas and liquid N_2 to cool down the samples. The samples were degassed at 200˚C overnight. These measurements allowed the determination of specific surface area of $CoFe_2O_4$ nanoparticles.

4.4.6 Piezoresponse Force Microscopy (PFM)

Scanning Probe Microscopy (SPM) has been a fundamental tool in high resolution characterization of metals, semiconductors, dielectrics, polymers and biomolecules. Piezoresponse Force Microscopy (PFM), the most popular technique of ferroelectrics characterization via SPM, allows a nondestructive visualization of domain structures in thin films at the nanoscale [111].

PFM technique is based on the detection of local piezoelectric deformation of the ferroelectric film, which is induced by the application of an external AC voltage ($V=V_0.\cos\omega t$, where V_0 is the vibration amplitude and ω the frequency) via a conducting cantilever tip. A standard lock-in technique is used by measuring the vertical mechanical displacement of the cantilever tip, as seen in Figure 4.7, which could be expressed as $\Delta Z=d_v V_0 \cos(\omega t+\varphi)$, where d_v is the effective piezoelectric constant and φ the phase difference between the applied voltage V and the piezoresponse, therefore indicator of the polarization direction.

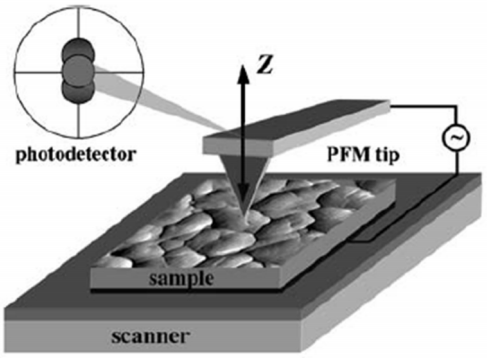

Figure 4.7 Schematic illustration of vertical PFM signal detection, adapted from Ref. [111].

However, apparent electrostatic components result in high complexity of piezoresponse detection in thin films. In addition, the presence of porosity (necessary for the subsequent functionalization) in combination with the low thickness (<200 nm) is responsible for making very difficult the process of characterization. The main reasons for the absence of publications in literature concerning the porous thin film piezoresponse characterization (with the exception of P. Ferreira et al. 2012 [13]) are: low quantity of deposited matter, inhomogeneity and preferential orientation of organized domains provoked by the substrate compliance interactions and unidirectional contraction of the domains due to the required thermal treatment [46].

Piezoelectric force microscopy (PFM) analyses were carried out in a modified atomic force microscope in PFM mode Nanoscope III, Digital Instruments, using silicon-SPM sensor with Al coating tips (*NANOSENSORS*^{TM} model *PPP-NCHR-20*, l = 125 μm, resonant frequency of 204 – 497 kHz, force constant of 10 - 130 N/m). The topographic images of the film surface were taken simultaneously with the domain images and were collected in non-contact mode.

4.4.7 Superconductor Quantum Interference Device (SQUID)

The superconductor quantum interference device (SQUID) was used to measure the magnetic properties of the $CoFe_2O_4$ nanoparticles. In a SQUID magnetometer, the sample moved through the external magnetic field. A pickup coil is linked to a superconducting loop with parallel Josephson junctions (Figure 4.8). A magnetic flux from the moving sample interrupts the superconducting loop. An applied bias current establishes the superconducting loop and indicates the magnetism of the sample [112].

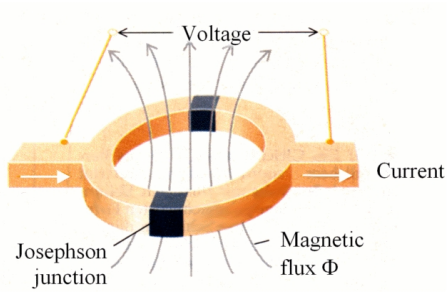

Figure 4.8 Schematic illustration of the superconducting loop with parallel Josephson junctions, [113].

The measurements were performed by varying the magnetic field at constant temperature (typically 10 K, but the same experience was made for other fixed temperature from 10 to 300 K) and by fixing the magnetic field (10 Oe) and changing temperature from 0 to 400 K. The equipment used was *Quantum Design – MPMS* from *Centro de Física Matérica Condensada- Faculdade de Ciências* from University of Lisbon.

Results and Discussion

5. Results and discussion

5.1. Porous ferroelectric thin films

In order to study the effect of different parameters on the microstructure of porous thin films, 6 different samples were prepared. The parameters studied were: a) the effect of type of annealing (with or without ramp); b) the molecular weight (Mw) of the block co-polymer PS-b-PEO: Mw = 40000-53000 $gmol^{-1}$ or 58600-71000 $gmol^{-1}$; concentration of block co-polymer and the withdrawal speed during the deposition. The designations of samples and their parameters are shown in Table 5.1.

Table 5.1 Designations for porous $BaTiO_3$ thin films prepared by different conditions.

Sample	Mw of PS-b-PEO ($gmol^{-1}$)	Concentration of polymer	Withdrawal speed ($mm\ min^{-1}$)
C1	40000-53000	Low*	15.58
C3	40000-53000	Low	29.58
C6	40000-53000	High**	15.58
C8	58600-71000	Low	15.58
C12	58600-71000	High	15.58
C30	58600-71000	Low	96

*Low concentration = 0.083 g ** High concentration = 0.166 g

5.1.1. Effect of experimental parameters on porous microstructures of thin films

- **Effect of type of annealing**

In order to study the effect of the type of annealing, firstly, DTA/TGA measurements (Figure 5.1) were done to know the temperature of $BaTiO_3$ phase crystallization and decomposition of organic content of the films.

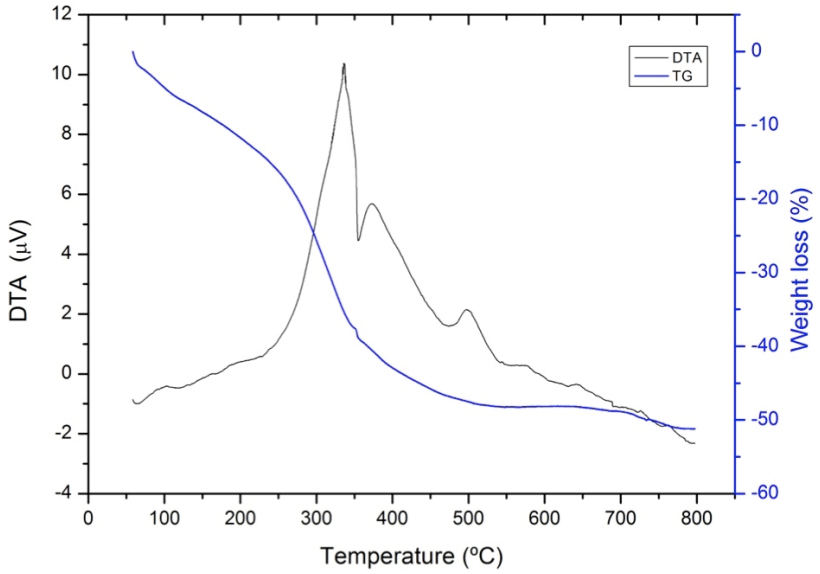

Figure 5.1 Differential thermal (DTA) and thermal gravimetric analysis (TGA) of $BaTiO_3$ dried sol-gel solution illustrating the pyrolysis of co-polymer and other organic compounds up to 500 °C and $BaTiO_3$ crystallization above of 600°C.

The TGA curve (blue line) shows the weight loss during the heating. The major weight loss occurs up to 450 ºC. This weight loss corresponds to the decomposition of the organic components of precursors, solvents and pyrolysis of block co-polymer PS-b-PEO (creating the porosity in the BTO film). It should be noted that the block co-polymer decomposes in two steps corresponding to the degradation of the two polymer blocks. According to literature [13], poly(ethylene oxide) decomposes around 200 ºC while polystyrene decomposes at *ca.* 280 ºC. Above of 450 ºC no other remarkable weight loss was observed.

Here two different types of annealing were studied: (1) 5 minutes at 400 °C (without ramp) and (2) ramp with heating rate 10 °C s^{-1} and plateau of 5 minutes at 400 °C. It was observed that the films should not age on the substrate as damage of the microstructure may occur.

In Figure 5.2, it is shown the effect of calcination type (with or without ramp) for porous thin films prepared with the block co-polymer with both Mw (samples C1 and C8). It can be observed that the type of annealing does not affect the porous microstructure for both thin films prepared with the block co-polymer with different Mw (40-53 k or 58.6-73 k $gmol^{-1}$). Both films present a porous microstructure free of cracks or other defects. Due to this observation, the following studies were only carried out with

annealing for 5 minutes at 400 ºC because it is a quick and less energy consuming method.

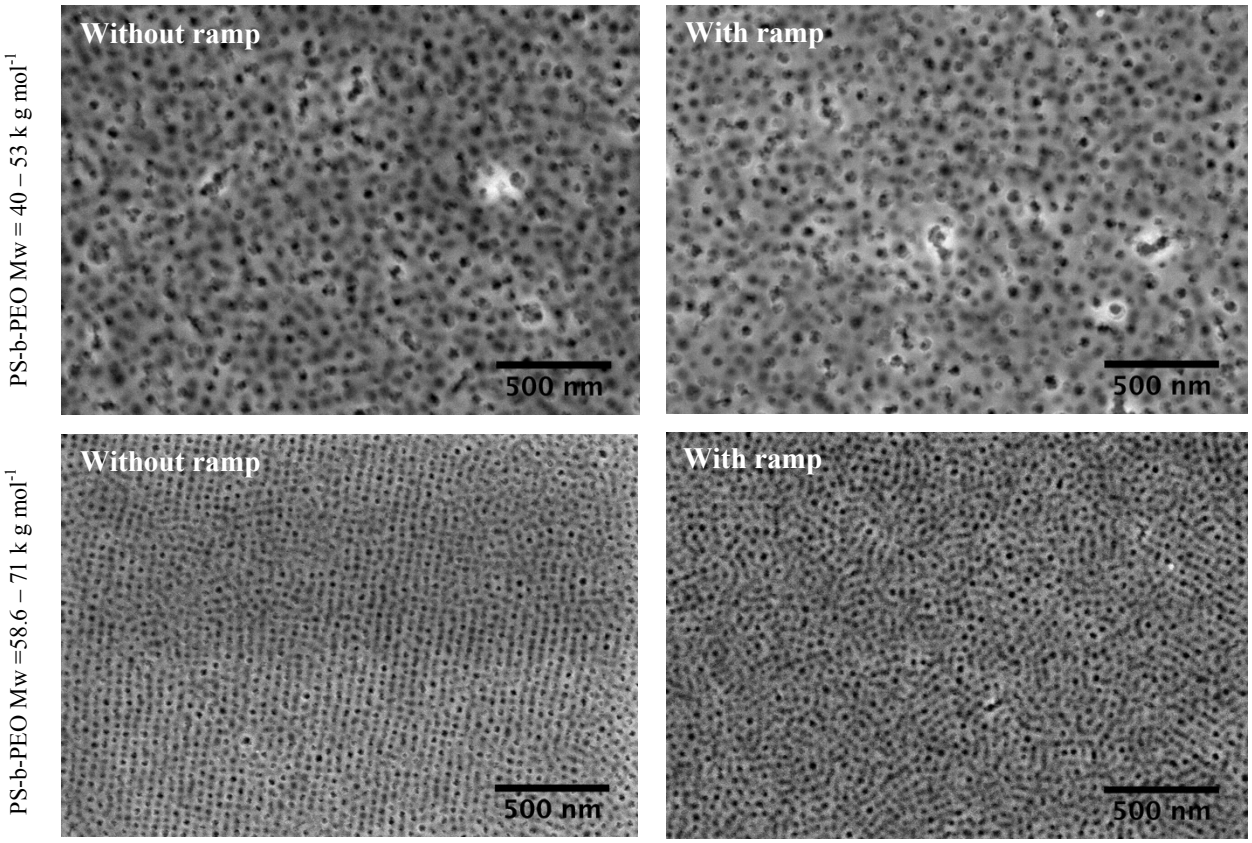

Figure 5.2 SEM micrographs of porous $BaTiO_3$ thin films annealed with or without ramp. The type of annealing does not affect the porous films free of cracks.

- **Effect of polymer Mw**

In order to study the effect of Mw of the block co-polymer on porous microstructure, different molecular weights were used: a) PS-b-PEO 40000-53000 $gmol^{-1}$ and b) 58600-71000 $gmol^{-1}$.

In Figure 5.3 the effect of different Mw on porous microstructures can be clearly observed. The polymer with Mw = 40-53 k $gmol^{-1}$ produces bigger pores with non-uniform shape, while the polymer with Mw = 58.6-71 k $gmol^{-1}$ produces smaller pores with narrow pore size distribution and uniform shape. Furthermore, the porous thin films obtained with higher Mw showed a preferential organization in the microstructure, the pores are well organized revealing hexagonal-like arrays (blue mark). This hexagonal-like arrays were also observed in nanoperforated TiO_2 layers [53] and porous TiO_2 thin films [54].

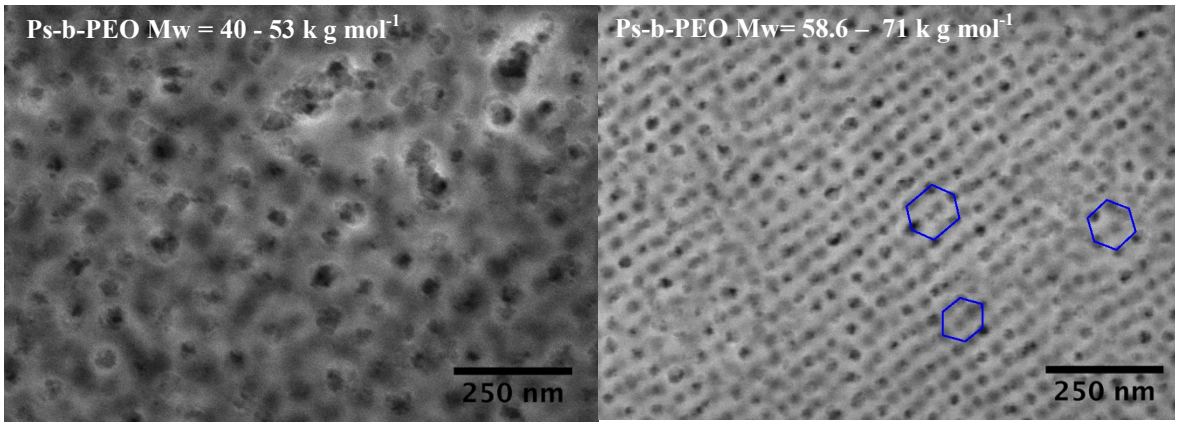

Figure 5.3 SEM micrographs of porous $BaTiO_3$ thin films prepared with polymers with different Mw annealed at 400°C. The polymer with Mw=58.6-71 k $gmol^{-1}$ displays small size but with hexagonal arrangement.

Table 5.2 shows the average of pores size and respective standard deviation (σ) of the films described above. The measurements were carried out using the computer software *ImageJ*. 150 measurements were done for each sample in order to achieve a good sampling. The calculations of average pore size and standard deviation were done using the software *Origin* version 8.5. The porous thin films prepared with Mw = 40-53 k $gmol^{-1}$ present average pore size of 60.7 nm with σ = 6.2 while the thin films prepared with Mw = 58.6-71 k $gmol^{-1}$ present lower average pore size, 28.8 nm, and σ = 2.6. This low value of σ indicates a narrow distribution of pore size for the high molecular weight block co-polymer.

Table 5.2 Average pore size and respective σ for films prepared with PS-b-PEO of different Mw.

Mw ($gmol^{-1}$)	Pore size (nm)	σ (nm)
40-53 k	60.7	6.2
58.6-71 k	28.8	2.6

- **Effect of bock co-polymer concentration**

To study the effect of block co-polymer concentration, it was prepared films using different concentrations of block co-polymer: a) low concentration (0.083 g) and b) high concentration (0.166 g) (double of the first one). The studies were carried out for the two block co-polymers described above.

Figure 5.4 shows the comparison of microstructures obtained from different concentrations of block co-polymer. It is clear that the films obtained from sol-gel solutions with high concentration of block co-polymer display more connected nanopores forming elongated pores as observed inside of yellow marked zones. This fact occurs for both block co-polymers, however in the film obtained from the PS-b-PEO Mw = 40-53 k $gmol^{-1}$, the presence of interconnected pores is more pronounced than for the other one.

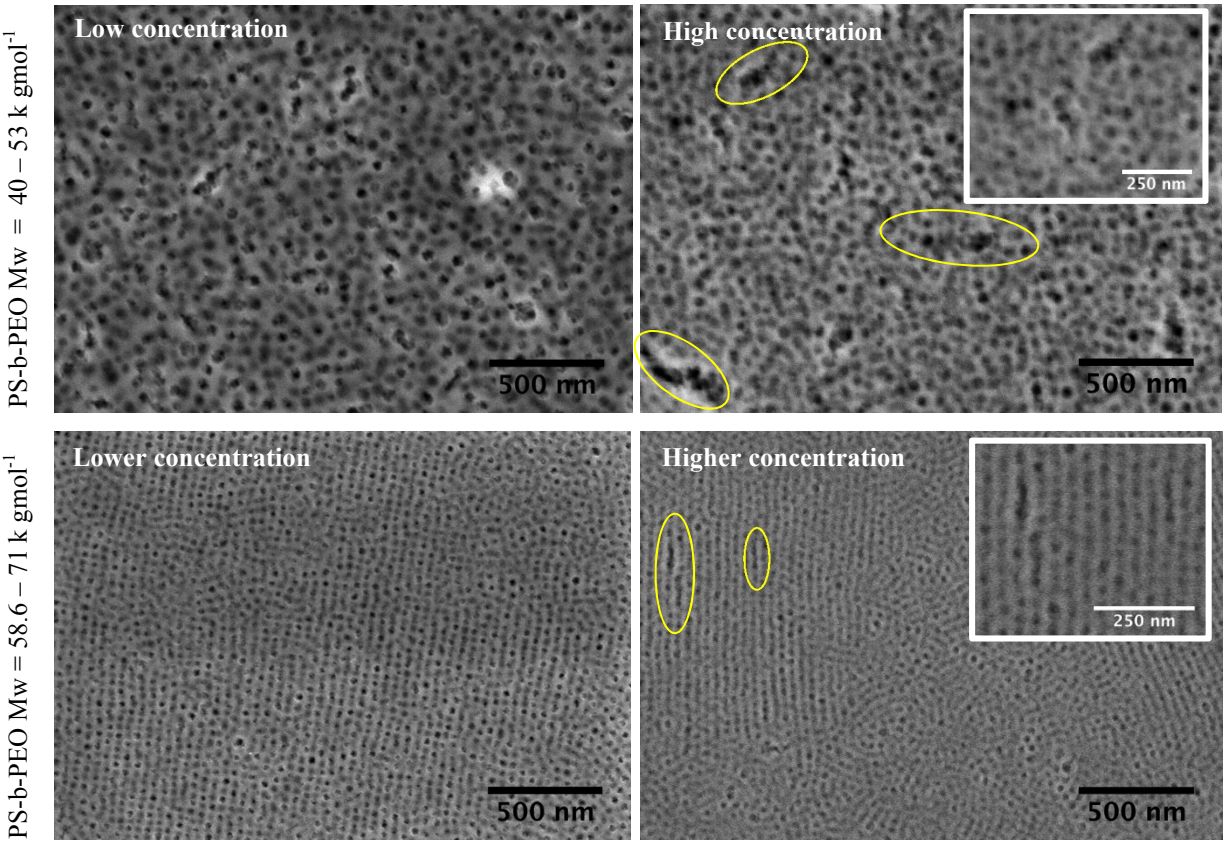

Figure 5.4 SEM micrographs of porous $BaTiO_3$ thin films prepared with different concentrations of block copolymer (Mw=40-53 k and Mw=58.6-73 k $gmol^{-1}$). Low concentration = 0.083 g, High concentration = 0.166 g.

The formation of elongated micropores is due too a high density of pores obtained on the samples prepared with high concentration of block co-polymer. In order to compare the effect of block co-polymer concentration on pore density, for each film, the number of pores present in a square with a side of 500 nm was calculated by using *ImageJ* software. Results are presented in Table 5.3.

Table 5.3 Pores density per nm^2 of $BaTiO_3$ thin films prepared by different concentrations of PS-b-PEO.

Mw ($gmol^{-1}$)	Pore density (pores / nm^2)	
	Low concentration*	High concentration**
40-53 k	2.04×10^{-4}	2.60×10^{-4}
58.6-71 k	4.72×10^{-4}	6.08×10^{-4}

*Low concentration = 0.083 g, **High concentration = 0.166 g

It can be clearly observed that the block co-polymer with high Mw gives films with high density of pores independently of the concentration. The pore walls are much thinner for Mw = 58.6-71 k $gmol^{-1}$ than for Mw = 40-53 k $gmol^{-1}$.

As expected, high concentrations of block co-polymer produces more pores per unit area. To compare the effect of both Mw, the increase of density was calculated by following Eq. 5.1:

$$\frac{\rho_h - \rho_l}{\rho_l} \times 100 \qquad \text{Eq. 5.1}$$

where ρ_h is the pores density at high concentration of block co-polymer and ρ_l is the pores density of lower concentration of block co-polymer.

The Mw = 40 – 53 k $gmol^{-1}$ block co-polymer caused an increase of 27.4% on density while Mw = 58.6-71 k $gmol^{-1}$ caused an increase of 28.8%. These two values of increase can be considered similar to each other.

- **Effect of withdrawal speed on $BaTiO_3$ thin films thickness**

It is known from the literature review that the thickness of thin films prepared by dip-coating depends on withdrawal speed and annealing temperature [13, 54].

In this work the effect of the withdrawal speed on the thickness of $BaTiO_3$ thin films was studied by using two different speeds: 15.58 and 96 mm min^{-1}. SEM micrographs (not shown) prove that the porosity was not influenced by withdrawal speed. In Table 5.4, the film thickness is presented as a function of the withdrawal speed, determined from the SEM micrographs cross-sections, for each withdrawal speed.

Table 5.4 Effect of withdrawal speed on porous thin films thickness*.

Withdrawal speed (mm min^{-1})	Annealing Temp. (ºC)	Thickness (nm)
15.58 (C8)	400	~150
96 (C30)	400	~370-410
15.58 (C8)	650	~110-120
15.58 (C12)	650	~115-145

*determined by using SEM micrographs of the cross-sections.

Comparing the samples C8 and C30, prepared with withdrawal speed 15.58 and 96 mm min^{-1} respectively, it was observed that high speeds induce high thickness. Higher withdrawal speed provokes slow evaporation of solvents inducing high thickness. In this study, it was observed that the film thickness depends on the block co-polymer concentration. Samples C8 and C12 were deposited with the same withdrawal speed, however, the block co-polymer concentration in sol-gel solution is different. However, in the case of C12 the high concentration of block co-polymer was used, resulting in a thicker film. This can be justified by an increase of viscosity of the sol-gel solution. Similar observation was described by Faustini *et al.* [54], who reported that at high withdrawal speeds the final thickness of TiO_2 films is mainly dependent on the viscous drag.

As an example, the cross-section of sample C30 is shown in Figure 5.5. The composition of *Ramtron* substrate is presented in the following section.

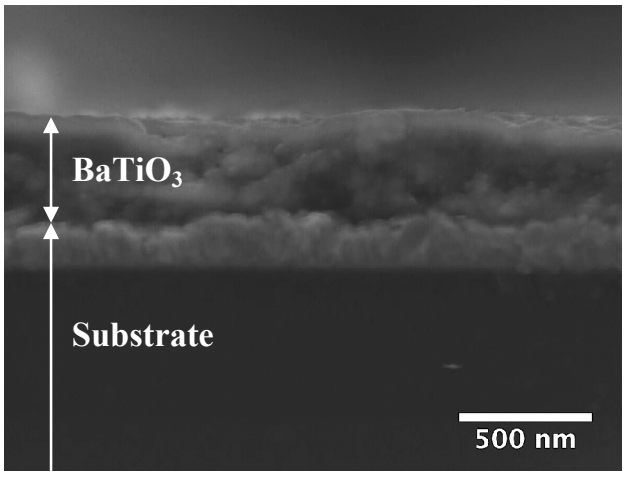

Figure 5.5 Cross-section of sample C30 annealed at 400 °C.

- **Evolution of porous thin film microstructure and morphology with annealing temperature**

Like discussed before in section 3.2 – *Porous ferroelectric thin films*, the thermal treatment step is necessary after deposition. During this step as evidenced by the DTA/TGA measurements (Figure 5.1), the decomposition of the organic content of the films occurs first, followed by the crystallization through nucleation and growth of $BaTiO_3$ crystallites.

To study the evolution of the microstructure of porous thin films and thickness with annealing temperature, the sample C8 was annealed at 3 different temperatures: 400 °C for 5 minutes, 650 °C 6 minutes and 750 °C 2 minutes. At 750 °C the films were treated only for 2 minutes to avoid degradation of the porosity due to particles growth. The thickness measurements were carried out on cross-section samples by SEM and are shown in Table 5.5. The thickness decreases with the annealing temperature due to the crystallization of the porous $BaTiO_3$ thin films.

Table 5.5 Pore size and thickness measurements* of different temperatures annealed C8 films.

Annealing temperature (°C)	Pore size (nm)	Thickness (nm)
400	28.8	~150
650	18.6	~110-120
750	Not measured	~90-100

*measured by *ImageJ*

- ***Ramtron* wafer characterization**

The used substrate from *Ramtron* was characterized by XRD and cross-section in SEM because the producer does not give information about the composition of their multilayer wafers. The composition and thickness of each layer was determined by SEM assisted by EDS analysis, Figure 5.6.

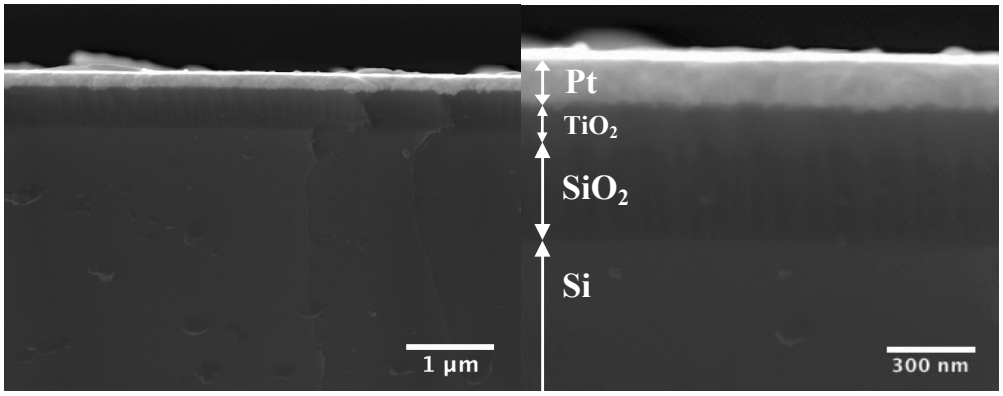

Figure 5.6 SEM micrographs of multilayer ($Pt/TiO_2/SiO_2/Si$) *Ramtron* wafer cross-section displaying different layers without any thermal treatment.

EDS spot analysis allowed to determine the composition of each layer of Ramtron wafer. The major difficulty in this analysis was the determination of the TiO_2 layer probably due to ultra thin thickness. By SEM micrographs, even when assisted by EDS analysis, is difficult to distinguish the TiO_2 layer. The TiO_2 layer should be located between platinum (Pt) and silica (SiO_2) layers (please see on the left micrograph of Figure 5.6) in order to ensure the adhesion of the Pt. The thickness of platinum layer was easily determined. Due to the difficulty in distinguishing the boundary between TiO_2 and SiO_2 layers, these two layers were measured together as having approximately 450 nm, Table 5.6. Probably, the TiO_2 layer is less than 100 nm of thickness.

Table 5.6 Composition and layer thickness of *Ramtron* wafers determined by SEM/EDS.

Composition	**Thickness (nm)**
Pt	150
$TiO_2 + SiO_2$	450
Si	Not measured

To support the results of SEM/EDS, XRD analyses were carried out. The Figure 5.7 displays the XRD patterns of bare substrate with and without thermal treatment.

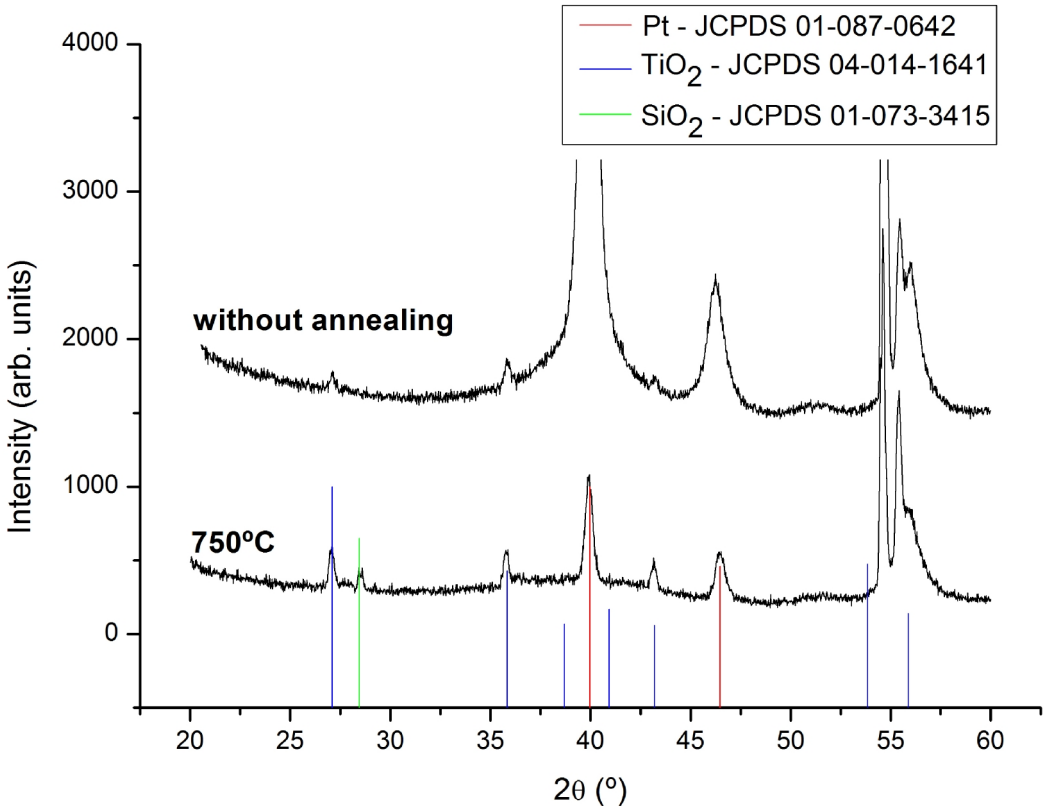

Figure 5.7 XRD patterns of Ramtron wafer with and without thermal treatment.

The observed reflections in XRD patterns of *Ramtron* wafer could be assigned to Pt, TiO_2 and SiO_2 confirming the elements identification of the SEM/EDS analysis. Furthermore, the peaks in XRD patterns indexed to SiO_2 JCPDS 01-073-3415 do not match in the exact values of 2θ, probably due to the presence of layers on the top of the SiO_2. The reflection peaks observed around $2\ \theta = 55\ °$ are attributed to substrate and can be related with forbidden peaks of Si.

Figure 5.8 shows the X-ray diffraction patterns of sample C8 annealed at different temperatures: 650, 700 and 750°C.

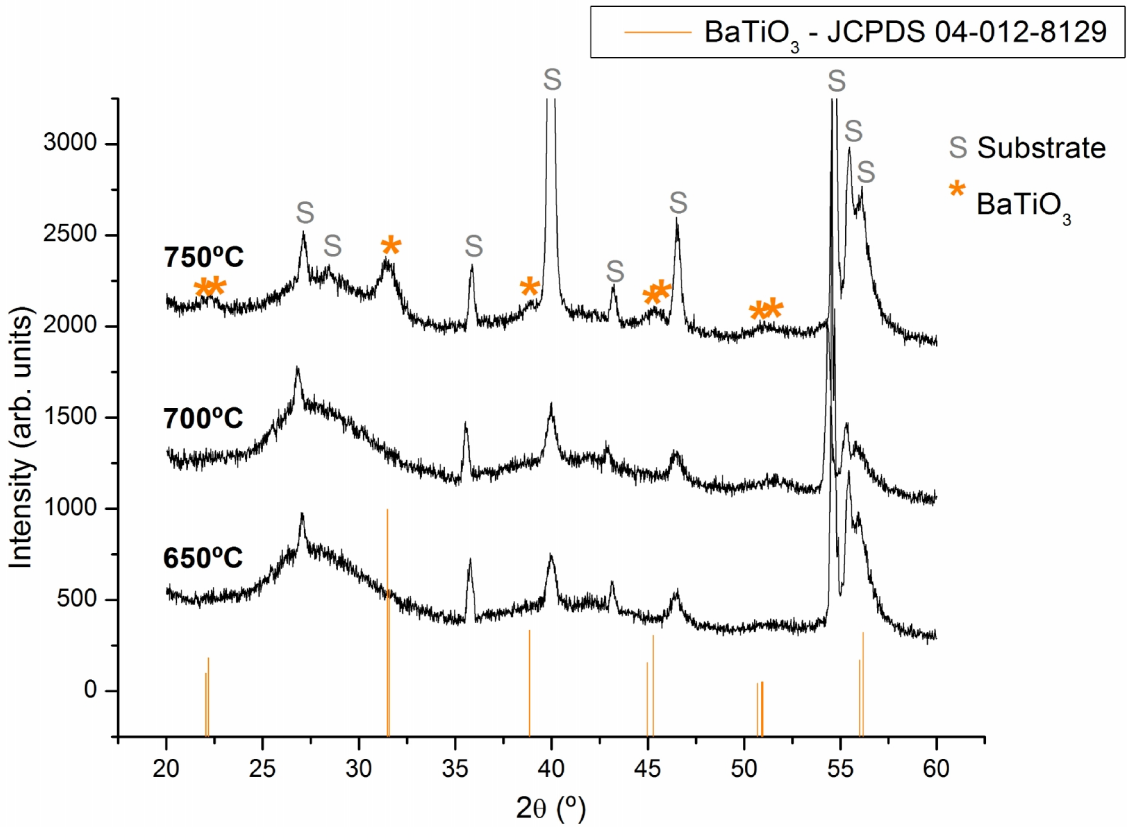

Figure 5.8 X-rays diffraction patterns of porous $BaTiO_3$ thin films annealed at different temperatures (650, 700 and 750°C).

The X-ray patterns confirmed the formation of tetragonal $BaTiO_3$ (for comparison, the reflections corresponding to $BaTiO_3$ tetragonal phase with space group P4mm according to the JCPDS database card no. 04-012-8129 are shown as solid orange lines) for temperatures above of 650°C. For higher temperatures $BaTiO_3$ becomes more crystalline. No other phases of $BaTiO_3$ or other compounds were detected indicating the purity of tetragonal $BaTiO_3$ phase. The peaks identified with an S were indexed to substrate by comparing this XRD patterns with the patterns of Figure 5.7.

5.1.2. Piezoresponse studies

In Table 5.7 and Table 5.8 are displayed the results of the Piezoresponce Force Microscopy study for different samples.

In the topography images, the dark regions correspond to larger depths, whereas the lighter ones represent the ones closer to the surface. Thus, the topography image is a representation of the film surface and, as a first approximation, of the apparent porosity.

In the piezoresponse images, the dark regions correspond to ferroelectric domains oriented towards the substrate and the lighter ones towards the surface. The dark regions that reveal large pores in the topography image continue to appear in the PFM image and they do not correspond to piezoresponse. However, the appearance of different domains in the PFM image does not necessarily imply the existence of polarization, since a very deep region (or else high) can present dark (light) domains in the PFM image. Consequently, a uniform region is preferred for better results. However, such requirement is difficult to be reached due to the thin porous films' limitations discussed above. As a result, lower piezoresponse signal is observed, accompanied by high noise.

In Table 5.7 the evolution of the ferroelectric domains with increasing applied voltage is presented for the case of sample C1, with a scanning size of 7 μm. By the application of 10 V we can observe the appearance of a few ferroelectric domains with opposite orientation. Increasing voltage results in increased contrast between the already existent domains. However, apart from the expected low piezoresponse signal, high noise - clearly observed when no voltage is applied to the sample - weakens even more the contrast between the domains. Finally, due to the high roughness of the surface there is an evident deformation of the grain morphology, as observed by the topography image. Such effects could be explained by an abrupt bend of the cantilever tip when in contact with the island-like surface, which provokes very dark regions right after the high ones. An apparent wear of the tip due to this violent interaction results in misrepresentation of the realistic shape of the grains, conferring them an elliptical geometry.

Table 5.7 Topography and piezoresponse images of sample C1 (low concentration of block co-polymer Mw = 40 – 53 k $gmol^{-1}$, withdrawal speed = 15.58 mm s^{-1}) for 0, 10, 15 and 20V applied voltage.

Voltage	Topography	Piezoresponse
0 V	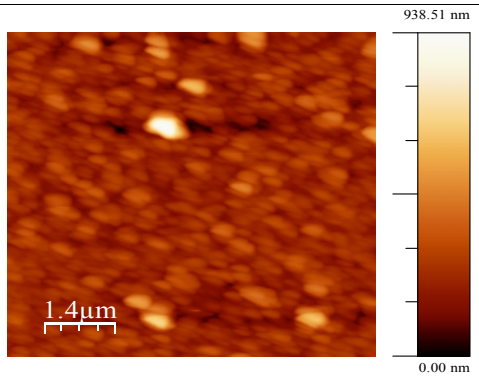	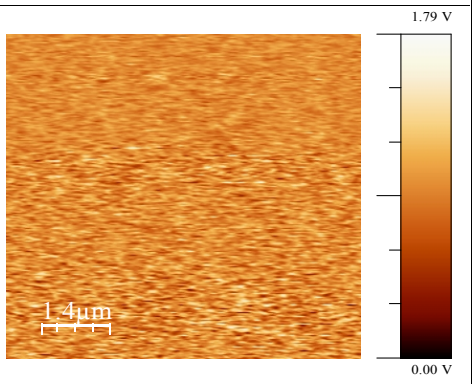
10 V	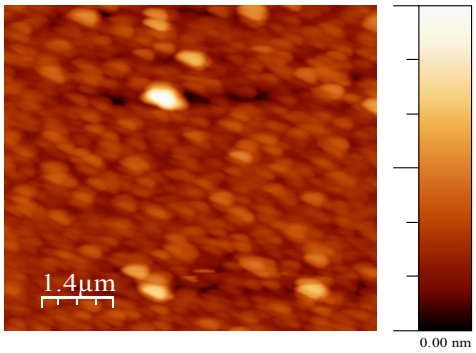	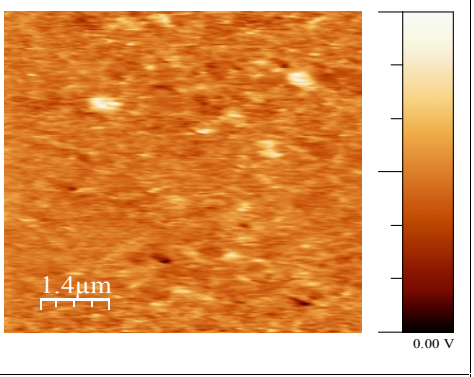
15 V	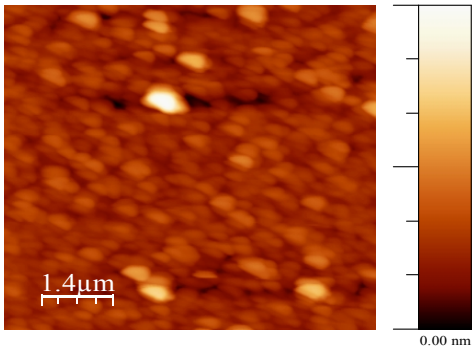	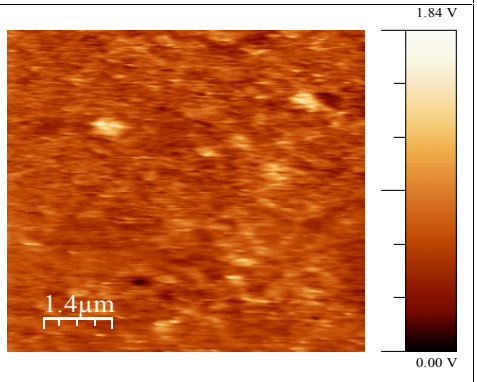
20 V	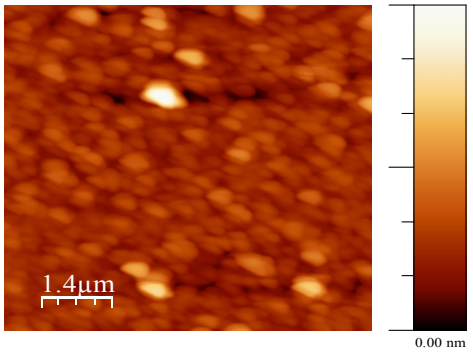	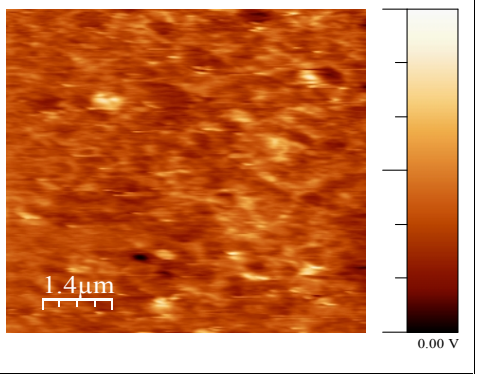

In Table 5.8 are presented the topography and piezoresponse characterization of samples C1, C3, C8, C12 and C30 for different scanning sizes and applied voltage. The fourth column corresponds to the topography image and the last to the piezoresponse image. The most interesting comparisons to be made are those for varying thickness, block co-polymer Mw and polymer concentration.

For the study of thickness effect to piezoresponse, taking into account that the thickness relation between samples was C3 < C1 = C12 = C8 < C30, two groups could be chosen, keeping in each one the concentration and type of polymer constant, but varying withdrawal velocity during dip-coating: C1-C3 and C8-C30. Sample C3 corresponds to a higher deposition velocity than that of C1, therefore being the thinnest film. A higher contrast between the ferroelectric domains is apparent on the C1 piezoresponse image, accompanied by an enhanced definition. Such a result was expected, since increased thickness is related to increased quantity of deposited matter, therefore enhanced accumulation of dipole components, which yields higher polarization. The second group does not follow the same behavior, probably due to the combination of the problems mentioned above.

The use of high block co-polymer Mw results in smaller pores in the ferroelectric matrix. A representative case for this kind of study is between C8 and C1 samples, since they have equivalent thickness, but C8 corresponds to the high block co-polymer Mw, thus smaller pores and enhanced polarization, which can be observed in the piezoresponse image by a higher number of ferroelectric domains appearing in the case of C8.

Lastly, a higher polymer concentration turns the solution more viscous, which has a severe effect on the homogeneity of the film thickness, as well as on the elongated pores as observed before in Figure 5.4. C12 sample was prepared with higher polymer concentration and, apart from the expected weak piezoresponse, it was very difficult to characterize, due to its extremely rough surface, which was destroying the cantilever tip and providing falsified topography and piezoresponse images.

Table 5.8 Topography and piezoresponse images for the samples C1, C3, C8, C12 and C30.

Sample	Scanning Size	Voltage	Topography	Piezoresponse
C1	7 µm	10 V	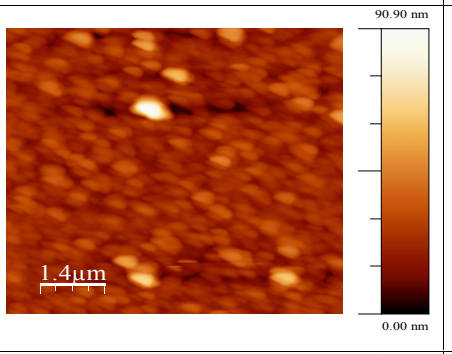	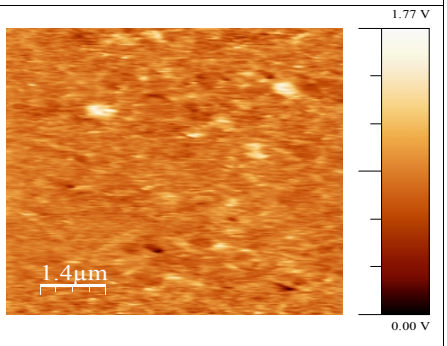
C3	7 µm	10 V	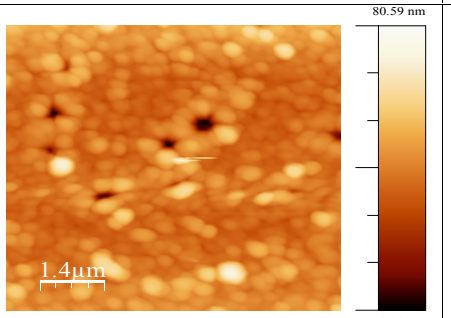	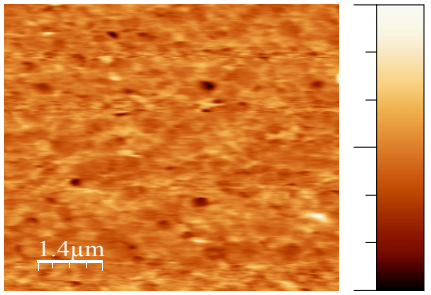
C8	5 µm	10 V	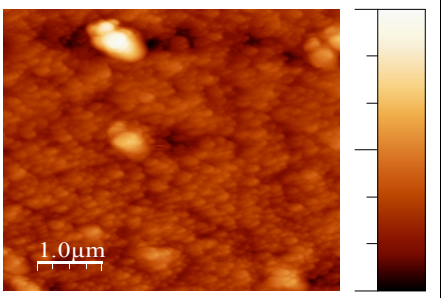	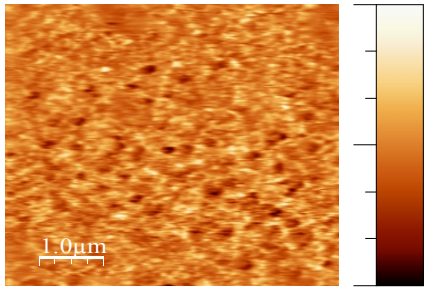
C12	3 µm	10 V	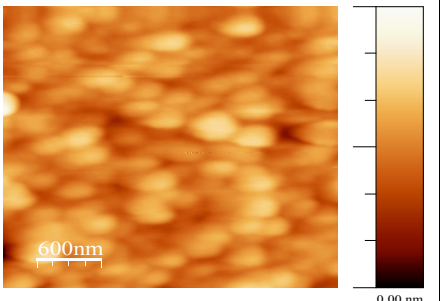	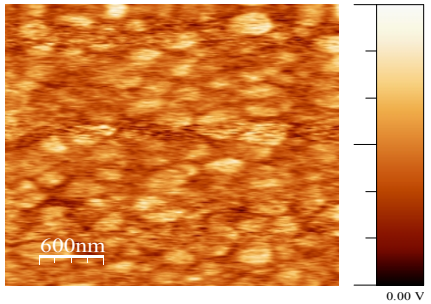
C30	5 µm	20 V	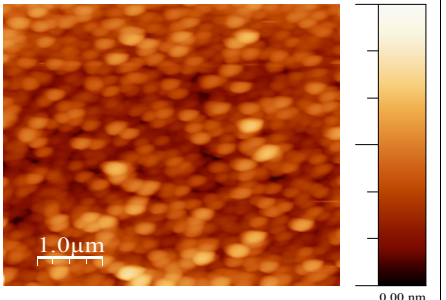	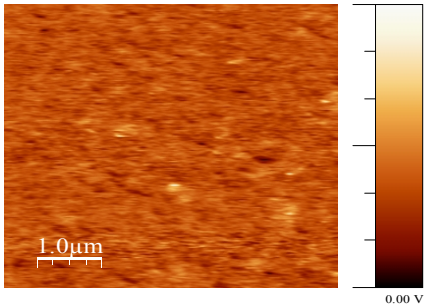

5.1.3 Summary

Porous $BaTiO_3$ thin films were successfully produced by dip-coating combined with EISA. The effect on the microstructure of different parameters such as type of annealing, Mw of block co-polymer, concentration of block co-polymer and withdrawal speed was studied. The type of annealing (with or without ramp) does not affect the microstructure. High block co-polymer Mw produces small pores and high concentration of polymer induces the formation of interconnected pores due to high density of pores. High annealing temperature reduces the pore size and the thickness of the film. High withdrawal speeds form thick films. These porous structures are good candidates to pyroelectric applications or future functionalization with nanoparticles composing a multifunctional material.

5.2. $CoFe_2O_4$ nanoparticles

In this section, the results of $CoFe_2O_4$ synthesis are shown. The effect of different hydrothermal synthesis (HS) parameters such as: temperature and time of HS, additive effect, metal ions and base concentration was discussed.

5.2.1. Synthesis temperature effect

To study the temperature effect, the syntheses were performed under the same condition but at different temperatures: 100, 150, 200 and 230 ºC. The maximum temperature is limited to 230 °C due to the limitations of properties of Teflon-lined autoclave. For all experiments, the autoclave was filled up to 50% of volume. In Figure 5.9 are displayed the TEM micrographs of nanoparticles synthesized at 100 and 230 °C.

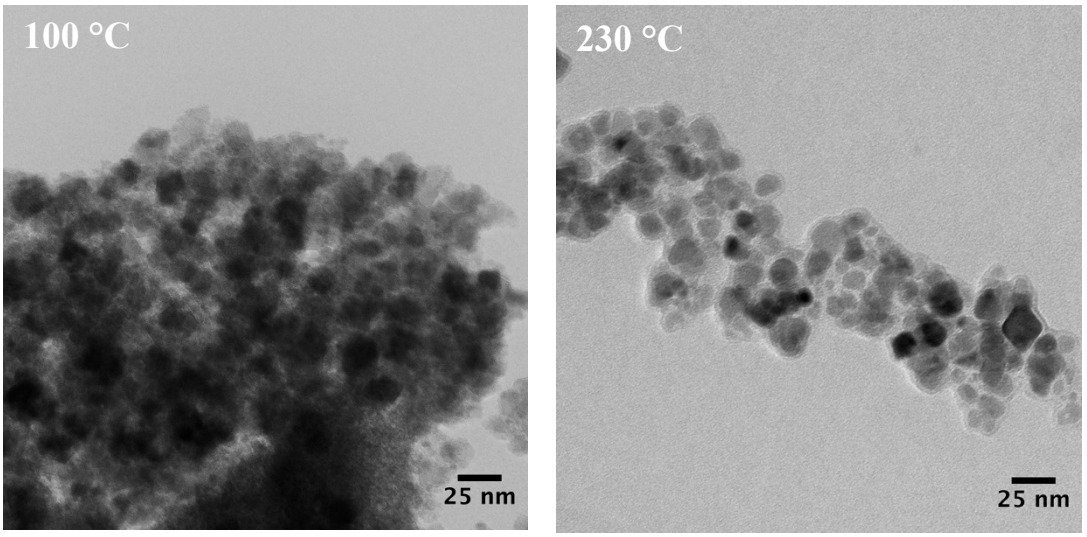

Figure 5.9 TEM micrographs of $CoFe_2O_4$ nanoparticles obtained from hydrothermal synthesis at 100 °C and 230 °C.

For low hydrothermal synthesis temperature, the nanoparticles present a fog-like shape, *i.e.* very agglomerated with none defined particle shape, due to the low crystallinity of the material [58]. As the temperature increases nanoparticles tend to have rounded shape and some of them cubic shape. The average sizes of CFO nanoparticles obtained at 100 °C and 230 °C were about 12.9 nm and 16.1 nm, respectively, Table 5.9. The sizes were measured in *ImageJ* software.

Table 5.9 Average particle size (D_{TEM}), standard deviation (σ) and specific surface area (A_{BET}) of samples prepared at different temperatures of HS.

HS temperature (ºC)	D_{TEM} (nm)	σ (nm)	A_{BET} ($m^2 g^{-1}$)
100	12.9	3.1	93.5
150	Not measured	Not measured	83.0
200	20.1	2.2	53.0
230	16.1	3.0	90.3

The average particle size measured by TEM micrographs is in good agreement with the crystallite size (Figure 5.10) estimated by Scherrer formula suggesting that each individual particle is a single crystal. The crystallite size increases from 15.6 to 19.1 nm with the temperature increase from 100°C to 150°C. This increasing should be due to the coalescence and Ostwald ripening as observed in previous studies [73]. For HS temperatures above 150 °C, the crystallite size decreases. This fact could be associated to a fast nucleation of the nanoparticles at higher synthesis temperature, with formation of a huge number of nuclei and rapid decrease of the precursor concentration on the medium preventing crystallite growth [73].

On the left side of Figure 5.10 X-rays diffraction patterns of $CoFe_2O_4$ nanoparticle obtained from different HS temperatures are presented. Single crystalline cubic spinel phase is formed which is in accordance to JCPDS card no. 04-008-4497. The products prepared below 200 °C show lower crystallinity than the products obtained at high HS temperatures.

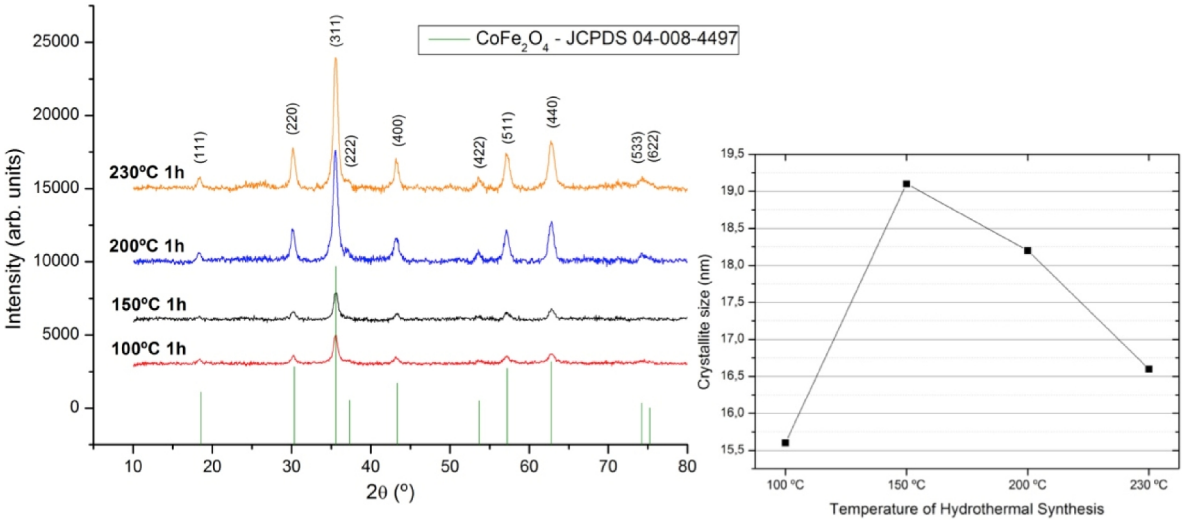

Figure 5.10 X-ray diffraction patterns (left) and evolution of crystallite size (right) of $CoFe_2O_4$ nanoparticles obtained at different temperatures of hydrothermal synthesis during 1h.

The Figure 5.11 presents the magnetic properties of $CoFe_2O_4$ nanoparticles as a function of HS temperature. All samples exhibit a typical ferromagnetic hysteresis loop. As the synthesis temperature increases, the saturation magnetization increases from 53,7 to 73,2 emu/g, as expected and in accordance to the high crystalline degree of these samples. Similar study was carried out by Goh *et al* [73], where CFO nanoparticles with sizes between 15.6 and 33.1 nm present saturation magnetization of 56.8 and 73.2 emu/g respectively.

It could be observed a drop on the magnetization at 10 K when the field is around 0 Oe. This effect was more pronounced for the sample prepared at 100 ºC and became less significant with the increase of the temperature of hydrothermal synthesis. According to the literature this may occur due to the presence on the samples of soft magnetic species such as FeOOH that easily can be formed at low temperature in very small quantity [114].

In the left side of Figure 5.11 is presented the zero field cooling (ZFC) and filed cooling (FC) curves. The peak of these two curves is called blocking temperature. The blocking temperature (characterized by blocked magnetic moments) is between 350 and 400 °C for all samples.

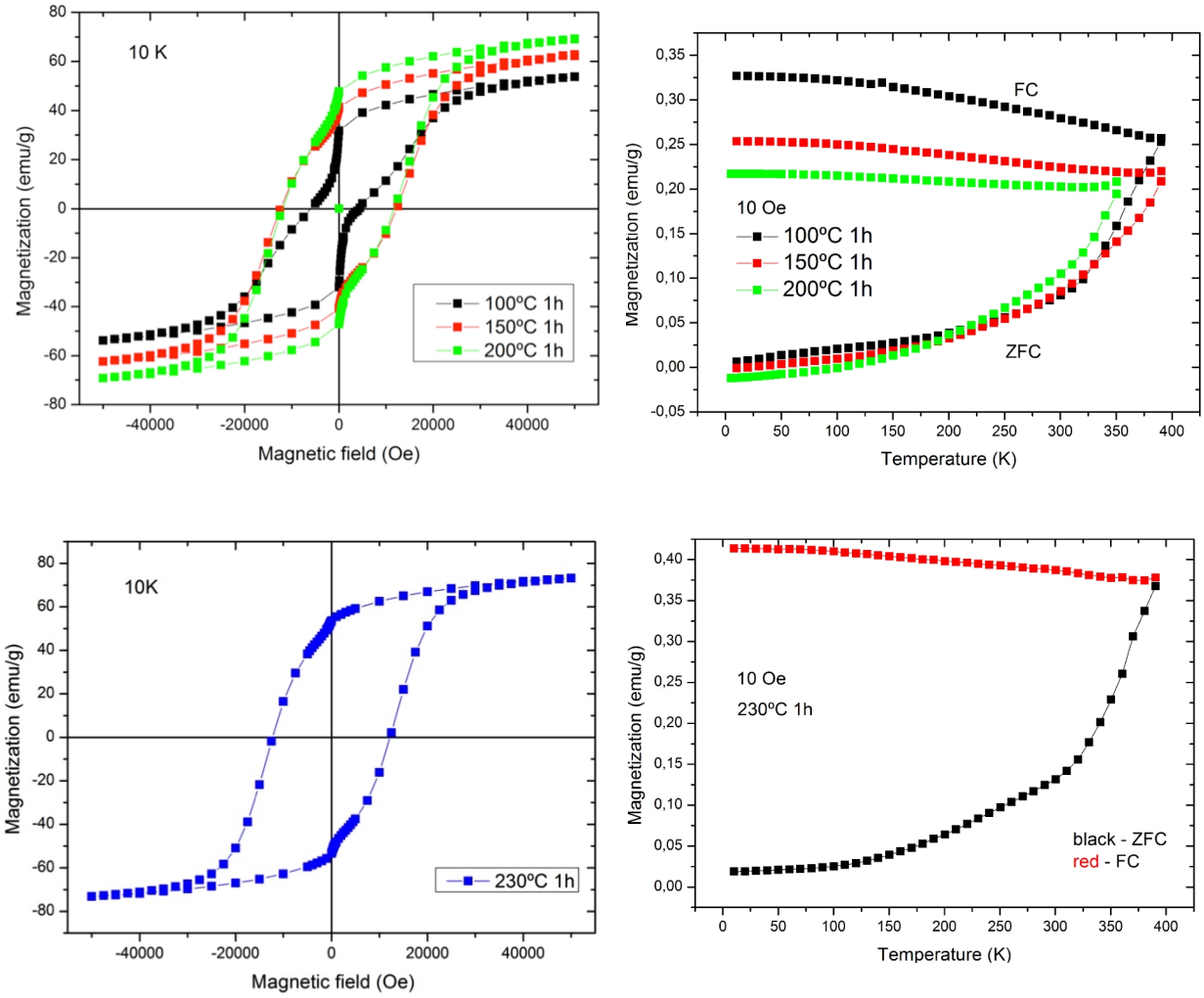

Figure 5.11 Hysteresis loops measured at 10 K (left side) and Magnetization versus Temperature curves at constant magnetic field (10 Oe) (right side) of the nanoparticles prepared at different temperatures of HS.

In Figure 5.12 is displayed the hysteresis loops measured at different temperatures for the sample prepared at 200 °C 1h. The saturation magnetization (*Ms*) and the coercive field (*Hc*) decrease with the increase of measurement temperature. At room temperature nanoparticles show a superparamagnetic behaviour, *i.e.*, very low coercive field [81]. The coercive field decreases from 11889 Oe (measured at 10 K) to 703 Oe (measured at 300 K). The saturation magnetization decreases from 69.1 to 60 emu/g.

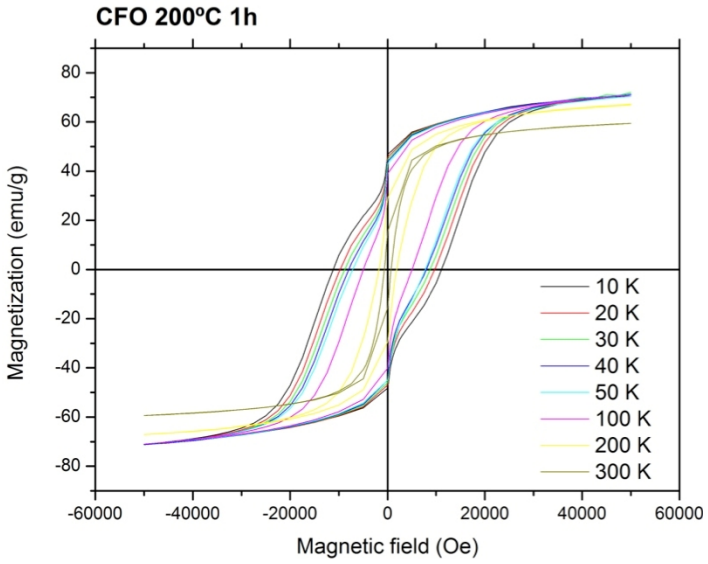

Figure 5.12 Hysteresis loops obtained at different measuring temperatures for the $CoFe_2O_4$ nanoparticles prepared at 200ºC 1h.

Table 5.10 summarises the characteristics of $CoFe_2O_4$ nanoparticles obtained at different HS temperatures.

Table 5.10 Summary table of $CoFe_2O_4$ nanoparticles obtained at different temperatures of HS.

HS temperature	Nanoparticles size* (nm)	Crystallite size** (nm)	Ms (emu/g)	Mr (emu/g)	Hc (Oe)
100 °C	12.9	15.6	53.7	31.8	6021
150 °C	Not measured	19.1	62.3	41.4	12397
200 °C	20.1	18.2	69.1	47.7	11889
230 °C	16.1	16.6	73.2	53.6	12304

*measured by ImageJ, **measured by Scherrer formula

5.2.2. Synthesis time effect

The temperature chosen to investigate the effect of the hydrothermal synthesis time was 230°C. The hydrothermal synthesis was conducted during 1, 3 and 24h.

Figure 5.13 depicts the morphology of the nanoparticles obtained at 230 °C during 1h and 24 h.

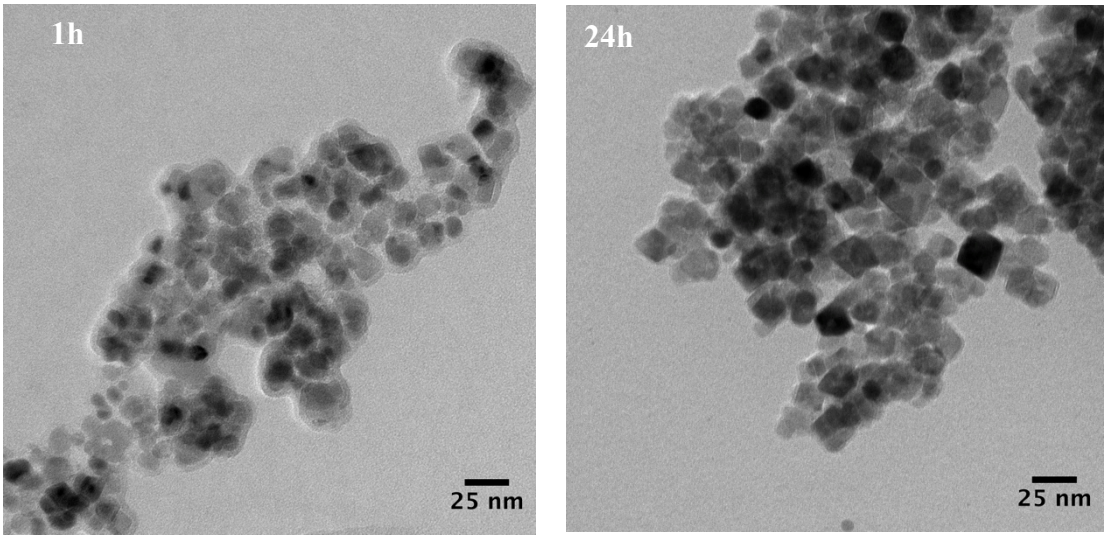

Figure 5.13 TEM micrographs of $CoFe_2O_4$ nanoparticles synthesized during different times of hydrothermal synthesis (1 and 24h), illustrating the increasing of nanoparticles size with increasing time.

Nanoparticles obtained at 230 °C for 24 h show bigger sizes and cubic shape than those obtained in short reaction times. However, from the TEM micrograph of nanoparticles prepared at 230 °C for 24 h, it can be conclude that the size distribution is not narrow due to the presence of small particles. The average size increases from 16.1 to 28.4 nm when the HS time increases from 1 to 24h, Table 5.11.

Table 5.11 Average particle size (D_{TEM}), standard deviation (σ) and specific surface area (A_{BET}) of samples prepared during 1, 3 and 24h of HS.

HS time (h)	D_{TEM} (nm)	σ (nm)	A_{BET} ($m^2\ g^{-1}$)
1	16.1	3.0	90.3
3	Not measured	Not measured	100.7
24	28.4	8.2	65.9

Figure 5.14 shows the XRD patterns and evolution of crystallite size of $CoFe_2O_4$ nanoparticles obtained during different times of hydrothermal synthesis.

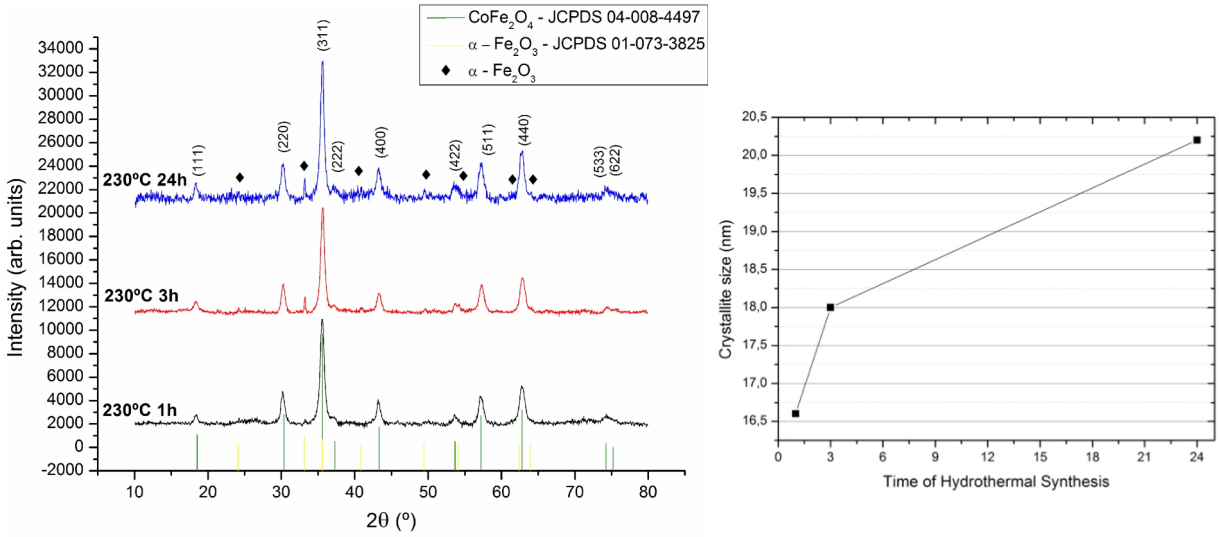

Figure 5.14 X-ray diffraction patterns showing the hydrothermal synthesis time effect on crystallinity (left) and crystallite size (right) of $CoFe_2O_4$ nanoparticles. Besides the $CoFe_2O_4$ phase, it was found the presence of an antiferromagnetic phase, α-Fe_2O_3.

All characteristic peaks of $CoFe_2O_4$ could be observed in XRD patterns, however, for longer times of hydrothermal synthesis another crystalline phase was detected, hematite (indexed JCPDS no. 01-073-3825). This iron oxide is antiferromagnetic [22] slightly present after 3 hours and clearly observed after 24 hours. The crystallite size measurements indicate that the crystallite size increases from 16.1 to 20.2 nm with HS time increase. By comparing the average size of particles measured by TEM micrographs and crystallite sizes, it can be concluded that the nanoparticles are single-crystals.

Figure 5.15 presents the magnetic properties of nanoparticles against the HS time. All of the samples exhibit typical ferromagnetic hysteresis loop.

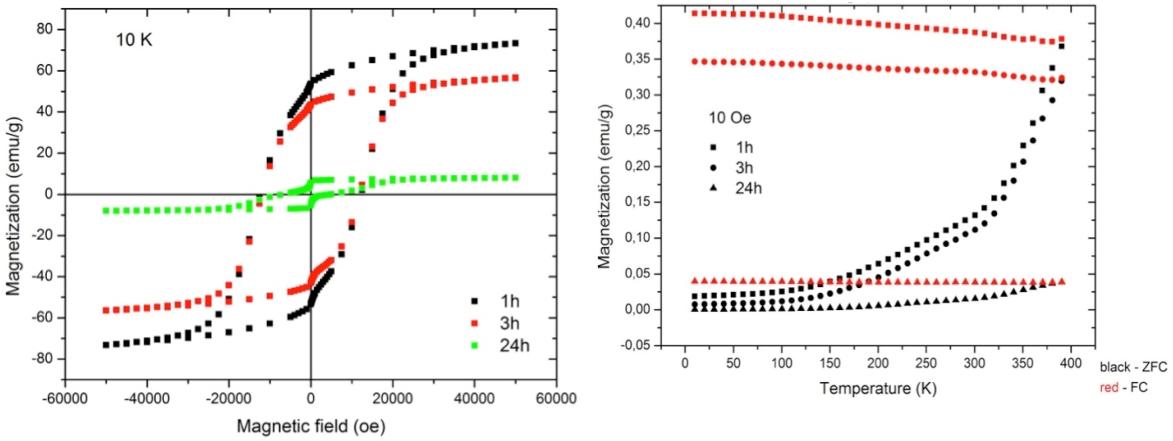

Figure 5.15 Hysteresis loops measured at 10 K for samples obtained at different times of hydrothermal synthesis (left) and Magnetization versus Temperature curve at constant magnetic field (10 Oe) (right) $CoFe_2O_4$ nanoparticles prepared at 230 °C at different HS reaction times.

Normally, the Ms increase with particle size [73]. However, it does not happen in this study. Saturation magnetization decreases drastically from 73.2 to 8.04 emu/g when the HS time increase from 1 to 24h. This decrease of saturation magnetization is clearly due to the presence of the antiferromagnetic phase, α-Fe_2O_3 detected by XRD. The blocking temperature is around 390 °C for all samples.

The summary of characteristic of nanoparticles obtained at different times of HS is presented in Table 5.12.

Table 5.12 Summary table for $CoFe_2O_4$ nanoparticles prepared at 230ºC for 1, 3 and 24h of HS

HS time (h)	Nanoparticles size (nm)	Crystallite size (nm)	Ms (emu/g)	Mr (emu/g)	Hc (Oe)
1	16.1	16.6	73.2	53.6	12304
3	Not measured	18.0	56.4	43.5	22933
24	28.4	20.2	8.04	5.6	6662

5.2.3. PVP addition effect

For the aim of this work it was important to obtain monodispersed nanoparticles of $CoFe_2O_4$. For this, it was studied the effect of the addition of different concentrations of PVP as mentioned in section 4.2. PVP (Figure 5.16) is a water-soluble polymer resulting from the polymerization of the monomer N-vinyl pyrrolidone. It is a strong Lewis base

and consequently can interact with other molecules by the formation of hydrogen bonds or can act as a proton acceptor. These chemical properties give PVP a strong affinity to bind ions surface, forming a layer, which theoretically avoids further aggregation, acting as growth inhibitor and dispersant [115]. PVP has been studied as a capping agent in the preparation of ferrites by thermal decomposition [63, 116, 117]. The authors proposed an interaction between the metal ions and the nitrogen of PVP. PVP is commonly used to obtain ferrite fibers by electrospinning because as it interacts with the metal ions, it can allow the preparation of hollow fibers or it can ensure the preparation of individual fibers [118, 119].

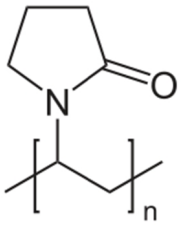

Figure 5.16 PVP monomer.

Figure 5.17 shows the TEM micrographs of $CoFe_2O_4$ nanoparticles prepared without additive and with PVP10 at 200 °C by 1 h.

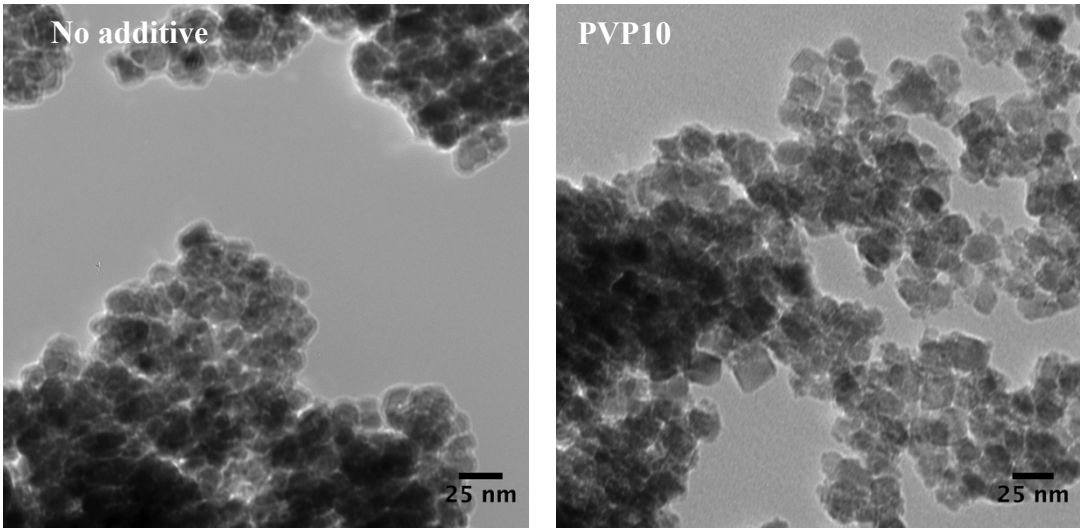

Figure 5.17 TEM micrographs of $CoFe_2O_4$ nanoparticles synthesized without and with PVP, both prepared at 200°C 1h.

In this study, the addition of PVP10 does not affect the shape of nanoparticles, however the particle size increases with PVP addition. The average particle size of synthesis with different concentrations of PVP, measured in the TEM micrographs, are shown in Table 5.13.

Table 5.13 Average particle size (D_{TEM}), standard deviation (σ) and specific surface area (A_{BET}) of $CoFe_2O_4$ nanoparticles prepared with different concentrations of PVP.

Additive	D_{TEM} (nm)	σ (nm)	A_{BET} (m^2 g^{-1})
None	20.1	2.2	53.0
PVP5	Not measured	Not measured	60.2
PVP10	23.6	3.6	59.9

The size of nanoparticles increases from 20.1 to 23.1 nm with addition of PVP10. The presence of PVP on hydrothermal synthesis of CFO nanoparticles seems to modify the kinetics of the growth process. Further studies such as reaction time in the presence of PVP needs to be done.

Figure 5.18 shows X-ray diffraction patterns and evolutions of crystallite size for samples prepared without and with PVP at different HS temperatures by 1 h.

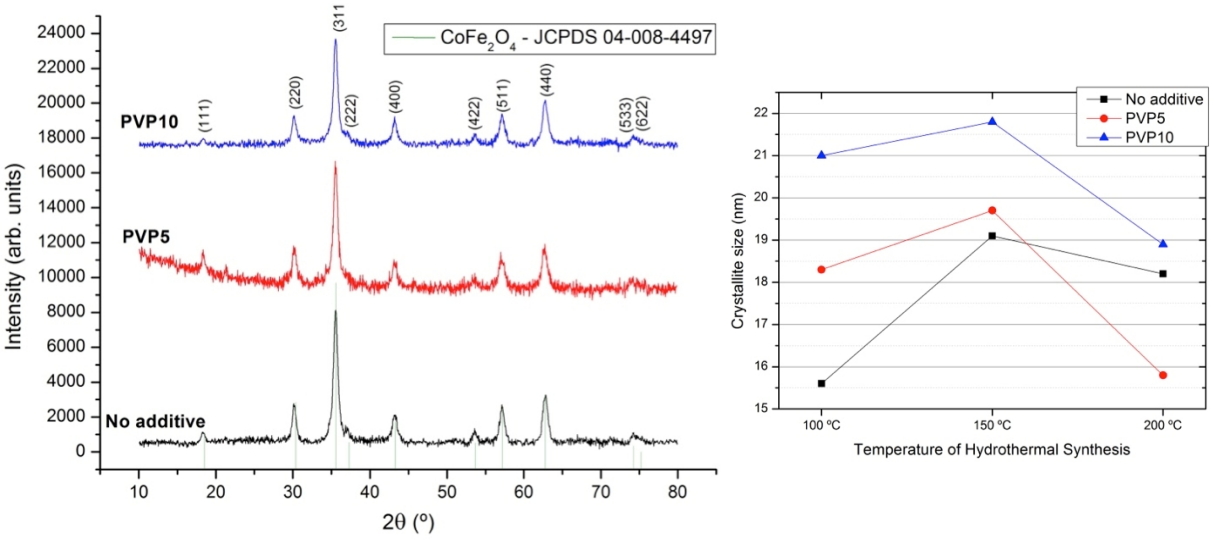

Figure 5.18 X-ray diffraction patterns showing that the PVP does not influenced the $CoFe_2O_4$ phase formation (left) and PVP effect on crystallite sizes (right) of $CoFe_2O_4$ nanoparticles prepared at 100, 150 and 200 °C.

The addition of PVP does not change the crystalline phase formation; only $CoFe_2O_4$ phase was detected in X-ray diffraction patterns. The degree of crystallinity is similar independently of the addition of PVP or of the PVP concentration (Figure 5.18). However PVP influences the crystallite size but keeps the trend with the temperature variation. The crystallite sizes in the samples with PVP are bigger than for the PVP-free sample at 100 °C. The crystallite size grows up to 150 °C in all samples and decrease afterwards with the increase of temperature to 200 °C. PVP containing samples show a bigger decrease in crystallite size when the temperature increases from 150 to 200 °C. The samples with PVP present exactly the same slope in all temperature ranges. For HS temperatures above of 150 °C, like observed in section 5.2.1 – *Synthesis temperature effect*, the crystallite size decreases due to fast nucleation at high temperatures.

DTA/TGA measurements were carried out aiming to understand the PVP function (capping agent or not) in hydrothermal synthesis of $CoFe_2O_4$ nanoparticles. In Figure 5.19 is presented DTA/TGA of $CoFe_2O_4$ nanoparticles prepared at 200 °C 1h without (left) and with PVP10 (right).

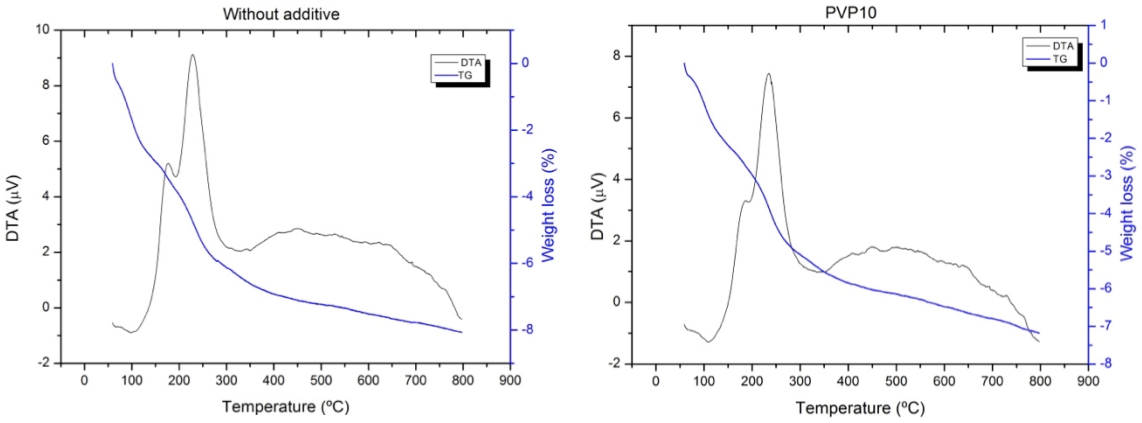

Figure 5.19 DTA/TGA of $CoFe_2O_4$ nanoparticles prepared without and with PVP10 at 200 °C during 1h.

The weight loss with temperature of CFO nanoparticles prepared without and with PVP10 is similar (TGA curves). The percentages of weight losses are presented in Table 5.14.

Table 5.14 Weight losses of $CoFe_2O_4$ nanoparticles prepared at 200 °C 1h without and with PVP10, calculated from TGA curves.

Sample	Weight loss (%)		
	< 150 °C	**150 – 500 °C**	**500 - 800 °C**
No additive	2.5	4.7	0.9
PVP10	1.8	4.4	0.9

The first weight loss up to 150 °C was 2.5% for CFO nanoparticles prepared without PVP and 1.8% for PVP10, which can be attributed to the evaporation of water adsorption. From measurements of size of nanoparticles (Table 5.14), it is known that the nanoparticles prepared in absence of PVP presented small size than those prepared with PVP10, which means that the nanoparticles with small size have high capacity to adsorb water molecules in their surface, leading to a higher weight loss in the temperature range up to 150 °C when compared with PVP10. Furthermore, as the temperature increases the weight loss between nanoparticles prepared without and with PVP10 tends to be equal, which suggests that the PVP was not adsorbed on the surface of particles, thus not acting as capping agent [115].

Hysteresis loops of CFO nanoparticles prepared with and without PVP at 200 °C 1h are presented in Figure 5.20.

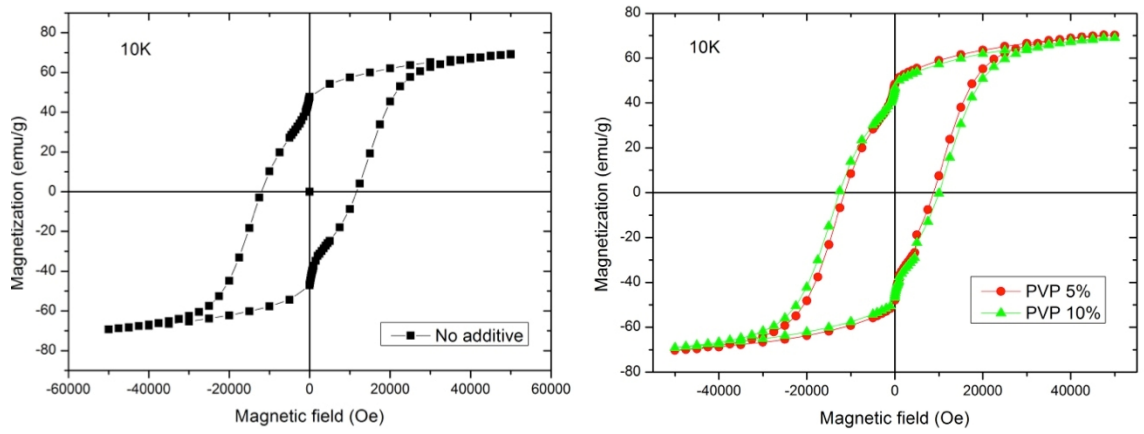

Figure 5.20 Magnetic hysteresis loops of samples prepared with and without PVP at 200 ˚C 1h.

All samples showed magnetic hysteresis loops behaviour. Besides the particle size increase with PVP addition, the saturation magnetization did not increase. Saturation magnetization did not change effectively with PVP addition, suggesting that PVP is not adsorbed on the nanoparticles surface.

The summary of characteristics of nanoparticles obtained with and without PVP at 200 °C during 1 hour.

Table 5.15 Summary table for $CoFe_2O_4$ nanoparticles prepared at 200 ºC 1h with and without PVP as additive of HS.

Additive	Nanoparticles size (nm)	Crystallite size (nm)	Ms (emu/g)	Mr (emu/g)	Hc (Oe)
None	20.1	18.2	69.1	47.7	11889
PVP5	Not measured	15.8	70.3	48.4	11346
PVP10	23.6	18.9	69	46.9	12581

5.2.4. Other studies

- ***Co^{2+} and Fe^{3+} concentration***

In order to study the effect of initial metal ions concentration, two concentrations were used: 0.1/0.2 M and 0.3/0.6 M. Figure 5.21 shows $CoFe_2O_4$ prepared by different concentrations of metal ions: 0.1/0.2 M and 0.3/0.6 M. The shape of nanoparticles does not changed with varying metal ions concentrations. Both samples show quasi-spherical and cubic nanoparticles.

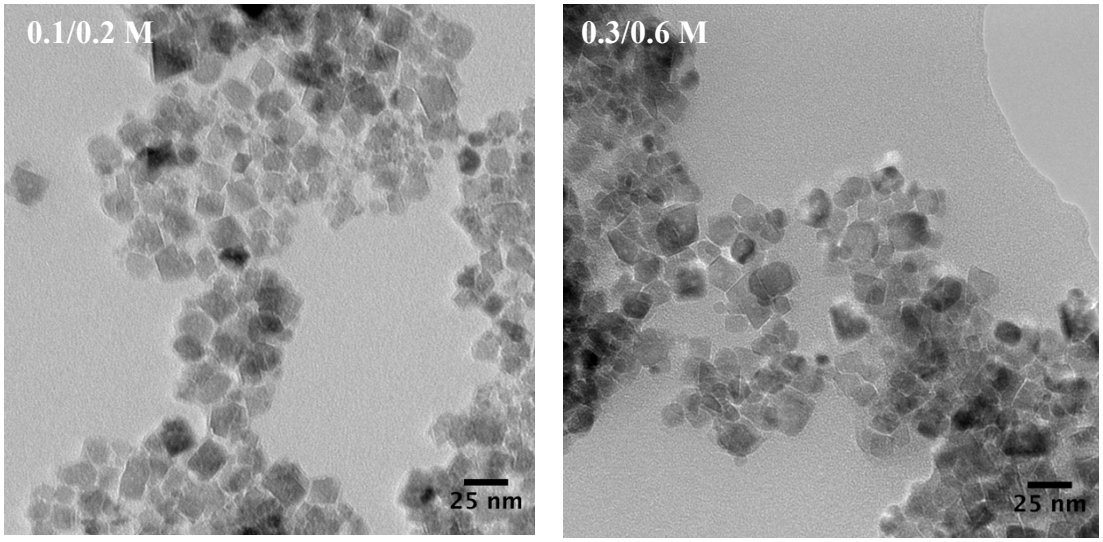

Figure 5.21 TEM micrographs of $CoFe_2O_4$ nanoparticles obtained with different molar concentrations of Co^{2+} and Fe^{3+} prepared at 230°C 1h.

The average particle size increases from 22.2 to 23.8 nm with increasing concentration (Table 5.16). A possible explanation is the availability of ionic species on the medium to promote the crystal growth.

Table 5.16 Average particle size (D_{TEM}), standard deviation (σ) and specific surface area (A_{BET}) of samples prepared with different concentrations of Co^{2+}/Fe^{3+}.

Co^{2+}/Fe^{3+}	D_{TEM} (nm)	σ (nm)	A_{BET} (m^2 g^{-1})
0.1/0.2 M	22.2	4.1	134.6
0.3/0.6 M	23.8	5.1	81.3

Figure 5.22 shows the X-ray patterns of nanoparticles prepared with different Co^{2+}/Fe^{3+} concentrations. For both samples, all peaks are indexed to $CoFe_2O_4$. No other phases were detected. Like particle size, the crystallite size increases for high concentrations due to more ionic species available for crystallite growth. The crystallite size is similar to particle size indicating that these nanoparticles are single-crystals.

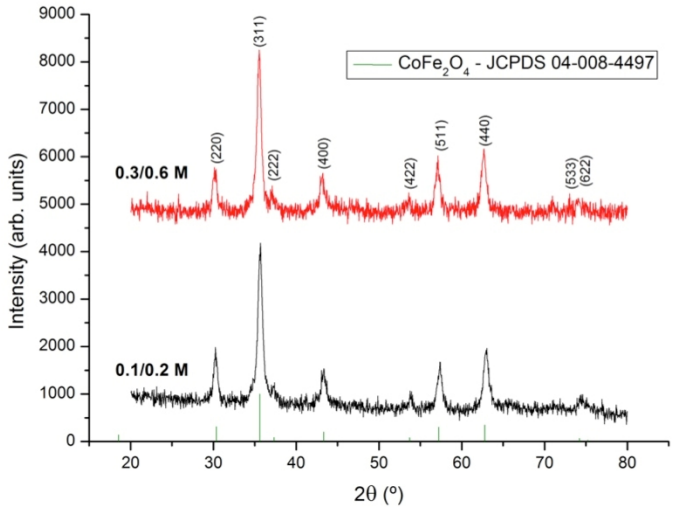

Sample	Crystallite size (nm)
0.1/0.2M	18.2
0.3/0.6 M	20.8

Figure 5.22 X-ray diffraction patterns showing the Co^{2+} and Fe^{3+} concentrations effect on crystallinity (left) and crystallite size (right) of $CoFe_2O_4$ nanoparticles.

Magnetic hysteresis loops showing the effect of Co^{2+}/Fe^{3+} on magnetic properties are presented in Figure 5.23.

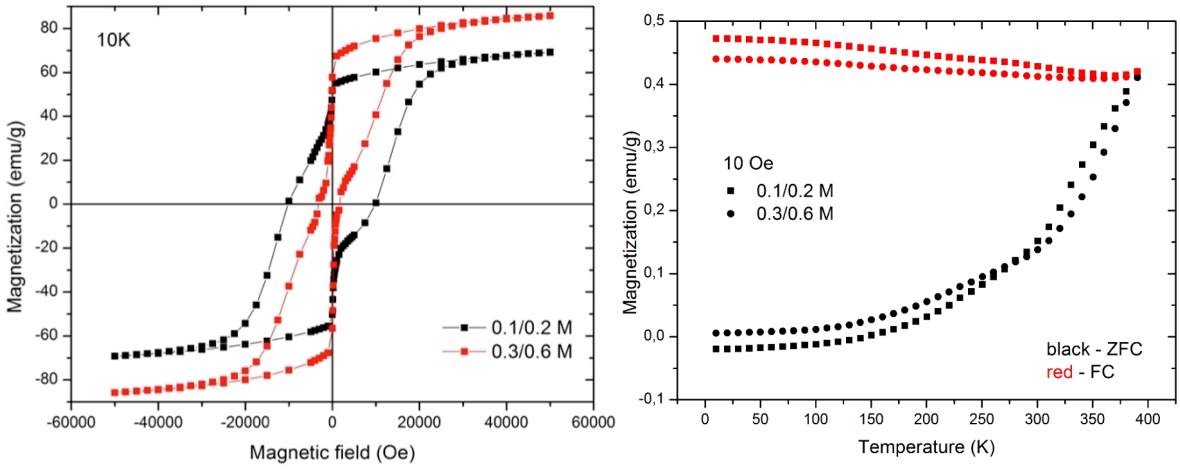

Figure 5.23 Hysteresis loops for samples prepared with different concentrations of Co^{2+}/Fe^{3+} (left) and Magnetization versus Temperature curve (right)**.**

Saturation magnetization increases from 69.1 to 85.8 emu/g with Co^{2+}/Fe^{3+} concentration increase. This high value of Ms is due to high particle size when it is compared with the other samples. The blocking temperature is around 390 °C for both samples.

Table 5.17 presents the summary of the properties of nanoparticles obtained from different concentrations of Co^{2+}/Fe^{3+} precursors.

Table 5.17 Summary table for $CoFe_2O_4$ nanoparticles prepared with different concentrations for Co^{2+}/Fe^{3+} at 230ºC 1h.

Co^{2+}/Fe^{3+}	Nanoparticles size (nm)	Crystallite size (nm)	Ms (emu/g)	Mr (emu/g)	Hc (Oe)
0.1/0.2M	22.2	18.2	69.1	51.7	10230
0.3/0.6M	23.8	20.8	85.8	57.8	3195

- ***NaOH concentration***

Figure 5.24 shows nanoparticles prepared with different concentration of base NaOH. The effect is clearly observed. High NaOH concentration induces the formation of cubic-like nanoparticles. The average size calculated by TEM measurements was 16.6 nm for nanoparticles prepared with NaOH 6 M and 22.2 nm for NaOH 10 M.

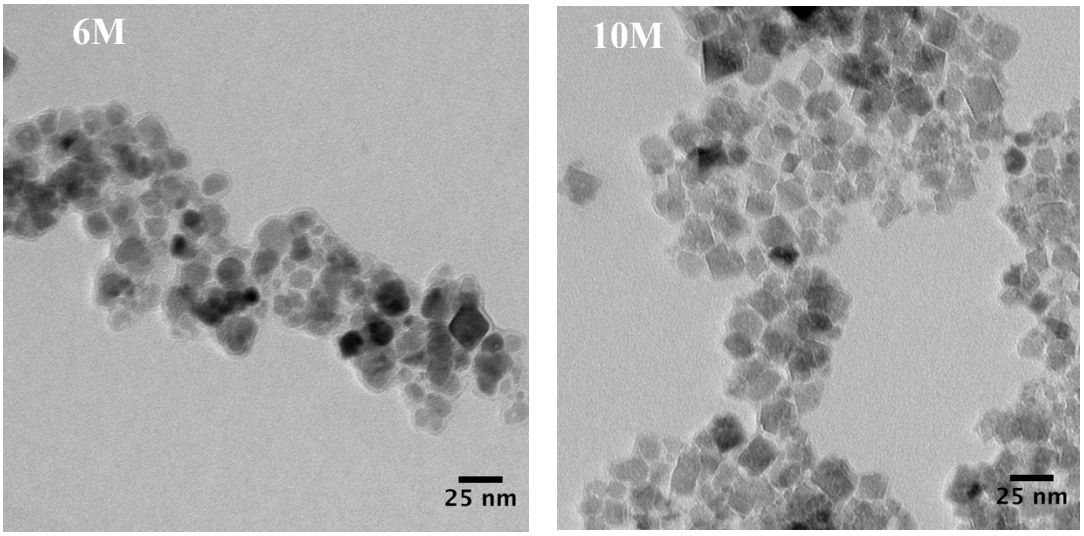

Figure 5.24 TEM micrographs of $CoFe_2O_4$ nanoparticles prepared at 230 °C for 1 h using different NaOH concentrations (6 and 10M).

Table 5.18 Average particle size D_{TEM}, standard deviation (σ) and specific surface area (A_{BET}) of samples prepared with different NaOH concentration.

NaOH concentration	D_{TEM} (nm)	σ (nm)	A_{BET} (m^2 g^{-1})
6 M	16.1	3.0	90.3
10 M	22.2	4.1	134.6

Figure 5.25 shows the XRD patterns of the nanoparticles prepared using different NaOH concentrations. The particles prepared with NaOH 6 M present on the XRD pattern of reflection peaks with low intensity indexed to hematite phase. The crystallite size increases from 16.6 to 18.2 with NaOH concentration increase. The similarities between crystallite size calculated by Scherrer equation and particle size calculated by TEM measurements indicate that the nanoparticles are single-crystals.

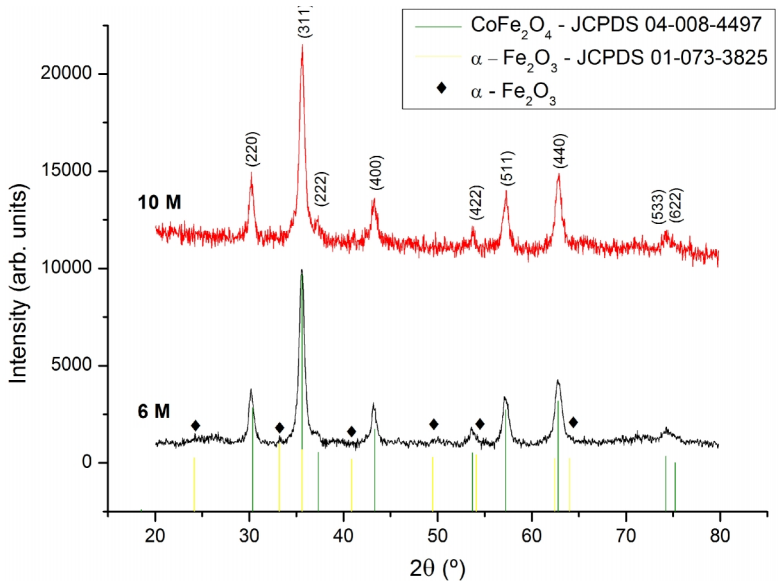

Sample	Crystallite size (nm)
6 M	16.6
10 M	18.2

Figure 5.25 X-ray diffraction patterns (left) and crystallite size (right) of $CoFe_2O_4$ nanoparticles prepared with different concentrations of NaOH.

In Figure 5.26 is shown the hysteresis loops of CFO nanoparticles prepared with different concentration of NaOH, 6 and 10 M. The presence of small amount of α-Fe_2O_3 does not influence the magnetic properties of nanoparticles prepared with NaOH 6M. The saturation magnetization is 73.2 and 69.1 emu/g for nanoparticles prepared with NaOH 6 M and 10 M, respectively.

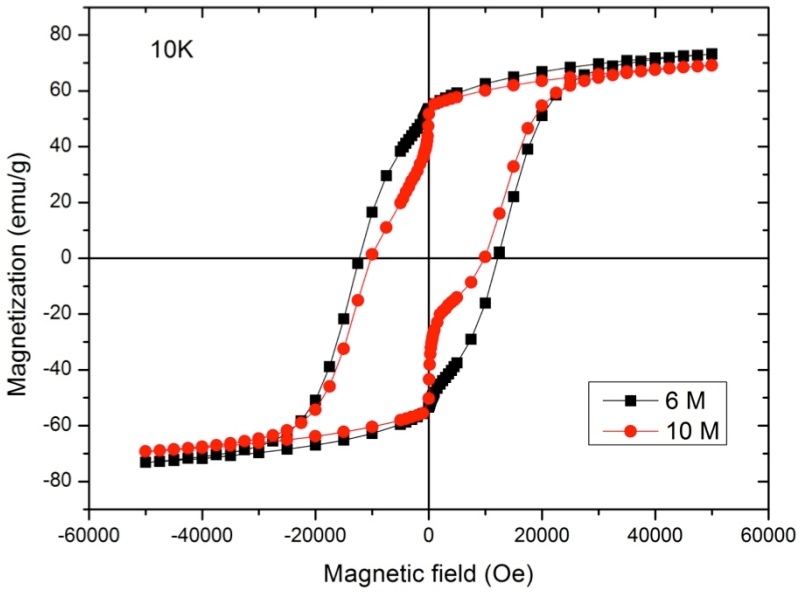

Figure 5.26 Hysteresis loops of $CoFe_2O_4$ nanoparticles prepared with different concentrations of NaOH at 230°C 1h.

The resume of characteristics of nanoparticles prepared by different concentrations of NaOH is presented in Table 5.19.

Table 5.19 Summary table for nanoparticles prepared with different concentrations of NaOH at 230ºC 1h.

NaOH concentration	Nanoparticles size (nm)	Crystallite size (nm)	Ms (emu/g)	Mr (emu/g)	Hc (Oe)
6 M	16.1	16.6	73.2	53.6	12304
10 M	22.2	18.2	69.1	51.7	10230

5.3. Films functionalization

5.3.1. Electrophoretic deposition optimization

In order to achieve a good electrophoretic deposition is important to get a stable suspension. The first step was to assess the stability of five different suspensions as a function of the time. $CoFe_2O_4$ nanoparticles used for EPD were prepared at 230 °C and 1h because, they present high crystallinity, good magnetic properties (73.2 emu/g) and small particle size (16 mm), allowing it deposition in the pores of $BaTiO_3$ thin films.

Figure 5.27 shows a qualitative study of the stability of the 5 suspensions prepared in the same conditions based on the evaluation of the visual changes. The solvents on the vials from left to right is water, ethanol, acetone, n-hexane and n-butanol. In the first 5 minutes, no changes were observed in the suspensions. After 30 minutes it could be seen that the acetone suspension shows more sedimentation than the other ones. After 120 minutes, the water and n-butanol suspensions remain practically unchanged, while ethanol and acetone are very clear indicating that the nanoparticles sediment in large extend. In the water suspension after 1500 minutes is clear the start of a gradual sedimentation. From all the solvents used as dispersant, n-hexane seems to be the one in which, after the sedimentation of the large particles (occurring in the first 30 minutes), the nanoparticles remain stable in suspension for longer times.

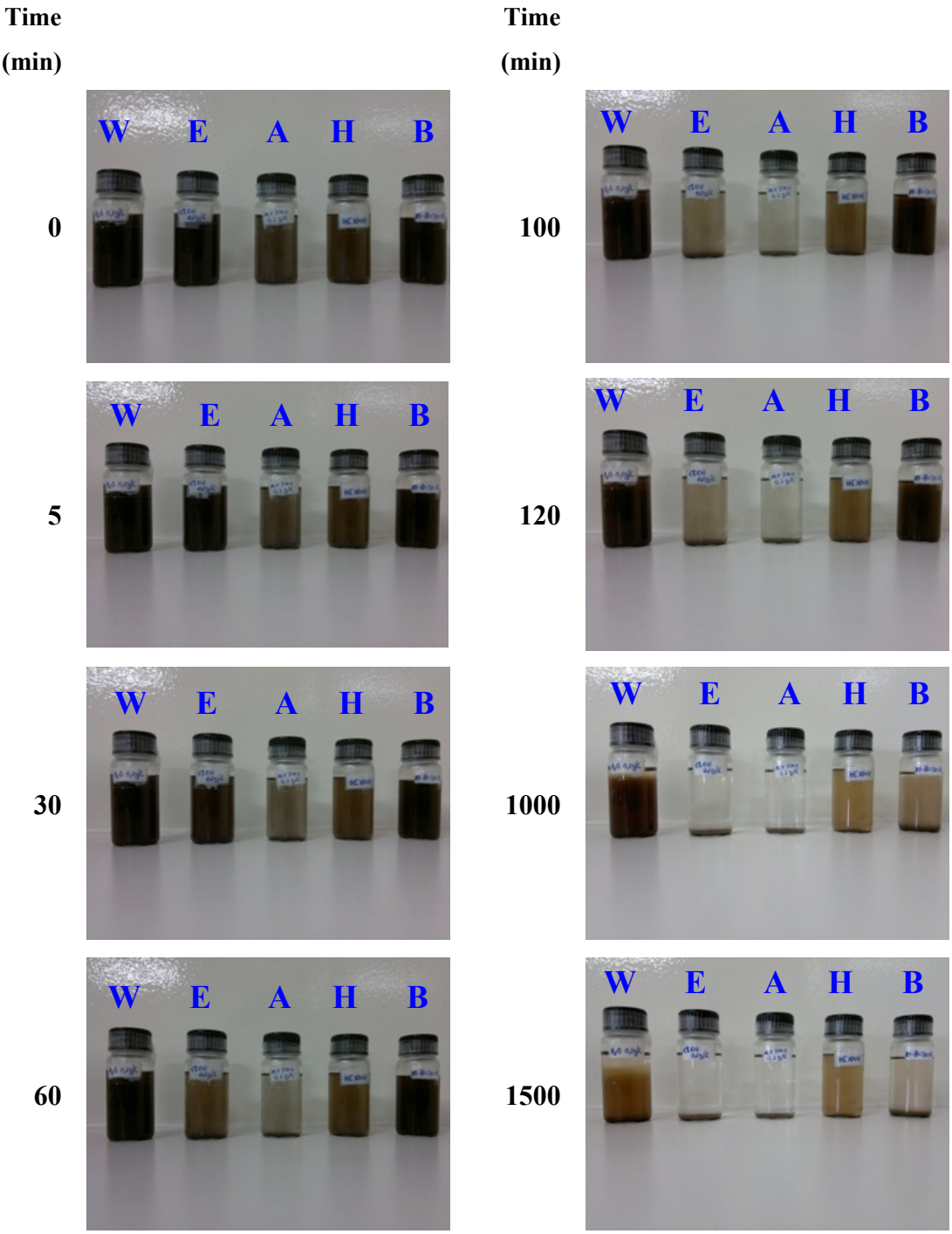

Figure 5.27 Suspensions stability studies as a function of the time (minutes).
Legend: **W** = water, **E** = ethanol, **A** = acetone, **H** = n-hexane and **B** = n-butanol.

To quantify the stability of the suspensions, in the first minutes, it was used a UV spectrometer *Shimadzu UV-3100*. Figure 5.28 shows the variation of the transmittance percentage as function of time (min) for the 5 suspensions.

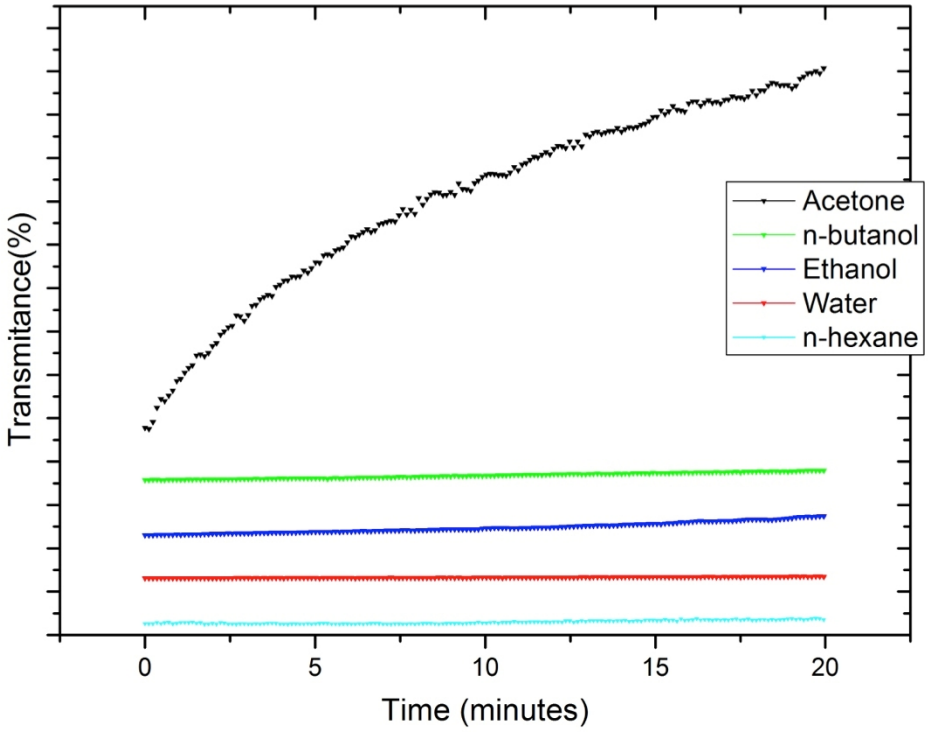

Figure 5.28 Transmittance (%) versus time (s) in order to observe the stability of different suspensions.

As observed before, the acetone suspension shows the worst stability. The best ones are water, n-hexane and n-butanol. The water suspension was not chosen because during the EPD process, when a voltage is applied some bubbles appear due to the electrolysis of water in presence of a voltage [120]. The chosen solvents for EPD optimization were n-hexane and n-butanol. Table 5.20 presents the physical properties of these two solvents important for EPD.

Table 5.20 Viscosity and dielectric constant of n-butanol [90] and n-hexane [121].

Solvent	Viscosity (cP)	Dielectric constant
n-butanol	2.6	17.5
n-hexane	0.3	1.89

At the beginning of this project, the substrates used for deposition of $BaTiO_3$ porous matrices and EPD optimization were purchased from *Inostek*. These wafers are composed with multilayer with known composition: $Pt/TiO_2/SiO_2/Si$. The thicknesses of layers are presented in Table 5.21.

Table 5.21 Composition and thickness of layers of Inostek platinized Si wafers.

Composition	Thickness (nm)
Pt	150
TiO_2	20
SiO_2	300
Si	150×10^6

The porous microstructure of the $BaTiO_3$ films was the same in *Inostek* and Ramtron substrates. However, for EPD optimization, during the deposition the peeling of first layer of *Inostek* substrate (not shown) was observed. The peeling occurs in both n-hexane and n-butanol suspensions. To further investigate what was occurring, other common dispersants were tested such as acetone and ethanol (EtOH). Citric acid (CAc) and triethanolamine (TEA) were added in order to change the suspension pH. Figure 5.29 shows the conditions used in terms of suspension composition, voltage and time (on the left) and the visual aspect of the *Inostek* substrates after deposition (on the right).

Sample	Suspension	Voltage / Time
E1	EtOH + CAc	50 V / 60 s
E2	EtOH + CAc	50 V / 15 s
E3	EtOH + TEA	20 V / 15 s
E4	Acetone + TEA	50 V / 15 s

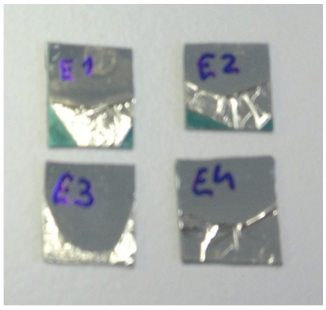

Figure 5.29 EPD conditions (left) and visual aspect of the *Inostek* substrates after deposition displaying the peeling after Pt layer.

In all cases, the *Inostek* substrate was not robust enough to be kept unchanged after use. As the *Ramtron* substrate shows better performance under the described conditions, the XRD patterns of both *Inostek* and *Ramtron* bare substrates were compared in an attempt to understand the reasons of the different behaviour (Figure 5.30). The substrates display similar XRD patterns, with the reflections peaks of SiO_2, TiO_2 and Pt. As the layers of *Ramtron* substrate measured by SEM/EDS are very similar to the specifications of the *Inostek*, one can conclude that the reasons for the peeling behaviour should be the worse quality of this substrate in comparison to the *Ramtron* with a bad adhesion of the Pt

to the layers underneath. From now on, all experiments were performed on *Ramtron* substrate.

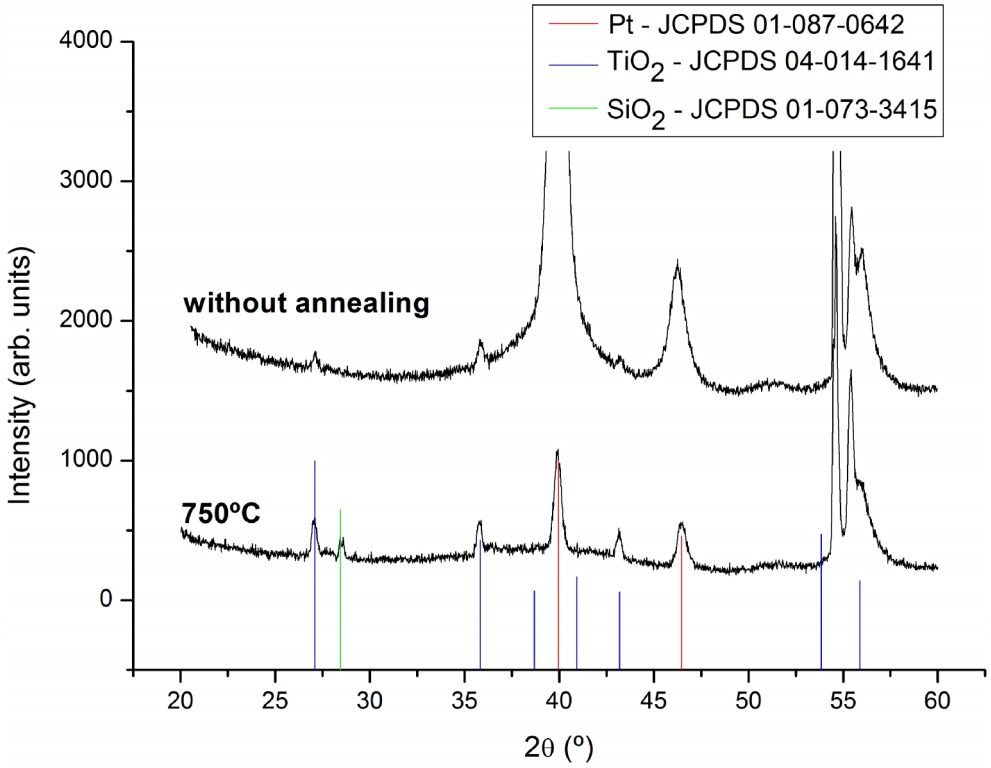

Figure 5.30 XRD patterns of *Inostek* and *Ramtron* substrates.

To optimize the EPD depositions, different voltages (250 and 500 V) and different deposition times (10, 30 and 60 s) were tested. A resume of the experiments with different voltages and times is shown in Table 5.22:

Table 5.22 Parameters of experiments for EPD optimization.

Solvent	Voltage (V)	Time (s)
n-Hexane	250	60
	250	10
	500	10
	250	30
n-Butanol	250	60
	500	30
	500	10

The results of these experiments are presented in Figure 5.31 for n-hexane suspension and Figure 5.32 for n-butanol suspension.

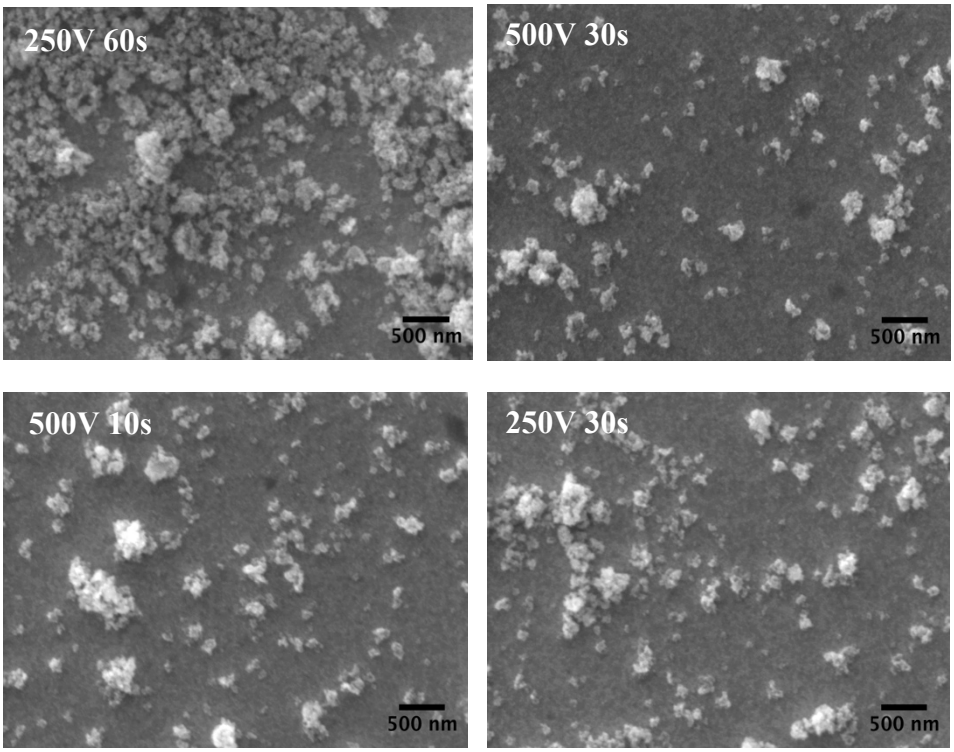

Figure 5.31 SEM micrographs of EPD optimization experiments for n-hexane suspension using different voltages (250 and 500 V) and deposition times (10, 30 and 60 s).

For the same voltage, in n-hexane medium, the amount of deposited nanoparticles increases with the deposition time. The use of 250 V allows a better control of the deposition, as the difference between different times of deposition becomes clear. There is not a big difference between the films prepared at 500 V for 10 or 30 s. For all the conditions, the deposited nanoparticles seem to be agglomerated.

For n-butanol experiments, as it can be seen in Figure 5.32, the amount of deposited nanoparticles is much lower than in the case of n-hexane suspension. This fact is related to the dielectric constant of each solvent. As the dielectric constant of the n-butanol (17.5) is quite high, a high ionic concentration is present at the solution, decreasing the mobility of the species.

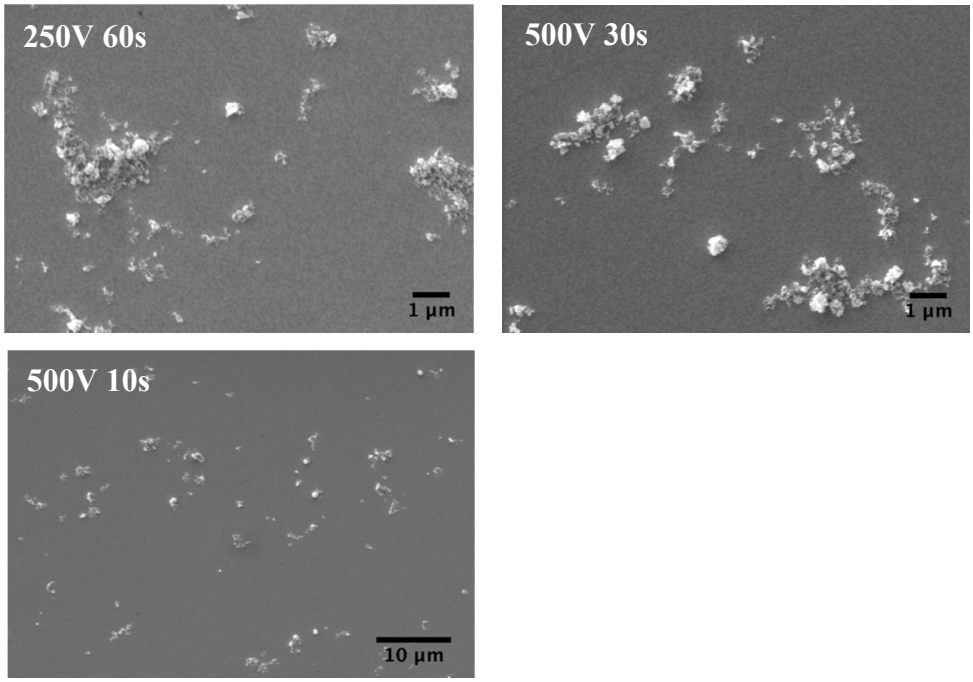

Figure 5.32 SEM micrographs of EPD optimization experiments for n-butanol suspension using 250 and 500 V and deposition times of 10, 30 and 60 s.

5.3.2. Porous $BaTiO_3$ films functionalization

To functionalize the porous $BaTiO_3$ matrices, it was used the n-hexane suspension, 250 V and 30 seconds of deposition time. The depositions were performed on the top of C8 $BaTiO_3$ film. C8 porous film was prepared using the PS-b-PEO with Mw of 58600-71000 $gmol^{-1}$. C8 presents ordered hexagonal arrangement of pores but pores sizes averaging around 29 nm. As observed in Figure 5.33, after the deposition the nanoparticles are still agglomerated. They are laying down at the top of the film. Almost no particles go into the pores.

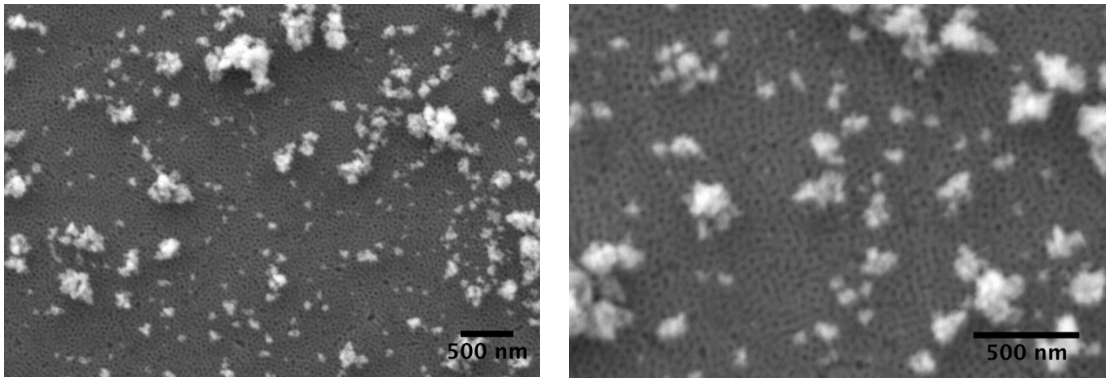

Figure 5.33 SEM micrographs of porous $BaTiO_3$ thin films with $CoFe_2O_4$ nanoparticles (250V 30s).

For further optimization of the electrophoretic mobility of species on n-butanol suspensions a small amount of 0.6 mM iodine was added to the suspension. This time it was chosen in order to functionalise the porous $BaTiO_3$ thin film C1 as-prepared with the block co-polymer with Mw of 40000-53000 $gmol^{-1}$. Although the microstructure of C1 is not so ordered as the one of C8, the pore size is larger (~61 nm) which may facilitate the deposition. In Figure 5.34 is presented the functionalized C1 porous film, using a voltage of 100 V and 1 minute of deposition time.

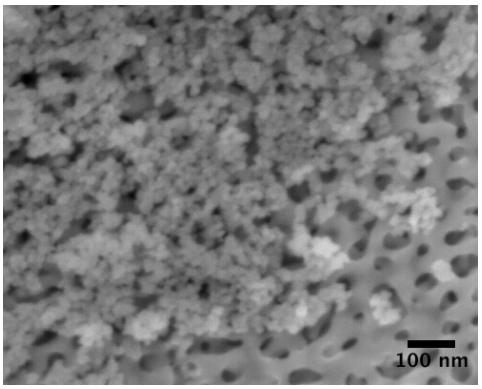

Figure 5.34 Functionalization with suspension n-butanol + iodine (0.6mM) 100V 60s.

It was observed that, effectively large and less ordered pores facilitate the functionalization. A possible explanation for this behaviour can be besides the large pore, which can accommodate easily one or more ferromagnetic particle, a better connectivity with the conductive substrate. By adding 0.6 mM of iodine, the amount of deposited nanoparticles was increased even with low voltage.

Conclusions And Future work

6. Conclusions and future work

6.1. Ferroelectric thin films

Porous $BaTiO_3$ films were successfully obtained by combining two methodologies: evaporation induced self-assembly and dip-coating. The effect of type of annealing, Mw of block copolymer and polymer concentration was observed. The annealing type (with or without ramp) does not influence the microstructure of porous thin films. The copolymer with higher molecular weight permits the pores organization and creates smaller pores. Further studies need to be done to understand the formation of small pores using block co-polymer with molecular weight (58600-71000). High concentrations of block co-polymer PS-b-PEO lead to formation of interconnected pores due to high pore density. The thickness of porous $BaTiO_3$ thin films decreases with annealing temperature due to the crystallization of material. The film thickness also depends on withdrawal speed since high speeds form thick films.

For a more complete study of ferroelectric porous thin films, a series of tasks and further characterizations must be taken into consideration. Principally, a controlled correlation between porosity magnitudes with the film thickness, will diminish topography deformation, increase polarization and therefore induce topography – piezoresponse information independence and allow a successful polarization hysteresis loop measurement. In addition, an indispensable evidence for the piezoelectric character in materials is the switching of the ferroelectric domains, by the application of DC bias voltage. Changing by positive to negative voltage application direction, the domains are reoriented respectively. Last but not least, an optimization of the combination between the technical characteristics of the cantilever tip (geometry, spring constant, resonant frequency), the applied voltage amplitude and the frequency is necessary for noise minimization.

These porous matrices are a good candidate for pyroelectric and multifunctional applications due to porous microstructure.

The preparation of dense films in the same conditions as porous films (withdrawal speed, molecular weight and concentration of co-polymer) are suggested in order to study the effect of porosity on dielectric constant and ferroelectric properties. The effect of block co-polymer concentration could affect the thickness of porous thin films, therefore studies on this directions need to be done.

6.2. Hydrothermal synthesis

The effect of various parameters on HS of $CoFe_2O_4$ nanoparticles was successfully studied. For the temperature of HS effect, it can be concluded that the crystallite size increases for temperatures between 100 and 150˚C, but above this temperature, the particle size decreases due to a fast nucleation and reduction of available precursors in solution avoiding their growth. The magnetic properties increase with temperature of HS due to the high crystallinity of samples synthesized at higher temperatures. At low HS temperature it was verified a drop of the magnetization at 0 Oe field which indicates the presence of a soft magnetic impurity. The samples prepared at 230°C 3h and 24h show the presence of hematite phase which impairs the magnetic properties due to the presence of a antiferromagnetic phase, hematite. The effect of PVP addition was studied. PVP addition does not influence the shape of nanoparticles, however promotes the nanoparticles growth. The crystallite size increases with the PVP addition, which did not acts as capping agent. The crystallinity and magnetic properties were not affected by PVP addition. The concentration of Co^{2+}/Fe^{3+} does not influence the shape of nanoparticles. However, the crystallite size increases for higher concentration due to the presence of more available precursors of crystal growth. Nanoparticles prepared with high concentration of Co^{2+}/Fe^{3+} show the higher saturation magnetization measured at 10 K, 85.6 emu/g, and low coercive field (3195 Oe) meaning that this material easily achieves saturation magnetization and easily this Ms could be withdrawn. The concentration of NaOH influences the nanoparticles shape and size. For higher concentrations nanoparticles show rhomb shape and the crystallite size is higher. The nanoparticles prepared with low concentration of NaOH (6M) showed the presence of an antiferromagnetic phase (hematite). However, it is in small weight and did not influence the magnetic properties.

Studies of effect of PVP for longer times of hydrothermal synthesis would be interesting to be done. A heating rate during the hydrothermal synthesis could avoid the rapid nucleation of nanoparticles, reducing their sizes. Lower concentrations than 6 M of NaOH should be used in hydrothermal synthesis in order to understand the formation of hematite phase.

6.3. Functionalization by EPD

The effect of stability of different suspensions for EPD was observed. Voltage and time of deposition effects were studied in order to optimize the electrophoretic deposition of $CoFe_2O_4$ nanoparticles.

The chemical and physical stability of substrates is a very important key to take into account.

EPD is a good candidate to functionalize porous $BaTiO_3$ thin films however, the deposition of nanoparticles does not occur in the pores of $BaTiO_3$ thin films as desired due to an agglomeration of nanoparticles. More studies need to be done in order to disperse $CoFe_2O_4$ nanoparticles and get a successful EPD.

7. Final notes

This thesis allowed to get significant knowledge about ferroelectric, ferromagnetic and multiferroic materials, which was not acquired during the Master in Engineering Materials curricular activities. New methods for synthesis of thin films and magnetic nanoparticles were learned. The properties of final products could be easily manipulated by changing some process parameters.

References

8. References

[1] (September 2012). *Old computer*. Available: http://t3.gstatic.com/images?q=tbn:ANd9GcQYdG1ttZLF7Jgasl7QNhwdx87QV04lrKjBuFkbrEmniFKy06i-Eh8-k_OGJQ

[2] (September 2012). *Macbook Air*. Available: http://cdn0.sempretops.com/wp-content/uploads/Apple.jpg

[3] G. E. Moore, "Cramming more components onto integrated circuits", *Proceedings of the Ieee,* vol. 38, pp. 114-117, 1965.

[4] W. Kleemann, "Switching magnetism with electric fields", *Physics,* vol. 2, 2009.

[5] L. W. Martin and R. Ramesh, "Multiferroic and magnetoelectric heterostructures", *Acta Materialia,* vol. 60, pp. 2449-2470, 2012.

[6] C. Ederer and N. A. Spaldin, "Weak ferromagnetism and magnetoelectric coupling in bismuth ferrite", *Physical Review B,* vol. 71, 2005.

[7] H. Zheng, J. Wang, S. E. Lofland, Z. Ma, L. Mohaddes-Ardabili, T. Zhao, L. Salamanca-Riba, S. R. Shinde, S. B. Ogale, F. Bai, D. Viehland, Y. Jia, D. G. Schlom, M. Wuttig, A. Roytburd, and R. Ramesh, "Multiferroic $BaTiO_3$-$CoFe_2O_4$ Nanostructures", *Science,* vol. 303, pp. 661-663, 2004.

[8] K. Aizu, "Possible Species of Ferromagnetic, Ferroelectric, and Ferroelastic Crystals", *Physical Review B,* vol. 2, pp. 754-772, 1970.

[9] W. Eerenstein, N. D. Mathur, and J. F. Scott, "Multiferroic and magnetoelectric materials", *Nature,* vol. 442, pp. 759-765, 2006.

[10] Y. Wang, J. M. Hu, Y. H. Lin, and C. W. Nan, "Multiferroic magnetoelectric composite nanostructures", *Npg Asia Materials,* vol. 2, pp. 61-68, 2010.

[11] N. Setter, D. Damjanovic, L. Eng, G. Fox, S. Gevorgian, S. Hong, A. Kingon, H. Kohlstedt, N. Y. Park, G. B. Stephenson, I. Stolitchnov, A. K. Taganstev, D. V. Taylor, T. Yamada, and S. Streiffer, "Ferroelectric thin films: Review of materials, properties, and applications", *Journal of Applied Physics,* vol. 100, 2006.

[12] K. M. Rabe, C. H. Ahn, and J.-M. Triscone, *Physisc of Ferroelectrics - A Modern Perspective*: Springer, 2007.

[13] P. Ferreira, R. Z. Hou, A. Wu, M.-G. Willinger, P. M. Vilarinho, J. Mosa, C. Laberty-Robert, C. Boissière, D. Grosso, and C. Sanchez, "Nanoporous Piezo- and Ferroelectric Thin Films", *Langmuir,* vol. 28, pp. 2944 - 2949, 2012.

[14] D. D. Fong, G. B. Stephenson, S. K. Streiffer, J. A. Eastman, O. Auciello, P. H. Fuoss, and C. Thompson, "Ferroelectricity in ultrathin perovskite films", *Science,* vol. 304, pp. 1650-1653, 2004.

[15] G. A. Smolenskii, V. A. Bokov, V. A. Isupov, N. N. Krainik, R. E. Pasynkov, and A. I. Sokolov, *Ferroelectrics and related materials*, 1984.

[16] (September 2012). *Image adapted from*: http://ferroeletricos.com

[17] (April 2012). *Image adapted from*: http://mrc.iisc.ernet.in/Images/Research_Areas/Original/Image1_Perovskite.jpg

[18] (September 2012). *Image adapted from*: http://www.piceramic.com/piezo_effect.php

[19] M. E. Lines and A. M.Glass, *Principles and applications of Ferroelectrics and Related Materials*: Oxford, 1977.
[20] R. A. McCurrie, *Ferromagnetic Materials - Structure and Properties*: Academic Press, 1994.
[21] W. D. Callister, *Fundamentals of Materials Science and Engineering*, 5 ed.: John Wiley & Sons, 2001.
[22] R. S. Tebble and D. J. Craik, *Magnetic Materials*: Wiley-Interscience, 1969.
[23] J. Wang, J. B. Neaton, H. Zheng, V. Nagarajan, S. B. Ogale, B. Liu, D. Viehland, V. Vaithyanathan, D. G. Schlom, U. V. Waghmare, N. A. Spaldin, K. M. Rabe, M. Wuttig, and R. Ramesh, "Epitaxial $BiFeO_3$ multiferroic thin film heterostructures", *Science,* vol. 299, pp. 1719-1722, 2003.
[24] R. Ramesh and N. A. Spaldin, "Multiferroics: progress and prospects in thin films", *Nature Materials,* vol. 6, pp. 21-29, 2007.
[25] P. M. Rorvik, T. Grande, and M. A. Einarsrud, "One-Dimensional Nanostructures of Ferroelectric Perovskites", *Advanced Materials,* vol. 23, pp. 4007-4034, 2011.
[26] H. Jeen, G. Singh-Bhalla, P. R. Mickel, K. Voigt, C. Morien, S. Tongay, A. F. Hebard, and A. Biswas, "Growth and characterization of multiferroic $BiMnO_3$ thin films", *Journal of Applied Physics,* vol. 109, pp. 1-5, 2011.
[27] J. Y. Son, B. G. Kim, C. H. Kim, and J. H. Cho, "Writing polarization bits on the multiferroic $BiMnO_3$ thin film using Kelvin probe force microscope", *Applied Physics Letters,* vol. 84, pp. 4971-4973, 2004.
[28] J. Y. Son, C. S. Park, and H. Kim, "Room temperature ferroelectric property of $BiMnO_3$ thin film with double $SrTiO_3$ buffer layers on $Pt/Ti/SiO_2/Si$ substrate", *Metals and Materials International,* vol. 16, pp. 289-292, 2010.
[29] N. A. Hill, "Why are there so few magnetic ferroelectrics?", *Journal of Physical Chemistry B,* vol. 104, pp. 6694-6709, 2000.
[30] F. Jimenez-Villacorta, J. A. Gallastegui, I. Fina, X. Marti, and J. Fontcuberta, "Strain-driven transition from E-type to A-type magnetic order in $YMnO_3$ epitaxial films", *Physical Review B,* vol. 86, pp. 1-4, 2012.
[31] L. Martin, S. P. Crane, Y. H. Chu, M. B. Holcomb, M. Gajek, M. Huijben, C. H. Yang, N. Balke, and R. Ramesh, "Multiferroics and magnetoelectrics: thin films and nanostructures", *Journal of Physics-Condensed Matter,* vol. 20, 1-14 2008.
[32] E. Aksel and J. L. Jones, "Advances in Lead-Free Piezoelectric Materials for Sensors and Actuators", *Sensors,* vol. 10, pp. 1935-1954, 2010.
[33] Y. H. Chu, L. W. Martin, M. B. Holcomb, and R. Ramesh, "Controlling magnetism with multiferroics", *Materials Today,* vol. 10, pp. 16-23, 2007.
[34] T. Moriya, "Anisotropic Superexchange Interaction and Weak Ferromagnetism", *Physical Review,* vol. 120, pp. 91-98, 1960.
[35] J. R. Teague, R. Gerson, and W. J. James, "Dielectric Hysteresis in Single Crystal $BiFeO_3$", *Solid State Communications,* vol. 8, pp. 1073-1074, 1970.
[36] J. B. Neaton, C. Ederer, U. V. Waghmare, N. A. Spaldin, and K. M. Rabe, "First-principles study of spontaneous polarization in multiferroic $BiFeO_3$", *Physical Review B,* vol. 71, pp. 1-8, 2005.

[37] L. E. Cross, *Nanocomposites for electronic applications* vol. I: Pennstate University, 1991.

[38] V. Suchtelen, "Product Properties - New Application of Composite-Materials", *Philips Research Reports,* vol. 27, p. 28, 1972.

[39] C. W. Nan, "Magnetoelectric Effect in Composites of Piezoelectric and Piezomagnetic Phases", *Physical Review B,* vol. 50, pp. 6082-6088, 1994.

[40] J. Ryu, A. V. Carazo, K. Uchino, and H. E. Kim, "Magnetoelectric properties in piezoelectric and magnetostrictive laminate composites", *Japanese Journal of Applied Physics Part 1-Regular Papers Short Notes & Review Papers,* vol. 40, pp. 4948-4951, 2001.

[41] J. Wang, Y. Zhang, J. Ma, Y. Lin, and C. W. Nan, "Magnetoelectric behavior of $BaTiO_3$ films directly grown on $CoFe_2O_4$ ceramics", vol. 104, pp. 1-5, 2008.

[42] Y. Zhang, C. Y. Deng, J. Ma, Y. H. Lin, and C. W. Nan, "Enhancement in magnetoelectric response in $CoFe_2O_4$-$BaTiO_3$ heterostructure", *Applied Physics Letters,* vol. 92, pp. 1-3, 2008.

[43] F. Zavaliche, H. Zheng, L. Mohaddes-Ardabili, S. Y. Yang, Q. Zhan, P. Shafer, E. Reilly, R. Chopdekar, Y. Jia, P. Wright, D. G. Schlom, Y. Suzuki, and R. Ramesh, "Electric field-induced magnetization switching in epitaxial columnar nanostructures", *Nano Letters,* vol. 5, pp. 1793-1796, 2005.

[44] L. Yan, Z. G. Wang, Z. P. Xing, J. F. Li, and D. Viehland, "Magnetoelectric and multiferroic properties of variously oriented epitaxial $BiFeO_3$-$CoFe_2O_4$ nanostructured thin films", *Journal of Applied Physics,* vol. 107, pp. 1-6, 2010.

[45] C. T. Kresge, M. E. Leonowicz, W. J. Roth, J. C. Vartuli, and J. S. Beck, "Ordered Mesoporous Molecular-Sieves Synthesized by a Liquid-Crystal Template Mechanism", *Nature,* vol. 359, pp. 710-712, 1992.

[46] D. Grosso, C. Boissière, L. Nicole, and C. Sanchez, "Preparation, treatment and characterisation of nanocrystalline mesoporous ordered layers", *Journal of Sol-Gel Science and Technology,* vol. 40, pp. 141-154, 2006.

[47] D. Grosso, C. Boissiere, B. Smarsly, T. Brezesinski, N. Pinna, P. A. Albouy, H. Amenitsch, M. Antonietti, and C. Sanchez, "Periodically ordered nanoscale islands and mesoporous films composed of nanocrystalline multimetallic oxides", *Nature Materials,* vol. 3, pp. 787-792, 2004.

[48] V. Stancu, M. Lisca, I. Boerasu, L. Pintilie, and M. Kosec, "Effects of porosity on ferroelectric properties of $Pb(Zr_{0.2}Ti_{0.8})O_3$ films", *Thin Solid Films,* vol. 515, pp. 6557-6561, 2007.

[49] G. Suyal and N. Setter, "Enhanced performance of pyroelectric microsensors through the introduction of nanoporosity", *Journal of the European Ceramic Society,* vol. 24, pp. 247-251, 2004.

[50] N. Setter, D. Damjanovic, L. Eng, G. Fox, S. Gevorgian, S. Hong, A. Kingon, H. Kohlstedt, N. Y. Park, G. B. Stephenson, I. Stolitchnov, A. K. Taganstev, D. V. Taylor, T. Yamada, and S. Streiffer, "Ferroelectric thin films: Review of materials, properties, and applications", *Journal of Applied Physics,* vol. 100, pp. 1-46, 2006.

[51] C. Sanchez, C. Boissiere, D. Grosso, C. Laberty, and L. Nicole, "Design, synthesis, and properties of inorganic and hybrid thin films having periodically organized nanoporosity", *Chemistry of Materials,* vol. 20, pp. 682-737, 2008.

[52] V. Stancu, I. Boerasu, M. Lisca, L. Pintilie, M. Popescu, and F. Sava, "Structural and microstructural properties of porous PZT films", *Journal of Optoelectronics and Advanced Materials,* vol. 8, pp. 1492-1497, 2006.

[53] A. Fisher, M. Kuemmel, M. Jarn, M. Linden, C. Boissiere, L. Nicole, C. Sanchez, and D. Grosso, "Surface nanopatterning by organic/inorganic self-local assembly and selective local functionalization", *Small,* vol. 2, pp. 569-574, 2006.

[54] M. Faustini, B. Louis, P. A. Albouy, M. Kuemmel, and D. Grosso, "Preparation of Sol-Gel Films by Dip-Coating in Extreme Conditions", *Journal of Physical Chemistry C,* vol. 114, pp. 7637-7645, 2010.

[55] A.-H. Lu, E. L. Salabas, and F. Schueth, "Magnetic nanoparticles: Synthesis, protection, functionalization, and application", *Angewandte Chemie-International Edition,* vol. 46, pp. 1222-1244, 2007.

[56] A. Hutten, D. Sudfeld, I. Ennen, G. Reiss, W. Hachmann, U. Heinzmann, K. Wojczykowski, P. Jutzi, W. Saikaly, and G. Thomas, "New magnetic nanoparticles for biotechnology", *Journal of Biotechnology,* vol. 112, pp. 47-63, 2004.

[57] D. L. LesliePelecky and R. D. Rieke, "Magnetic properties of nanostructured materials", *Chemistry of Materials,* vol. 8, pp. 1770-1783, 1996.

[58] D. Zhao, X. Wu, H. Guan, and E. Han, "Study on supercritical hydrothermal synthesis of $CoFe_2O_4$ nanoparticles", *Journal of Supercritical Fluids,* vol. 42, pp. 226-233, 2007.

[59] Y. Zhang, Z. Yang, D. Yin, Y. Liu, C. Fei, R. Xiong, J. Shi, and G. Yan, "Composition and magnetic properties of cobalt ferrite nano-particles prepared by the co-precipitation method", *Journal of Magnetism and Magnetic Materials,* vol. 322, pp. 3470-3475, 2010.

[60] K. Maaz, A. Mumtaz, S. K. Hasanain, and A. Ceylan, "Synthesis and magnetic properties of cobalt ferrite ($CoFe_2O_4$) nanoparticles prepared by wet chemical route", *Journal of Magnetism and Magnetic Materials,* vol. 308, pp. 289-295, 2007.

[61] L. I. Cabrera, A. Somoza, J. F. Marco, C. J. Serna, and M. Puerto Morales, "Synthesis and surface modification of uniform MFe_2O_4 (M = Fe, Mn, and Co) nanoparticles with tunable sizes and functionalities", *Journal of Nanoparticle Research,* vol. 14, pp. 1-14, 2012.

[62] R.-R. Gao, Y. Zhang, W. Yu, R. Xiong, and J. Shi, "Superparamagnetism and spin-glass like state for the $MnFe_2O_4$ nano-particles synthesized by the thermal decomposition method", *Journal of Magnetism and Magnetic Materials,* vol. 324, pp. 2534-2538, 2012.

[63] M. G. Naseri, E. B. Saion, M. Hashim, A. H. Shaari, and H. A. Ahangar, "Synthesis and characterization of zinc ferrite nanoparticles by a thermal treatment method", *Solid State Communications,* vol. 151, pp. 1031-1035, 2011.

[64] M. M. Husein and N. N. Nassar, "Nanoparticle Preparation Using the Single Microemulsions Scheme", *Current Nanoscience,* vol. 4, pp. 370-380, 2008.

[65] D. Langevin, "Micelles and Microemulsions", *Annual Review of Physical Chemistry,* vol. 43, pp. 341-369, 1992.

[66] M. A. Lopez-Quintela, "Synthesis of nanomaterials in microemulsions: formation mechanisms and growth control", *Current Opinion in Colloid & Interface Science,* vol. 8, pp. 137-144, 2003.

[67] M. A. Malik, M. Y. Wani, and M. A. Hashim, "Microemulsion method: A novel route to synthesize organic and inorganic nanomaterials", *Arabian Journal of Chemistry,* vol. 5, pp. 397-417, 2012.

[68] C. Liu, A. J. Rondinone, and Z. J. Zhang, "Synthesis of magnetic spinel ferrite $CoFe_2O_4$ nanoparticles from ferric salt and characterization of the size-dependent superparamagnetic properties", *Pure and Applied Chemistry,* vol. 72, pp. 37-45, 2000.

[69] K. Byrappa and T. Adschiri, "Hydrothermal technology for nanotechnology", *Progress in Crystal Growth and Characterization of Materials,* vol. 53, pp. 117-166, 2007.

[70] C. Vazquez-Vazquez, M. A. Lopez-Quintela, M. C. Bujan-Nunez, and J. Rivas, "Finite size and surface effects on the magnetic properties of cobalt ferrite nanoparticles", *Journal of Nanoparticle Research,* vol. 13, pp. 1663-1676, 2011.

[71] C. Vazquez-Vazquez, M. Lovelle, C. Mateo, M. A. Loez-Quintela, M. C. Bujan-Nunez, D. Serantes, D. Baldomir, and J. Rivas, "Magnetocaloric effect and size-dependent study of the magnetic properties of cobalt ferrite nanoparticles prepared by solvothermal synthesis", *Physica Status Solidi a-Applications and Materials Science,* vol. 205, pp. 1358-1362, 2008.

[72] L. J. Cote, A. S. Teja, A. P. Wilkinson, and Z. J. Zhang, "Continuous hydrothermal synthesis of $CoFe_2O_4$ nanoparticles", *Fluid Phase Equilibria,* vol. 210, pp. 307-317, 2003.

[73] S. C. Goh, C. H. Chia, S. Zakaria, M. Yusoff, C. Y. Haw, S. Ahmadi, N. M. Huang, and H. N. Lim, "Hydrothermal preparation of high saturation magnetization and coercivity cobalt ferrite nanocrystals without subsequent calcination", *Materials Chemistry and Physics,* vol. 120, pp. 31-35, 2010.

[74] X. M. Liu, S. Y. Fu, and L. P. Zhu, "High-yield synthesis and characterization of monodisperse sub-microsized $CoFe_2O_4$ octahedra", *Journal of Solid State Chemistry,* vol. 180, pp. 461-466, 2007.

[75] Q. Liu, J. Sun, H. Long, X. Sun, X. Zhong, and Z. Xu, "Hydrothermal synthesis of $CoFe_2O_4$ nanoplateles and nanoparticles", *Materials Chemistry and Physics,* vol. 108, pp. 269 - 273, 2008.

[76] X. X. Xiao, K. L. Huang, J. H. Yan, and Q. Q. He, "Synthesis and characterization of $CoFe_2O_4$ nanoparticles", *Transactions of Nonferrous Metals Society of China,* vol. 15, pp. 1172-1177, 2005.

[77] M. M. El-Okr, M. A. Salem, M. S. Salim, R. M. El-Okr, M. Ashoush, and H. M. Talaat, "Synthesis of cobalt ferrite nano-particles and their magnetic characterization", *Journal of Magnetism and Magnetic Materials,* vol. 323, pp. 920-926, 2011.

[78] G. B. Ji, S. L. Tang, S. K. Ren, F. M. Zhang, B. X. Gu, and Y. W. Du, "Simplified synthesis of single-crystalline magnetic $CoFe_2O_4$ nanorods by a surfactant-assisted hydrothermal process", *Journal of Crystal Growth,* vol. 270, pp. 156-161, 2004.

[79] Z. T. Chen and L. Gao, "Synthesis and magnetic properties of $CoFe_2O_4$ nanoparticles by using PEG as surfactant additive", *Materials Science and Engineering B-Solid State Materials for Advanced Technology,* vol. 141, pp. 82-86, 2007.

[80] Y. Zhang, Y. Liu, Z. Yang, R. Xiong, and J. Shi, "Synthesis of $CoFe_2O_4$ nanoparticles with tunable magnetism by the modified hydrothermal method", *Journal of Nanoparticle Research,* vol. 13, pp. 4557-4563, 2011.

[81] X. H. Li, C. L. Xu, X. H. Han, L. Qiao, T. Wang, and F. S. Li, "Synthesis and Magnetic Properties of Nearly Monodisperse $CoFe_2O_4$ Nanoparticles Through a Simple Hydrothermal Condition", *Nanoscale Research Letters,* vol. 5, pp. 1039-1044, 2010.

[82] A. R. Boccaccini and I. Zhitomirsky, "Application of electrophoretic and electrolytic deposition techniques in ceramics processing", *Current Opinion in Solid State & Materials Science,* vol. 6, pp. 251-260, 2002.

[83] S. Bonnas, H.-J. Ritzhaupt-Kleissl, and J. Haußelt, "Electrophoretic deposition for fabrication of ceramic microparts", *Journal of the European Ceramic Society,* vol. 30, pp. 1159-1162, 2010.

[84] I. Corni, M. P. Ryan, and A. R. Boccaccini, "Electrophoretic deposition: From traditional ceramics to nanotechnology", *Journal of the European Ceramic Society,* vol. 28, pp. 1353-1367, 2008.

[85] A. R. Boccaccini, J. A. Roether, B. J. C. Thomas, M. S. P. Shaffer, E. Chavez, E. Stoll, and E. J. Minay, "The electrophoretic deposition of inorganic nanoscaled materials", *Journal of the Ceramic Society of Japan,* vol. 114, pp. 1-14, 2006.

[86] I. Gonzalo-Juan, A. J. Krejci, and J. H. Dickerson, "Toward Dynamic Control over TiO_2 Nanocrystal Monolayer-by-Monolayer Film Formation by Electrophoretic Deposition in Nonpolar Solvents", *Langmuir,* vol. 28, pp. 5295-5301, 2012.

[87] A. J. Krejci, I. Gonzalo-Juan, and J. H. Dickerson, "Evolution of Ordering in Iron Oxide Nanoparticle Monolayers Using Electrophoretic Deposition", *Acs Applied Materials & Interfaces,* vol. 3, pp. 3611-3615, 2011.

[88] A. J. Krejci, J. Mandal, and J. H. Dickerson, "Patterned substrates to facilitate long-range ordering in the formation of nanoparticle monolayers by electrophoretic deposition", *Applied Physics Letters,* vol. 101, 2012.

[89] A. Y. Wu, P. M. Vilarinho, and A. I. Kingon, "Electrophoretic deposition of lead zirconate titanate films on metal foils for embedded components", *Journal of the American Ceramic Society,* vol. 89, pp. 575-581, 2006.

[90] L. Besra and M. Liu, "A review on fundamentals and applications of electrophoretic deposition (EPD)", *Progress in Materials Science,* vol. 52, pp. 1-61, 2007.

[91] H. C. Hamaker, "Formation of a deposit by electrophoresis", *Transactions of the Faraday Society,* vol. 35, pp. 0279-0286, 1940.

[92] L. Kreethawate, S. Larpkiattaworn, S. Jiemsirilers, L. Besra, and T. Uchikoshi, "Application of electrophoretic deposition for inner surface coating of porous ceramic tubes", *Surface & Coatings Technology,* vol. 205, pp. 1922-1928, 2010.

[93] R. F. Louh and Y. H. Hsu, "Fabrication of barium titanate ferroelectric layers by electrophoretic deposition technique", *Materials Chemistry and Physics,* vol. 79, pp. 226-229, 2003.

[94] S. Put, J. Vleugels, G. Anne, and O. Van der Biest, "Functionally graded ceramic and ceramic-metal composites shaped by electrophoretic deposition", *Colloids and Surfaces a-Physicochemical and Engineering Aspects,* vol. 222, pp. 223-232, 2003.

[95] H. W. Wang, H. C. Lin, Y. C. Yeh, and C. H. Kuo, "Synthesis of Fe_3O_4 nanoparticles and formation of nanowire by electrophoretic deposition", *Journal of Magnetism and Magnetic Materials,* vol. 310, pp. 2425-2427, 2007.

[96] I. Zhitomirsky, "Cathodic electrodeposition of ceramic and organoceramic materials. Fundamental aspects", *Advances in Colloid and Interface Science,* vol. 97, pp. 279-317, 2002.

[97] S. Heavens, "Electrophoretic depositions as a processing route for ceramics," in *Advanced ceramics processing and technology*. vol. 1, ed: Noyes publications, 1990, pp. 255-283.

[98] (September 2012). *Image adapted from:* http://en.wikipedia.org/wiki/Zeta_potential

[99] H. C. Hamaker and E. J. W. Verwey, "(C) Colloid stability. The role of the forces between the particles in electrodeposition and other phenomena", *Transactions of the Faraday Society,* vol. 35, pp. 0180-0185, 1940.

[100] F. Grillon, D. Fayeulle, and M. Jeandin, "Quantitative Image-Analysis of Electrophoretic Coatings", *Journal of Materials Science Letters,* vol. 11, pp. 272-275, 1992.

[101] P. Sarkar and P. S. Nicholson, "Electrophoretic deposition (EPD): Mechanisms, kinetics, and application to ceramics", *Journal of the American Ceramic Society,* vol. 79, pp. 1987-2002, 1996.

[102] B. Ferrari and R. Moreno, "EPD kinetics: A review", *Journal of the European Ceramic Society,* vol. 30, pp. 1069-1078, 2010.

[103] R. W. Powers, "Electrophoretic Forming of Beta-Alumina Ceramic", *Journal of the Electrochemical Society,* vol. 122, pp. 490-500, 1975.

[104] (March 2012). *Product technical data*. Available: https://http://www.polymersource.com/dataSheet/P8658-SEO.pdf

[105] R. E. Dinnebier and S. J. L. Billinge, *Powder Diffraction - Theory and Practice*: RSC Publishing, 2008.

[106] C. Hammond, *The Basics of Crystallography and Difrraction*, 3 ed.: Oxford University Press, 2009.

[107] P. Echlin, *Handbook of Sample Preparation for Scanning Electron Microscopy and X-Ray Microanalysis*: Springer, 2009.

[108] M. Dunlap and J. E. Adaskaveg, *Introduction to the Scanning Electron Microscope - Theory, Practice and Procedures*: Facility for advanced instrumentation, 1997.

[109] K. S. W. Sing, D. H. Everett, R. A. W. Haul, L. Moscou, R. A. Pierotti, J. Rouquerol, and T. Siemieniewska, "Reporting Physisorption Data for Gas Solid Systems with Special Reference to the Determination of Surface-Area and Porosity", *Pure and Applied Chemistry,* vol. 57, pp. 603-619, 1985.
[110] Roque-Malherbe and R. M. A., *Adsorption and Diffusion in Nanoporous Materials*: CRC PressINC, 2007.
[111] A. Gruverman and S. V. Kalinin, "Piezoresponse force microscopy and recent advances in nanoscale studies of ferroelectrics", *Journal of Materials Science,* vol. 41, pp. 107-116, 2006.
[112] J. Clarke and A. I. Braginski, *The SQUID Handbook* vol. I: Wiley-VCH, 2004.
[113] (August 2012). *Image adapted from*: http://www.csiro.au/~/Media/CSIROau/Images/Maps Graphs/SQUID_CESRE_ind/High_Resolution.gif
[114] Y. Zhang, Y. Liu, C. L. Fei, Z. Yang, Z. H. Lu, R. Xiong, D. Yin, and J. Shi, "The temperature dependence of magnetic properties for cobalt ferrite nanoparticles by the hydrothermal method", *Journal of Applied Physics,* vol. 108, 2010.
[115] F. Maxim, P. Ferreira, P. M. Vilarinho, A. Aimable, and P. Bowen, "Additive-Assisted Aqueous Synthesis of $BaTiO_3$ Nanopowders", *Crystal Growth & Design,* vol. 10, pp. 3996-4004, 2010.
[116] M. G. Naseri, E. B. Saion, H. A. Ahangar, M. Hashim, and A. H. Shaari, "Simple preparation and characterization of nickel ferrite nanocrystals by a thermal treatment method", *Powder Technology,* vol. 212, pp. 80-88, 2011.
[117] M. G. Naseri, E. B. Saion, H. A. Ahangar, A. H. Shaari, and M. Hashim, "Simple Synthesis and Characterization of Cobalt Ferrite Nanoparticles by a Thermal Treatment Method", *Journal of Nanomaterials,* 2010.
[118] Y. Cheng, B. Zou, J. Yang, C. Wang, Y. Liu, X. Fan, L. Zhu, Y. Wang, H. Ma, and X. Cao, "Fabrication of $CoFe_2O_4$ hollow fibers by direct annealing of the electrospun composite fibers and their magnetic properties", *CrystEngComm,* vol. 13, pp. 2268-2272, 2011.
[119] W. Ponhan and S. Maensiri, "Fabrication and magnetic properties of electrospun copper ferrite ($CuFe_2O_4$) nanofibers", *Solid State Sciences,* vol. 11, pp. 479-484, 2009.
[120] J. L. Zhao, X. H. Wang, and L. T. Li, "Electrophoretic deposition of $BaTiO_3$ films from aqueous suspensions", *Materials Chemistry and Physics,* vol. 99, pp. 350-353, 2006.
[121] (October 2012). *Product technical data*. Available: http://www.sigmaaldrich.com/chemistry/solvents/hexane-center/physical-properties.html